NANYANG TECHNOLOGICAL UNIVERSITY

CORROSION FATIGUE BEHAVIORS OF ALUMINUM ALLOYS FOR OFFSHORE APPLICATIONS

NGUYEN NGOC VU

INTERDISCIPLINARY GRADUATE SCHOOL
ENERGY RESEARCH INSTITUTE @ NTU (ERI@N)

2016

CORROSION FATIGUE BEHAVIORS OF ALUMINUM ALLOYS FOR OFFSHORE APPLICATIONS

NGUYEN NGOC VU

Interdisciplinary Graduate School
Energy Research Institute @ NTU (ERI@N)

A thesis submitted to the Nanyang Technological
University in partial fulfilment of the requirement for
the degree of
Doctor of Philosophy

2016

Statement of Originality

I hereby certify that the work embodied in this thesis is the result of original research and has not been submitted for a higher degree to any other University or Institution.

. . . 23-December-2016. . . . .
Date Nguyen Ngoc Vu

Abstract

Pitting corrosion in conjunction with fatigue has been a great concern for structural integrity of aluminium alloys that are being extensively used in offshore applications due to their unique properties, high strength-to-weight ratio compared to other materials. This study aims at investigating corrosion fatigue behaviors of Aluminum alloys to provide a reliable corrosion fatigue control and further extend the use of aluminum alloys in offshore applications. Specifically, the contents of this thesis are as follows:

Firstly, the 3-D morphological damage of pitting corrosion was characterized using confocal microscopy and image processing. A method that simplified the complex and tortuous morphology of pits into idealized shapes was proposed. This method incorporates the combined effect of pit morphology and orientation as well as its interaction with other pits in adjacent areas. Therefore, it provides a realistic approximation in quantifying stress-strain concentration factor, which can be used to predict possible crack nucleation sites as well as the early stage of crack propagation behavior.

Secondly, microstructural characteristics of pitting corrosion were examined using Scanning Electron Microscopy (SEM) and Orientation Imaging Microscopy (OIM) based analysis technique. The effects of crystallographic texture on pitting susceptibility and fatigue performance were studied. Crystallographic pits were found to be the main cause of fatigue failure and preferably initiate from the inside of grains having orientation close to $\langle 001 \rangle$. Furthermore, crack initiation characteristics and fatigue performance of aluminum alloys when subjected to prior corrosion were investigated. Fatigue endurance along rolling direction is higher than along transverse direction due to the morphology of crystallographic pits and grain texture. Critical fatigue crack nucleated from grain boundaries that were damaged by corrosion processes around a crystallographic pit. Fatigue crack nucleation was further assisted by surrounding grains that have multiple active slip systems associating with high Schmid factor value.

Finally, fatigue crack initiation characteristics and crack growth mechanisms of an aluminum alloy when simultaneously subjected to a corrosive environment were investigated. Fatigue crack nucleation, as well as crack propagation, was affected by corrosive environment. High stress concentration at both sides of pit mouth in conjunction with attacked grain boundaries favoured fatigue crack nucleation while the presence of hydrogen formed by corrosion reactions caused crack tip embrittlement and intensified crack growth rate. The findings in this work offer a better understanding of fatigue crack initiation and propagation mechanisms of aluminum alloys and provide a more realistic corrosion fatigue life prediction for structures operating in the offshore environment.

Acknowledgements

I wish to thank, first and foremost, Assistant Professor Li Peifeng for his invaluable encouragement and supervision throughout this project. His prompt inspirations, enthusiasm and constructive suggestions with kindness have helped me to a very great extent to conduct this project.

I would like to extend my utmost gratitude to Dr. Narasimalu Srikanth for his valuable advice and continuous support during this project.

I also wish to express my thanks to Associate Professor Fan Zheng, my mentor in this project, who offered his precious time to assist me with my project.

In addition, I would like to take this opportunity to express my sincere gratitude to the laboratory staffs in MAE, especially Ms. Yong Mei Yoke, Ms. Chia Hwee Lang, for their precious assistance in equipment training. They helped me to acquire the skills on the operation of many advanced instruments for conducting this research.

Meanwhile, I am also indebted to my many colleagues and friends who supported me through this project and gave me a meaningful PhD life.

Finally, I wish to thank my beloved family and my girlfriend for their continuous support and encouragement. I would like to dedicate this achievement to all of them.

Table of Contents

Table Captions

Figure Captions

Abbreviations

Mtoe	Million tonnes of oil equivalent
Mt	Megatonne
AFM	Atomic Force Microscopy
SEM	Scanning Electron Microscopy
EBSD	Electron Backscattered Diffraction
EBSP	Electron Beam Scattering Patterns
OIM	Orientation Imaging Microscopy
BEI	Backscatter Electron Images
BSE	Backscattered Electron
EDS	Energy Dispersive X-ray Spectroscopy
HEDE	Hydrogen-enhanced decohesion
HELP	Hydrogen-enhanced localized plasticity
AIDE	Adsorption Induced Dislocation Emission
IPF	Inverse Pole Figure
fcc	face-centered cubic

Publications

P. Li, **N. V. Nguyen**, and H. Hao, "Dynamic compressive behaviour of Mg foams manufactured by the direct foaming process," *Materials & Design*, vol. 89, pp. 636-641, 1/5/ 2016.

Chapter 1

Introduction

This chapter introduces the background, motivation, and objectives of this research. Renewable energy has been established as a mainstream source thanks to several developments in technology as well as public awareness. Among different forms of renewable energy, offshore renewable energy is emerging as a promising source since the world's oceans and seas provide enormous amounts of clean energy, which can be harnessed from offshore winds, tides and ocean currents. Renewable energy technologies provide a large market of opportunity for aluminum and its alloys. However, aluminum alloys are more subjected to pitting corrosion when working in offshore conditions due to the high salinity of seawater. Moreover, offshore structures are typically subjected to fatigue loads, which naturally exist as a result of many factors such as winds, waves or ocean currents. This research focuses on investigating corrosion fatigue behaviors of Aluminum alloys to provide a reliable corrosion fatigue control and further extend the use of aluminum alloys in offshore applications.

1.1. Background

There are now more than seven billion people populating this planet, and this figure is projected to reach 8.5 billion by 2030, 9.7 billion in 2050 and 11.2 billion in 2100, according to the United Nations Population Division [1]. This rapid growth of human footprint is putting more pressure on natural resources and the ecosystem. Fossil fuels have long been the main sources for human energy demands. As shown in Figure 1.1, the use of fuel energy keeps increasing time after time since 1971. Reported by International Energy Agency in 2016, world energy production in 2014 was 13800 Mtoe, which is 1.1% higher than that in 2013. Fossil fuels accounted for 81.2% of it with oil production increased the most (2.1%), followed by coal and natural gas (0.8% and 0.6% respectively). Together, the production of these three fossil fuels increased by 1.3% in 2014 (Figure 1.2). However, exploiting these sources of energy has caused a huge impact on the environment and human health, including water and land pollution, biodiversity loss, and climate change. Moreover, coal and other fossil fuels are one-time energy and will soon be exhausted with the escalating of energy consumption [2].

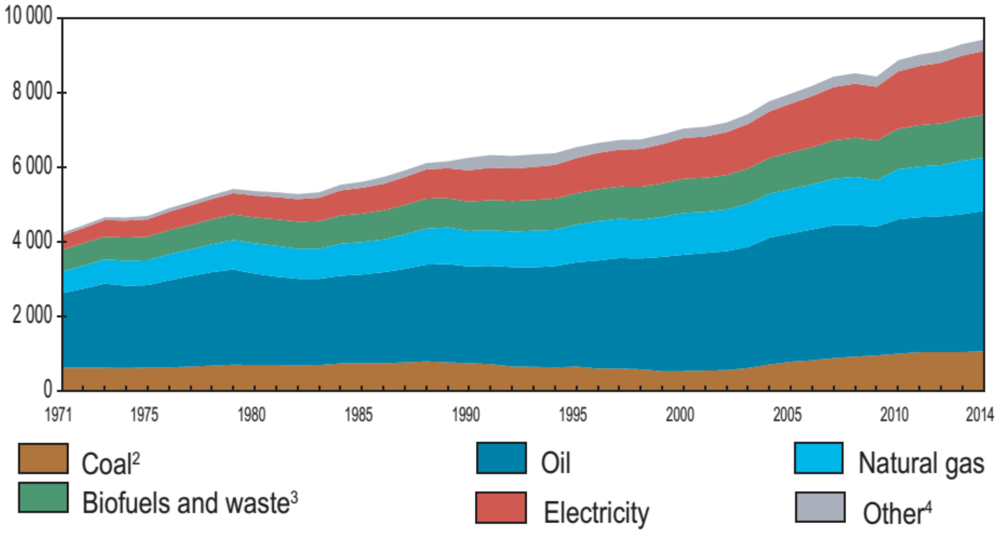

Figure 1.1 World total energy consumption from 1971 to 2014 by fuel (Mtoe) [3]

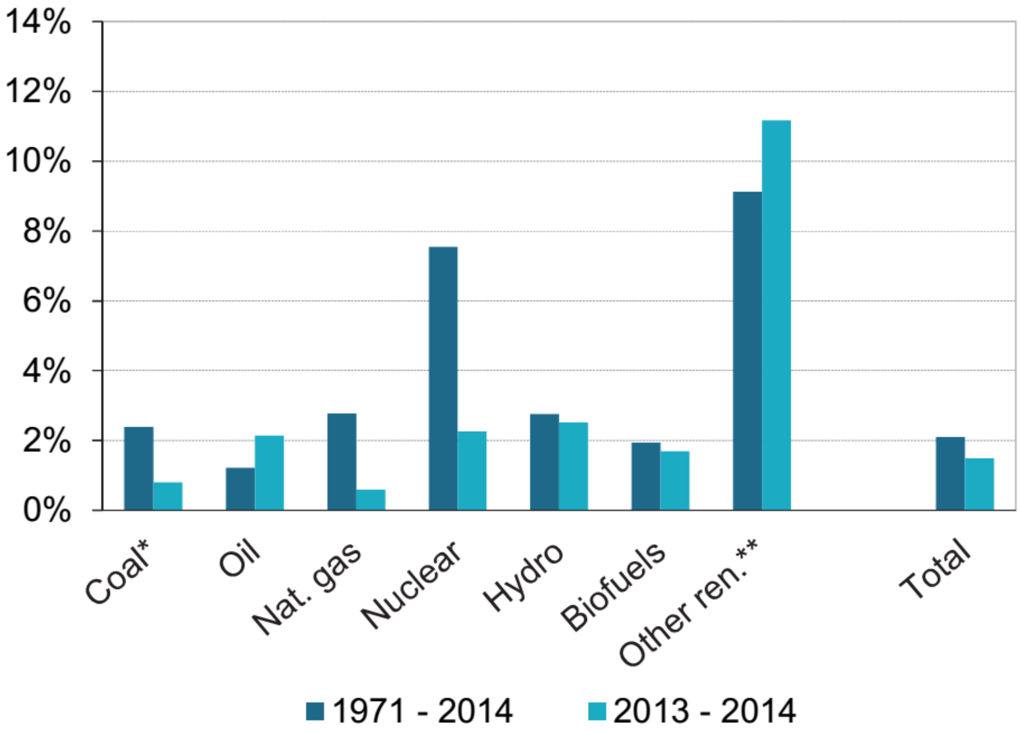

Figure 1.2 Global energy change in energy production by fuel [4]

In recent years, renewable energy has been established as a mainstream source thanks to several developments in technology as well as public awareness. In 2014, renewable energy afforded almost one fifth of global energy consumption. Besides, much progress in energy capacity has been made. It added approximately 147 gigawatts (GW) of renewable power capacity in 2015, the largest annual improvement ever, while renewable heat capacity enhanced by about 38 gigawatts-thermal (GWth) together with growing in total production of biofuels. The year of 2015 also saw a historic Paris Agreement that reinforced global awareness of climate change and environment. A number of long-term contracts were announced regarding the lowest prices for renewable energy. The extraordinary development of renewable energy was an outcome of several factors, including innovation in renewable technologies, dedicated policy supports and mobilizing financial resources for resilience investments.

Among different forms of renewable energy, offshore renewable energy is emerging as a promising source since the world's oceans and seas provide enormous amounts of clean energy which can be harnessed from offshore winds, tides and ocean currents. Several projects are being deployed farther from the coasts and in deeper water. Offshore wind annual deployment marked a new record, with over 3 GW connected to the grid, mostly in Europe, for a world total exceeding 12 GW. Wind power is playing a major role in meeting electricity demand in an increasing number of countries, including Denmark (42% of demand in 2015), Germany (more than 60% in four states) and Uruguay (15.5%) [5]. In 23.7% of renewable electricity, offshore wind energy together with hydropower is projected to provide up to 20.3% of electricity production (Figure 1.3).

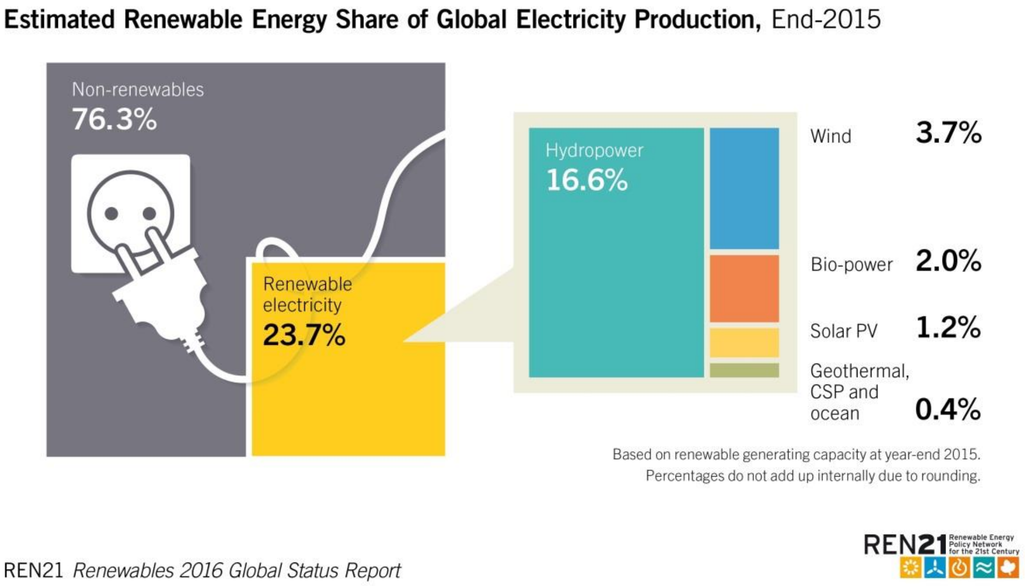
Estimated Renewable Energy Share of Global Electricity Production, End-2015

Based on renewable generating capacity at year-end 2015. Percentages do not add up internally due to rounding.

REN21 *Renewables 2016 Global Status Report*

Figure 1.3 Estimated renewable energy share of global electricity production [5]

Although offshore hydropower is less established, innovation in technologies using tidal currents or the power of waves to generate electricity from seawater is being accelerated. Offshore hydropower market accounted for more than 16% of the overall hydropower production in 2015, and it is anticipated to have an annual growth rate of more than 3% from 2016 to 2023. By properly taking advantage of offshore renewable energy in a manner that preserves the ocean ecosystem, we can lessen our dependence on fossil fuels, restrain global warming, protect our habitat and step to a sustainable future [6].

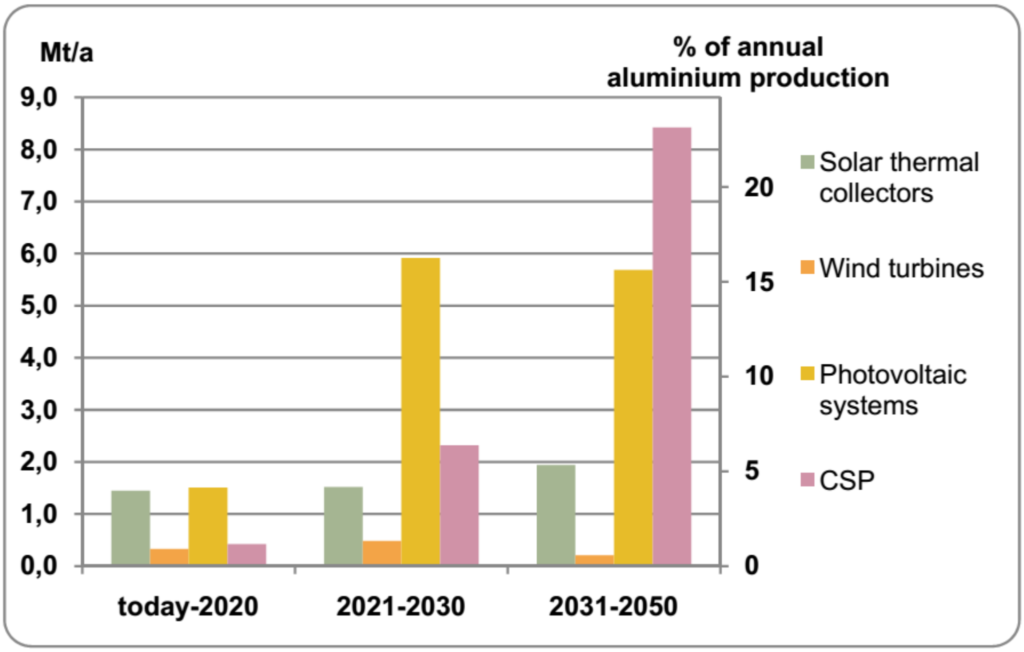

Figure 1.4 Projected Aluminum use in renewable energy systems in the most promising scenario [7]

Renewable energy technologies provide a promising market for aluminum and its alloys. The use of aluminum in renewable energy systems is expected to increase up to 10 % in the most promising scenario [7]. As shown in Figure 1.4, renewable energy systems could consume approximately 1.4% of annual aluminum production from now until 2020. Furthermore, this figure is projected to reach 4% of total aluminum sales or equivalently 1.5Mt per year from 2021 to 2030, and it could rise up to nearly 9% in the 2031-2050 period. In order to transport the electricity through marine cables to the mainland, offshore wind farms require more use of aluminum compared to onshore systems due to the additional need of transformers and cable stations, which are partly made of aluminum. On land, the electricity is then transmitted in an amount equal to the transmission from onshore wind turbines. In other technology areas, aluminum has to compete with other materials such as steel and composites. Nonetheless, aluminum is already used to a great extent within renewable energy technologies, for example, photovoltaic systems and solar collectors.

Primary aluminum production has grown significantly over the past few decades, by 110% from 24 Mt in 2000 to 51 Mt in 2013 [8]. The consumption and production of aluminum and its alloys keep increasing over time and now only behind steel alloys. Aluminum is being extensively used in offshore applications due to many versatile properties such as superior strength-to-weight ratio, ease of fabrication, lower maintenance cost, and longer life span, but most of all, its weight reduction in comparison with ferrous alloys. Moreover, recycling aluminum requires only 5% of the primary energy input for production, making it a prominent material for marine renewable energy applications. The 5xxx series of Aluminum alloys, which are well known for their admirable corrosion resistance and weld ductility, have been effectively used in marine construction and offshore applications, some of which are jack-up barges, tension leg platforms (TLPs), piping, marine vessels and hulls, etc. Furthermore, some alloy series such as 2xxx and 7xxx can be employed in structures where high tensile strengths (450-550 MPa) are desired. However, some protective methods (coatings, corrosion inhibitors or cathodic protection) are required to ensure acceptable service expectancy [9].

While aluminum alloys exhibit adequate corrosion resistance in atmospheric environments, they are more subjected to pitting corrosion when working in offshore conditions due to the high salinity of seawater which enhances the pitting process of alloying elements. Moreover, offshore structures are typically subjected to fatigue loads, which naturally exist as a result of many factors such as winds, waves or ocean currents. In conjunction with corrosion effects, these fatigue loads facilitate the initiation and development of cracks, which in turn could lead to unexpected failures. According to National Association of Corrosion Engineers (NACE) report, corrosion has cost the marine industry of America alone $2.7 billion every year, and the annual cost of marine corrosion all over the world was estimated to be around $65 billion [10]. In addition to the economic problem, corrosion fatigue is a safety concern since several catastrophic accidents have occurred as fatigue cracks develop from corrosion pits in a corrosive environment, resulting in fatalities, environmental as well as property damage.

1.2. Motivation and research objectives

As mentioned above, structures operating in offshore conditions are naturally subjected to both corrosion and dynamic loads. Corrosion fatigue must be distinguished from stress corrosion, which is the growth of cracks under stable load or residue stress. Under stress corrosion conditions, cracks normally develop along the grains of materials whereas corrosion fatigue cracks are generally normal to the direction of principal stress and can be transgranular. Furthermore, stress corrosion cracking does not happen in many materials while corrosion fatigue can take place in most of structural materials. The joint effects of corrosion and fatigue, which have been considered as hazardous threats to structural integrity, are highly dependent on many factors including temperature, stress state, working conditions, and kind of materials [11]. In order to enhance its mechanical performance, several alloying elements are included into aluminum. These elements produce inhomogeneity into the microstructure of aluminum, which adjusts the pitting potential and makes the pitting processes more complicated [12]. Several studies [13-15] have shown that pitting corrosion is an influential factor, which has a substantial effect on fatigue performance of aluminum alloys. A critical aspect of corrosion fatigue is pitting morphology and characterization. Local discontinuities caused by pitting have a variety of shapes and sizes as a result of intricate microstructure and electrochemical behaviors of alloying materials. A number of studies have been conducted using various techniques to elucidate the pit initiation, propagation mechanisms and characterize corrosion behavior of metals under corrosive environment. Nevertheless, current approaches to inspect and characterize pitting morphology are mainly based on two-dimensional models involving expressions for just pit depth or area, which take certain simplifications and assumptions. They cannot capture the intrinsic complexity of pit profile below the surface and pit depth, which are considered as the most critical parameters in characterizing pitting corrosion [16]. The morphologic characteristics of pitting corrosion in 3-D should be given more consideration as the pit growth rate is highly dependent on potential distribution within the pit, which is dominated by pit profile [17, 18].

Previous authors [19-21] who studied corrosion of single face-centered cubic (fcc) Aluminum crystals demonstrated that pitting potential of single crystal fcc Al is strongly dependent on crystal orientation. Chloride concentration and pH value are also critical factors that determine dissolution rates of face-centered cubic Aluminum single crystal with various orientation [22, 23]. Furthermore, rolling processes, which cause anisotropic properties in materials, considerably affect corrosion and fatigue performance of aluminum alloys along longitudinal and transverse directions. During service life in an offshore environment, a structure could encounter fatigue loads from various directions. However, the effects of microstructures and crystal orientation on pitting susceptibility and anisotropic fatigue performance of aluminum alloys in a corrosive environment have not been sufficiently investigated.

In a corrosive environment, hydrogen is generated by cathodic corrosion reactions and then absorbs at crack tips. There is broad consensus that degradation of crack growth resistance is caused by crack tip embrittlement due to the presence of hydrogen species. Of the many proposals, the three most widely accepted interstitial mechanisms are: Hydrogen-enhanced localized plasticity (HELP), Hydrogen-enhanced decohesion (HEDE) and Adsorption Induced Dislocation Emission (AIDE). Nevertheless, the embrittlement mechanisms and kinetics involved are not fully resolved and are still controversial disputes as there are many possible material-environment interactions can occur at crack tips [24].

In summary, pitting corrosion in conjunction with fatigue is a complex phenomenon involving various processes and mechanisms. There are a number of factors that can affect the corrosion fatigue performance of materials, for instance, microstructure of materials, grain orientation, role of pit morphology as well as pit proximity, hydrogen generation and dislocation interactions at crack tip. Although the effects of those factors have been systematically identified and investigated, they cannot be generally applied to all materials in a particular environment. Moreover, the mechanism of corrosion fatigue damage is still a controversial issue, and fatigue life prediction is mainly empirical. The corrosion fatigue behavior of materials in marine structures has long been a topic of practical importance. Nevertheless, a number of failures have been encountered in many offshore structures and components in spite of several published reports.

The life expectancy of a structure can be categorized as follows [25]:

- Initiation of damage by corrosion in combination with fatigue process. There is a transition from pitting to fatigue crack at the end of this stage.
- Joining of small cracks and propagation (short crack growth regime).
- Long crack growth regime where fracture mechanics theories (LEFM, EPFM or FPEM) are applicable for material analysis and characterization.
- Unstable development of cracks until failure.

The lifetime of a structure during the first two stages is highly dependent on corrosion processes, which cause local discontinuities in the structure and enhance the nucleation as well as propagation processes of small fatigue cracks. Since the pit initiation and development, as well as pit to crack transition, could account for up to 80 percent of the total corrosion fatigue life, it is of the essence to have a better understanding of corrosion fatigue mechanisms of Aluminum alloys, which are being extensively used in offshore applications, for structural design.

This research focuses on investigating corrosion fatigue behaviors of Aluminum alloys to provide a reliable corrosion fatigue control and further extend the use of aluminum alloys in offshore applications. Towards this target, this study analyzes the microstructural characteristics of pitting corrosion in aluminum alloys, explores how fatigue cracks initiate from corrosion pits and further elucidates fatigue crack growth mechanism of aluminum alloys in a corrosive environment. Particularly, the objectives of this project are as follows:

- To characterize morphological damage of pitting corrosion and to quantify the effects of pit induced stresses on aluminum alloys using three-dimensional models.
- To explore the characteristics of pitting corrosion and their dependency on microstructures, grain texture, and grain orientation using an orientation imaging microscopy based analysis technique.
- To investigate the effects of corrosion on pit to crack transition and to evaluate anisotropic fatigue performance of aluminum alloys when subjected to prior corrosion.
- To further elucidate fatigue crack initiation and propagation behaviors of aluminum alloys when simultaneously subjected to a corrosive environment.

1.3. Dissertation Overview

The structure of this dissertation will be presented as follows:

Chapter 1 provides a brief introduction to the background, motivation, and objectives of this research.

Chapter 2 reviews the fundamental theories and previous work related to this study. Firstly, the essential aspects of pitting corrosion and general performance of Aluminum alloys are addressed. Afterwards, the fatigue behaviors and failure mechanisms of aluminum alloys are discussed together with the characterization and modelling techniques.

Chapter 3 describes the principle of experimental methodologies employed in this study to investigate material properties and characterize corrosion fatigue damage.

Chapter 4 to Chapter 6 elaborates the major results and discussion of this research.

Chapter 4 quantifies the corrosion damage and investigates the 3-D morphological characteristics of pitting corrosion of aluminum alloy AA7075-T6. An analysis procedure was developed to quantify the severity of corrosion and classify pit morphology using a 3-D shape descriptor. A method that simplified the complex and tortuous morphology of pits into idealized shapes was proposed in order to provide a realistic approximation in quantifying stress-strain concentration factor.

Chapter 5 investigates the effects of microstructure, crystallographic orientation, and grain texture on pitting susceptibility and anisotropic fatigue performance of aluminum alloy AA6061-T6 when subjected to prior corrosion. Characteristics of pitting corrosion and fatigue crack initiation were examined using Scanning Electron Microscopy (SEM) and Orientation Imaging Microscopy (OIM) based analysis technique. Moreover, the preferred orientation of grains having high susceptibility to pitting was identified that could offer an important contribution to corrosion resistance aspect.

Chapter 6 investigates crack initiation characteristics and crack growth mechanisms of AA6061-T6 when simultaneously fatigue loaded in a corrosive environment. Fatigue performance and crack growth mechanisms of AA 6061-T6 tested in ambient air and in NaCl 3.5% solution were compared. The mathematical concept of pivot point was used to model the transition of crack growth rate during stage II region with different exponential laws.

Chapter 7 draws together the conclusions of this research and outlines the recommendations for future work.

1.4 Findings and Contributions

The major findings and contributions of this research are summarized as follows:

- The morphological damage of pitting corrosion was characterized using a three-dimensional model. Three-dimensional pitting surface of the corroded sample was reconstructed using data obtained from confocal microscopy. Confocal microscopy was proven to be a great assistance in quantifying corrosion damage and characterizing pitting morphology in 3-D. A methodology was proposed to simplify tortuous morphology of corrosion pits into idealized geometry. The proposed method provides a realistic approximation in quantifying stress-strain concentration factor, which can be used to predict possible crack nucleation sites as well as the early stage of crack propagation behavior.
- Characteristics of pitting corrosion and fatigue crack initiation were examined using Scanning Electron Microscopy (SEM) and Orientation Imaging Microscopy (OIM) based analysis technique. Crystallographic pits were found to be the main cause of fatigue failure and preferably initiate from the inside of grains having orientation close to $\langle 001 \rangle$. OIM analysis revealed that critical fatigue crack, when subjected to prior corrosion, nucleated from grain boundaries that were damaged by corrosion processes around a crystallographic pit. Fatigue crack nucleation was further assisted by surrounding grains that have multiple active slip systems associating with high Schmid factor value. These findings provide an important contribution to corrosion resistance aspect as well as fatigue crack initiation understandings. Corrosion inhibitors might be developed to restrict the corrosion processes of crystallographic pits on $\langle 001 \rangle$ facets that could, in turn, improve fatigue performance of structures operating in the offshore environment. Furthermore, advanced manufacturing techniques could be involved in producing materials with texture having superior corrosion resistance.

- An environmental chamber consisting of 3.5% NaCl by weight was used to investigate crack initiation characteristics and crack growth behaviors of AA6061-T6 when simultaneously fatigue loaded in a corrosive environment. Crack nucleation, as well as crack propagation, was affected by corrosive environment. High stress concentration at both sides of pit mouth in conjunction with attacked grain boundaries favoured fatigue crack nucleation while the presence of hydrogen formed by corrosion reactions caused crack tip embrittlement and intensified crack growth rate. Two stages of short crack growth were identified by fractography analysis. Near crack origin, which is a crystallographic pit, crack propagated transgranularly along crystallographic planes due to Hydrogen-enhanced decohesion process. Further crack growth is dominated by Adsorption Induced Dislocation Emission process resulting in a mixed mode of intergranular and transgranular crack growth with a higher portion of transgranular. These findings offer a better understanding of fatigue crack initiation and propagation mechanisms of aluminum alloys and provide a more realistic corrosion fatigue life prediction for structures operating in the offshore environment.

References

1. United Nations, Department of Economic and Social Affairs, Population Division. World population prospects: The 2015 revision, key findings and advance tables; 2015. Working Paper No. ESA/P/WP.241.
2. Hodgson, P., *Nuclear Power and the Energy Crisis.* Modern Age, 2008. **50**(3): p. 238.
3. IEA, *Key World Energy Statistics 2016*. IEA.
4. OECD, *World Energy Balances 2016*. OECD Publishing.
5. REN21, 2016, 'Renewables 2016 Global Status Report', www.ren21.net/status-of-renewables/global-status-report/.
6. Natural Resources Defense Coucil,"Harvesting the benefits of homegrown, renewable energy," Available: http://www.nrdc.org/energy/renewables/offshore.asp.

7. Bödeker, J.M., M. Bauer, and M. Pehnt, *Aluminium and Renewable Energy Systems–Prospects for the Sustainable Generation of Electricity and Heat.*

8. IAI (2015a),Current IAI Statistics, www.world-aluminium.org/statistics/ (accessed 7 December 2015).

9. Marcus, P., *Corrosion mechanisms in theory and practice*. 2011: CRC Press.

10. Koch, G.H., et al., *Corrosion cost and preventive strategies in the United States*. 2002.

11. Schijve, J., J. Schijve, and J. Schijve, *Fatigue of structures and materials*. 2001: Springer.

12. Davis, J.R., *Corrosion of aluminum and aluminum alloys*. 1999: ASM International.

13. Pao, P.S., S.J. Gill, and C.R. Feng, *On fatigue crack initiation from corrosion pits in 7075-T7351 aluminum alloy.* Scripta Materialia, 2000. **43**(5): p. 391-396.

14. Sankaran, K.K., R. Perez, and K.V. Jata, *Effects of pitting corrosion on the fatigue behavior of aluminum alloy 7075-T6: modeling and experimental studies.* Materials Science and Engineering: A, 2001. **297**(1–2): p. 223-229.

15. Genel, K., *The effect of pitting on the bending fatigue performance of high-strength aluminum alloy.* Scripta Materialia, 2007. **57**(4): p. 297-300.

16. North Atlantic Treaty Organization, R. and O. Technology, *Corrosion fatigue and environmentally assisted cracking in aging military vehicles La fatigue-corrosion et la fissuration en milieu ambiant des véhicules militaires vieillissants*. 2011, [Neuilly-sur-Seine Cedex]: N.A.T.O., Research and Technology Organization.

17. Pickering, H.W., *The role of electrode potential distribution in corrosion processes.* Materials Science and Engineering: A, 1995. **198**(1–2): p. 213-223.

18. Engelhardt, G., M. Urquidi-Macdonald, and D.D. Macdonald, *A simplified method for estimating corrosion cavity growth rates.* Corrosion Science, 1997. **39**(3): p. 419-441.

19. Yu, S. and P. Natishan, *Critical factors in localized corrosion III.* by RG Kelly, PM Natishan, GS Frankel and RC Newman, Pennington, NJ, 1999.

20. Davis, B., P. Moran, and P. Natishan, *Metastable pitting behavior of aluminum single crystals.* Corrosion science, 2000. **42**(12): p. 2187-2192.

21. Yasuda, M., F. Weinberg, and D. Tromans, *Pitting Corrosion of Al and Al‐Cu Single Crystals.* Journal of the Electrochemical Society, 1990. **137**(12): p. 3708-3715.

22. Koroleva, E., et al. *Crystallographic dissolution of high purity aluminium*. in *Proceedings of the Royal Society of London A: Mathematical, Physical and Engineering Sciences*. 2007. The Royal Society.

23. Takayama, Y., M. Sato, and H. Watanabe. *Crystallographic Orientation Dependence of Corrosion Behavior of 5N Purity Aluminum in Different Concentrations of HCl Aqueous Solutions*. in *ICAA13: 13th International Conference on Aluminum Alloys*. Wiley Online Library.

24. Lynch, S., *Understanding Mechanisms and Kinetics of Environmentally Assisted Cracking.* BHM Berg-und Hüttenmännische Monatshefte, 2016. **161**(1): p. 3-18.

25. Hoeppner, D. *Parameters that input to application of damage tolerance concepts to critical engine components*. in *AGARD conference proceedings*. 1985. AGARD.

Chapter 2

Literature Review

This chapter reviews the fundamental theories and previous work related to this study. Firstly, the essential aspects of pitting corrosion and general corrosion resistance of Aluminum alloys are presented. Afterwards, the pitting characterization and modelling techniques involved are discussed. Subsequently, the fatigue behaviors and failure mechanisms of aluminum alloys when subjected to a corrosive environment are described. Finally, this chapter briefly summarizes all of corrosion fatigue aspects related to this research topic and indicates the research gaps.

2.1. Pitting Corrosion of aluminum and its alloys

2.1.1. Pitting corrosion

Pitting corrosion is a form of localized attack that occurs on every Aluminum alloys and in most of environments, especially in offshore conditions which have high concentration of chloride ion [1]. In general, there are four essential prerequisites for corrosion to take place, namely an anode, a cathode and an electrolyte joined by a metallic path [2] as shown in Figure 2.1. The mechanism of pitting is based on the dissolution of metals in anode:

$$Al \rightarrow Al^{3+} + 3e^{-} \qquad (2.1)$$

and several cathodic reactions, which could be the oxygen reduction:

$$O_2 + 2H_2O + 4e- \rightarrow 4OH^{-} \qquad (2.2)$$

or hydrogen development in neutral or acidic environments:

$$2H^{+} + 2e^{-} \rightarrow H_2 \qquad (2.3)$$

$$2H_20 + 2e^{-} \rightarrow H_2 + 20H^{-} \qquad (2.4)$$

The types of corrosion reaction and their products are dependent on several factors including temperature, concentration of dissolved oxygen, chemical composition of alloys, pH scale of the media, etc.

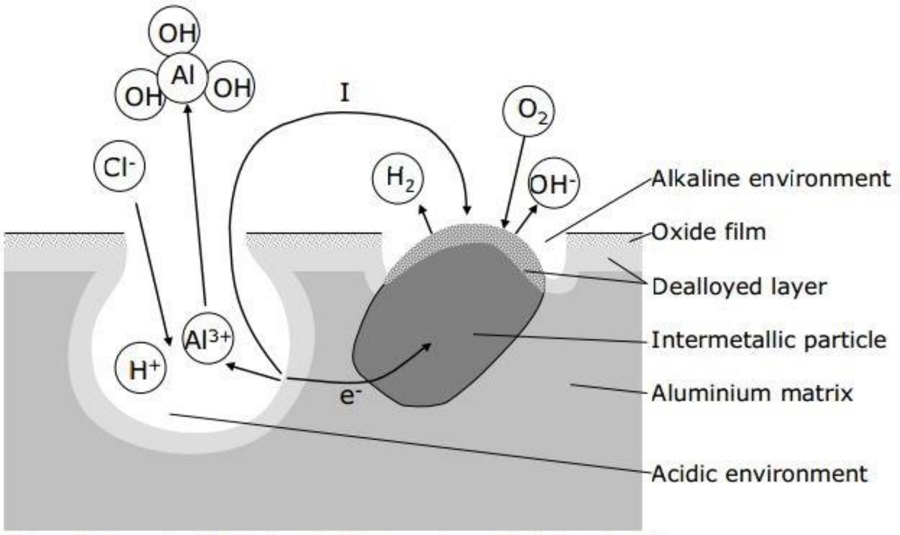

Figure 2.1 An illustration of pitting corrosion processes of Aluminum alloy [3]

Pitting processes of aluminum can be categorized into four stages [4]: (1) Anion adsorption on the aluminum oxide layer, (2) reactions of those anions with aluminum ions, (3) dissolution of the oxide layer and (4) localized attack on the bare metal that results in the formation of pits. Offshore conditions, which contain high concentration of chloride ions, are particularly unfavorable for aluminum alloys. Pitting in pure aluminum has a tendency to repassivate in certain oxidizing conditions by reproducing its oxide layer [5]. The oxide layer, which is a thermodynamic stable form of aluminum, functions as a protective barrier enhancing corrosion resistance of aluminum and its alloys in aggressive environments. However, the presence of chloride ions facilitates the dissolution process of aluminum oxide film by producing $AlCl_3$ which is typically found at pit locations. Although there has been much dispute over the breakdown mechanism of this oxide layer by chloride ions [6, 7], the common agreement is that the penetration of destructive anions initiates localized damages and produces soluble compounds on the pitting surface.

Several alloying elements are included into aluminum in order to enhance its mechanical performance. On the contrary, these elements produce inhomogeneity into the microstructure of aluminum, which creates favorable conditions for pitting corrosion to initiate. For pure aluminum or 5xxx series, they are less susceptible to pitting due to their low heterogeneous microstructure. However, heterogeneity is an essential requirement in further improving mechanical performance of aluminum alloys. Therefore, high strength and heat treatable aluminum alloys such as 2xxx, 6xxx, 7xxx series are highly subjected to pitting corrosion. Figure 2.2 indicates an upward tendency of corrosion rate of several aluminum alloys in corresponding to their hardness, which could stand for yield strength. It suggests a great necessity to understand the effects of alloying elements on corrosion resistance of aluminum alloys.

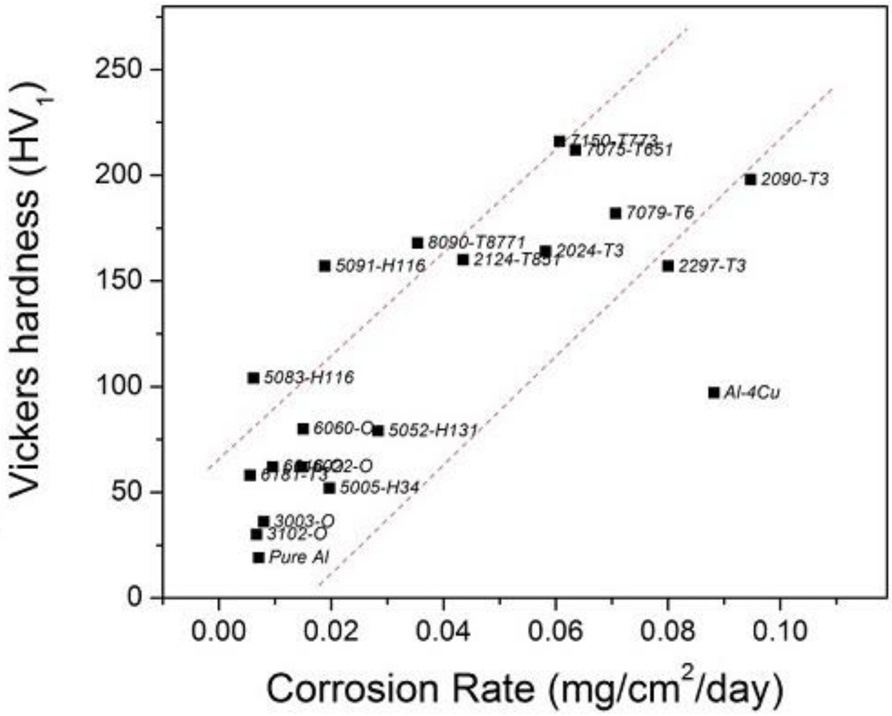

Figure 2.2 Corrosion rate of various Al alloys (mg/cm2/day) [8]

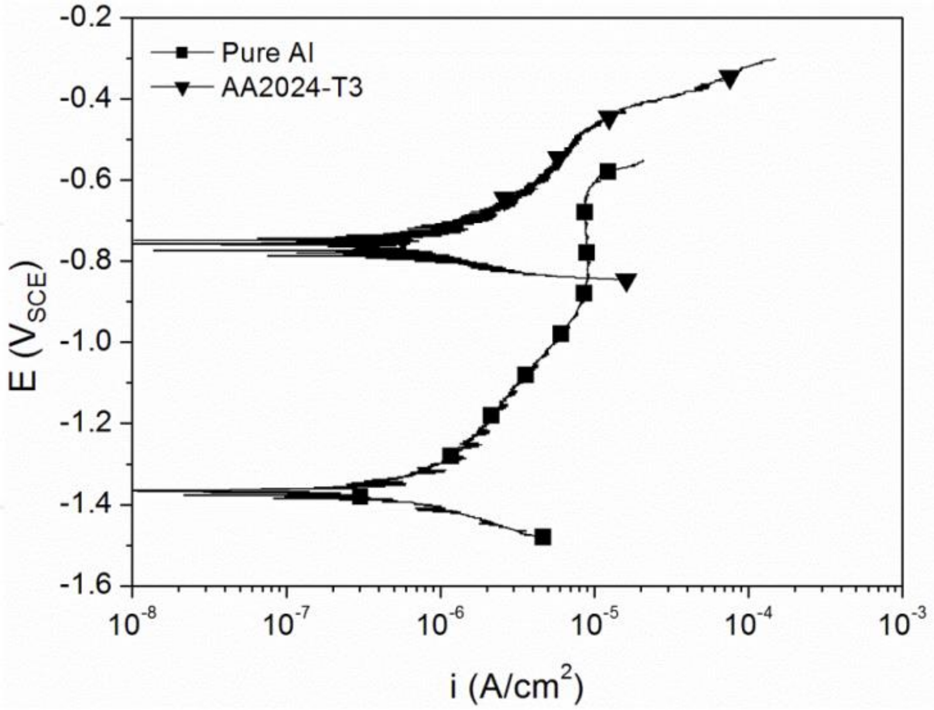

Figure 2.3 Corrosion potentials of pure Al and AA2024-T3 [9]

Different alloying elements exhibit various electrochemical behaviors which in turn has different effects on corrosion resistance of aluminum alloys. It has been shown that the presence of a more noble constituent could shift the corrosion potential of aluminum toward a more noble value which suggests a lower corrosion rate [10] as we can see in Figure 2.3. Nevertheless, a more noble potential, in this case, does not certainly indicate a superior corrosion resistance as pitting processes, the major problem of aluminum alloys, are not only influenced by the overall corrosion potential but also the chemical composition and microstructural homogeneity [11].

A number of studies have been carried out over the past few decades until now with the aim of understanding the effects of alloying elements on pitting corrosion behavior of aluminum alloys using electrochemical techniques such as electrochemical impedance spectroscopy, potentiodynamic polarization or electrochemical noise measurement [12]. Table 2.1 summarizes the corrosion potentials of several intermetallic phases that are typically found in aluminum alloys. Recent developments in understanding the microstructure behavior of aluminum alloys have enabled advanced methods in anti-corrosion managements such as anodizing or conversion and organic coating systems; for example, using multi-functional inhibitors could suppress corrosion reactions more efficiently than using a mono-functional inhibitor. Electrochemical techniques have received a great interest in analyzing the effectiveness of corrosion protection methods in recent years. These techniques have been extensively employed in anti-corrosion applications [13], some of which are local electrochemical impedance spectroscopy (LEIS), scanning electrochemical microscope (SECM) or scanning vibrating electrode technique (SVET).

Table 2.1 Corrosion potentials of common intermetallic particles in aluminum alloys [14]

Phase	Corrosion Potential (mV_{SCE}) in 0.1M NaCl
Al_3Fe	−539
Al_2Cu	−665
Al_6Mn	−779
Al_3Ti	−603
$Al_{32}Zn_{49}$	−1004
Mg_2Al_3	−1013
$MgZn_2$	−1029
Mg_2Si	−1538
Al_7Cu_2Fe	−551
Al_2CuMg	−883
$Al_{20}Cu_2Mn_3$	−565
$Al_{12}Mn_3Si$	−810
Al-2%Cu	−672
Al-4%Cu	−602

2.1.1. General corrosion performance of various aluminum classes

Generally, pitting corrosion of aluminum alloys is governed by several electrochemical reactions. Therefore, most of the studies relating to corrosion measurement and protection are mainly based on electrochemical techniques. The general corrosion resistance and mechanical performance of various classes of aluminum alloys can be summarized as below:

1xxx series alloys: Controlled unalloyed (pure) composition. 1xxx series have very high corrosion resistance due to their high impurity. However, the use of such alloys is limited to specialist applications where high corrosion resistance and ductility are required such as electrical or chemical industries. 1xxx is sometimes used in lightly stressed application but mainly serves as feedstock for secondary alloy production.

2xxx series alloys: have a sizable amount of copper, which is the principle alloying addition, although other elements, especially magnesium, may present. The appreciable solubility of copper contributes to the high mechanical strength, which could exceed 500MPa depending on temper conditions. 2xxx series alloys are widely used in aerospace applications where their high strength is valued. However, the high solubility of copper also in turn decreases the corrosive resistance of the alloy. This is mainly due to the position of copper in the galvanic series table, which accelerates pitting corrosion by forming copper clusters:

$$3Cu^{2+} + 2Al = 2Al^{3+} + 3Cu(cluster) \qquad (2.5)$$

3xxx series alloys: alloyed mainly with manganese, which has a low solubility but can enhance corrosion performance when forming solid solution in aluminum. 3xxx series have a broad of applications, for example, in architecture, due to their relatively good corrosion resistance and moderate strength (~110MPa). They are also suited for applications working at elevated temperatures such as heat exchanger in vehicles and power plants.

4xxx series alloys: typically alloyed with silicon. These alloys are mainly found as filler substance and are predominantly used in welding rods or brazing sheet.

5xxx series alloys: magnesium is the principle element added. It has considerable solubility in aluminum, which strengthens mechanical properties. 5xxx series have appreciably good corrosion resistance making them ideal materials for structures exposed to aggressive environments such as marine vessels, boat hulls, gangplanks.

6xxx series alloys: alloyed with magnesium and silicon. The present of silicon lowers the melting point of aluminum and improves fluidity when molten (which is why silicon is the principle alloying element for cast aluminum products). These alloys have appreciable resistance to corrosion, immunity to stress corrosion cracking and are weldable. They are widely used in automotive industry and structural applications where high mechanical strengths are required (tensile strength of 6xxx could exceed 300MPa).

7xxx series alloys: zinc is the key alloying element while other elements such as copper, magnesium, chromium may be included. 7xxx series are the strongest class of aluminum alloys and thus is extensively used in the construction and aerospace industry. A tensile strength of 580MPa is possible. However, 7xxx series are highly susceptible to localized corrosion in chloride containing environment. Such alloys are not suitable for marine applications until their corrosion performance and stress corrosion cracking resistance are improved.

8xxx series alloys: include a sizable amount of Lithium. These alloys have specific high strength and stiffness when properly heat-treated. The first generation of 8xxx series exhibited high corrosion resistance, but it is susceptible to intergranular corrosion. Research and development are ongoing to overcome this challenge and extend 8xxx potential for widespread usage in aviation applications.

2.2 Pitting morphology and characterization

Optical techniques were used early by some researchers to determine the pitting probability [15, 16]. Image processing was applied to analyze the affected areas for characterizing pitting corrosion. However, this method was virtually impossible to determine pit depth, which is considered as the most important parameter in evaluating pit, and pit shape below the surface. Recent methods focusing on pit depth and shape can be classified as [17]:

- Vertical sectioning.
- Analyzing by Scanning Electron Microscopy (SEM) and Atomic Force Microscopy (AFM).
- Characterizing by Confocal Laser Scanning Microscopy.

2.2.1 Vertical Sectioning

Pit morphology characterization has been widely determined by random vertical sectioning by several researchers [18-22]. Codaro, Nakazato et al. [18] proposed a method for morphology characterization by defining shape, size, and population of pits using a well-known shape descriptor, the area-box (AB) parameter as can be seen in Figure 2.4. This parameter is described as the ratio of pit area and the rectangular bounding it. Silva et al. [19, 20] applied this method and reported that:

- Pits grow more rapidly in depth than in width, and the widest pits are also the deepest
- Pits are predominantly conical or quasi-conical and irregular morphology.
- Pit morphology evolution from hemispherical or conical to irregular (or ramified) shape.

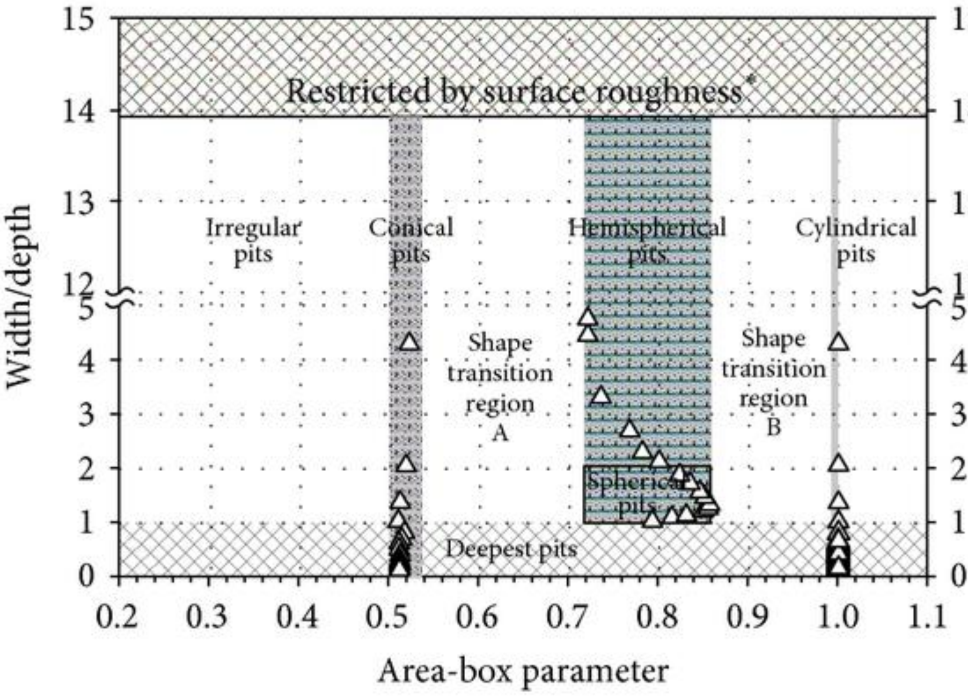

Figure 2.4 Pit morphology classification [22]

Ribeiro et al. [21] suggested that dissolution rate is higher at pit wall than at pit bottom. At short time immersion, pits are predominantly hemispherical then develop to near conical and hemispherical shape; cylindrical pits are not found. Pereira et al. [22] analyzed the shape of pits on the surface using the AB parameter and introduced the surface corrosion ratio to describe the evolution of pitting corrosion.

2.2.2 Analyzing by Scanning Electron Microscopy (SEM) and Atomic Force Microscopy (AFM)

Some attempts have been made to characterize pits in three-dimensional models and analyze pits induced stresses using SEM or AFM in conjunction with Finite Element Analysis [23, 24]. SEM or AFM images are imported to a NURB modeling software; Rhinoceros, to create a 3-D pitting surface. The height of the pitting surface is scaled down to match an actual pit depth measured by a commercial pit gauge (Starret Pit Gauge). Figure 2.5 presents SEM images of corrosion pits and their reconstructed surfaces used in these studies.

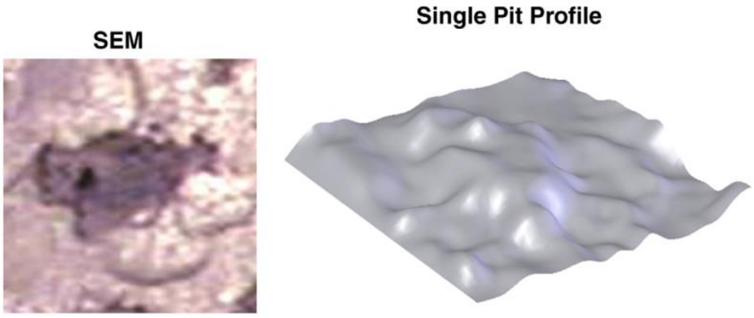

(a) 50 days

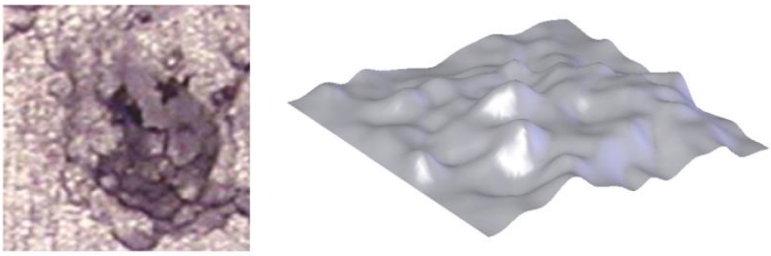

(b) 74 days

Figure 2.5 SEM images of corrosion pits and their reconstructed surfaces [23]

Cerit et al. [25] investigated the stress concentration factor (SCF) of corrosion pits using 3-D semi-elliptical models with different ratios of depth (a) and diameter ($2c$). The effect of secondary pits at the bottom was also examined. From the data obtained, a simple equation for estimating SCF was proposed:

$$K_t = \frac{[1+6.6(a/2c)]}{[1+2(a/2c)]} \tag{2.6}$$

They suggested that the aspect ratio $(a/2c)$ is the main parameter affecting SCF and the position of maximum stress can be either at the bottom or near the mouth of pits. Turnbull and Horner [26] developed a model to predict the evolution of corrosion cracks from pits, pit to crack transition and the early stages of crack growth in the short crack regime using 3-D models of hemispherical and bullet-shaped (U-shape in the cross section) pits with various pit depths on cylindrical specimens.

2.2.3 Characterizing by Confocal Laser Scanning Microscopy

In recent years, the use of confocal microscopy has proved to be the most practical tool for analyzing the morphological characteristics of pitting corrosion [17]. This tool has been successfully used to determine pit depth and allow more lucidity in 3-D observation of corrosion pits [27, 28]. Nevertheless, this tool has only been used in an extensive range of biological applications while it has not been widely utilized for metallic materials. Furthermore, there is a scarcity of 3-D volumetric quantification and modeling 3-D pit to evaluate stress-strain distribution.

2.3 Effect of grain orientation on corrosion behavior

During the early stage of solidification process, there are generally multiple nucleation points where atoms from the liquid, such as molten metal, begin to bond together and start to form crystals. The crystals expand by the progressive addition of adjacent atoms and grow until they impinge on other growing crystals. Therefore, most of engineering materials are in polycrystalline solid form unless there are special controlled conditions [29]. These crystals are generally referred to as grains. Grain is simply a crystal with arbitrary orientation since its evolution was obstructed by contacting with adjacent grains. The arbitrary orientation of each grain introduced chemical and mechanical heterogeneity in engineering materials even in most pure metals or single-phase alloys, which have the same chemical constitution and crystalline structure. The distribution of crystallographic orientations of a polycrystalline material is called texture. There are various qualitative and quantitative techniques to characterize texture of materials. Among quantitative techniques, diffraction technique using X-ray or backscatter electron signals is the most widely used method [30]. The grain orientation of materials was demonstrated to have a strong influence on material properties such as anisotropy mechanical behaviors of yield strength, ultimate tensile strength [31], crack growth direction [32], oxidation [33] and adsorption [34]. Several studies focused on the pitting behaviors of single crystal or polycrystalline in pure form due to its simplicity and described the relationship between crystal orientation and dissolution rate. Yu and Natishan [35] studied corrosion of single fcc Aluminum crystals and reported that pitting potential of single crystal fcc Aluminum in 0.5M NaCl solution reduced in the order $\{001\} > \{110\} > \{111\}$. It indicates the dissolution rate and corrosion severity of pure Al crystals increase in the order $\{001\} < \{110\} < \{111\}$. Davis [36] also demonstrated that dissolution rate of pure Al in HCl is highest at planes close to $\{001\}$.

Koroleva et al. [37] observed small facets on the grain structure of pure Aluminum after alkaline etching (Figure 2.6). These facets have distinct texture depending on from which grain orientation they initiated. They also concluded that $\{334\}$ grain, which is close to (111) orientation, has the highest dissolution rate compared to other orientations. In contrast, Takayama [38] stated that corrosion severity of pure Al in HCl solution is higher on $\{001\}$ planes at low concentration of HCl while $\{111\}$ planes corrode faster at high concentration. On the other hand, Seo, Ryu et al. [39] reported that corrosion rates of single Al crystals show little dependence on crystal orientation after subjected to cathodic polarization. Based on the observed results, they proposed a model to describe the transient of pit shape with different orientations.

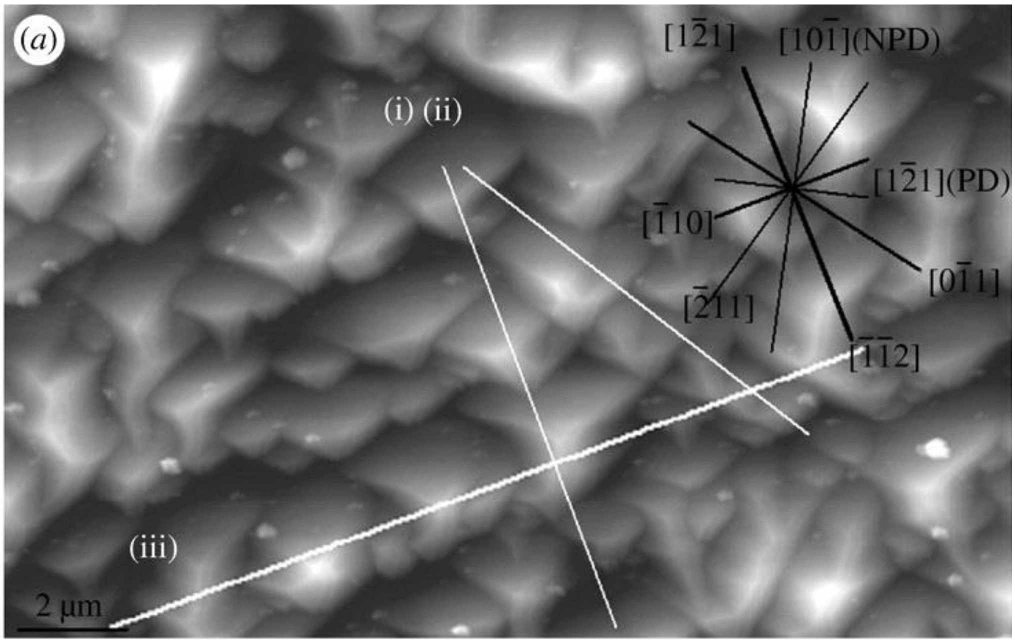

Figure 2.6 Two-dimensional atomic force image with prominent crystallographic directions identified [37]

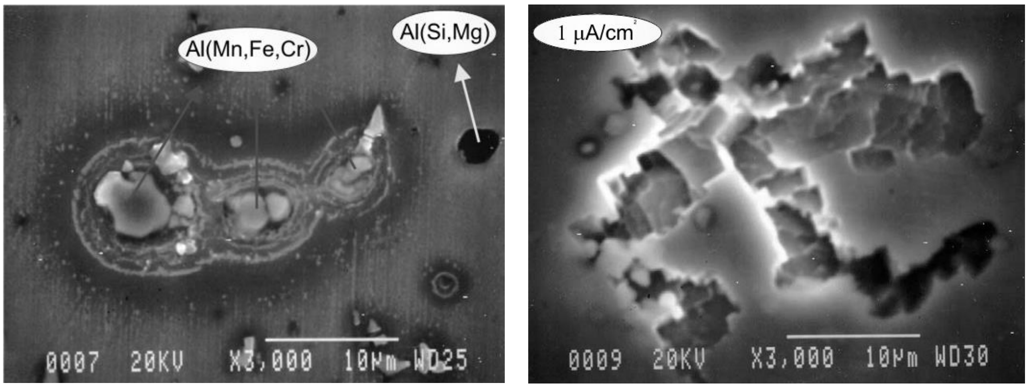

Figure 2.7 SEM images of hemispherical pit and crystallographic pit of AA5083 tested in 3.5% NaCl solution [40]

Due to the complexity of material-environment interactions, various observations were reported which emphasize the importance of alloying elements and microstructure of materials. Aballe [40] investigated corrosion process of AA5083 in aerated 3.5% NaCl solution and reported that there are two types of pitting form occurred in Aluminum alloys, namely hemispherical pitting and crystallographic pitting as shown in Figure 2.7. Localized corrosion process around Al(Mn, Fe, Cr) precipitates results in the formation of hemispherical pits while the initiation of crystallographic pits required anodic polarization at current density above a critical level. The morphology of crystallographic pits indicates a strong influence of crystal orientation on corrosion behavior of Aluminum alloys. A number of studies have been carried out to investigate the effects of microstructures on the orientation dependence of corrosion behavior of polycrystalline copper [41], Inconel [42, 43] or stainless steel [44] using EBSD technique. However, there was a scarcity of research carried out on polycrystalline Aluminum alloys to investigate the orientation dependence of corrosion processes.

2.4 Pitting corrosion fatigue models

Under a corrosive environment, it has been shown that cracks could initiate from pits under fatigue loading conditions while pitting processes are significantly enhanced due to the application of cyclic stresses. Moreover, pitting corrosion in combination with fatigue severely affects the integrity as well as service life of structures operating in offshore conditions. Therefore, several models have been proposed and developed in order to understand pitting corrosion fatigue mechanisms and provide a life prediction of materials. Linear Elastic Fracture Mechanics (LEFM) theories are generally applied to investigate corrosion fatigue behavior of materials. Hoeppner [45] proposed a model to identify critical pit depth for a mode I (tensile separation) crack to initiate under corrosion fatigue environments. This model combined both pit growth concept, which was proposed by Godard [46], and LEFM theories to provide a corrosion fatigue life prediction. The stress intensity factor of a hemispherical pit was estimated by using the equation of a half penny-shaped crack:

$$K = 1.1\sigma\sqrt{\pi(a/Q)} \tag{2.7}$$

where, σ represents the applied stress, a represents the length of pit and Q is a geometry constant. The time for pits to reach critical pit depth was determined by pit growth model of Godard as $t = (d/c)^3$ where d is the pit depth and c is an empirical constant.

Following this model, Lindley et al. [47] introduced a stress intensity threshold where fatigue cracks could initiate from pits:

$$\Delta K_{th} = \frac{\Delta\sigma\sqrt{(\pi a)}[1.13-0.07(a/c)^{1/2}}{[1+1.47(a/c)^{1.64}]^{1/2}} \tag{2.8}$$

where, $\Delta\sigma$ represents stress range, a and c are the major and minor of semi-elliptical pit respectively.

Kawai and Kasai [48] developed a model to determine the permissible stress range of materials under corrosion fatigue condition. Kondo [49] proposed a corrosion fatigue life prediction based on critical pit depth and corrosion pit growth rate. All of these models simplify pits as hemispherical or semi-elliptical shapes and are material dependent. The stress intensity threshold is determined empirically based on experimental data. These models did not address the mechanisms of crack initiation from pits, and they are only applicable in which LEFM conditions are satisfied.

Several models were then introduced which take into account the mechanisms of pitting corrosion fatigue and environmental effects. Fong et al. [50] developed a crack propagation mechanism for stage I (shear driven) corrosion fatigue crack based on the intrusion and extrusion activities of crack tips. T. Magnin [51] investigated the influence of hydrogen concentration on local deformation of crack tip. Other authors [52, 53] considered the effects of loading ratio, crack closure and anodic dissolution on corrosion fatigue crack growth mechanisms. G. Henaff and J. Petit [54] suggested that the crack growth rate under a corrosive environment could be determined by the summation of fatigue effects and stress corrosion cracking or crack tip environmental effects whichever is higher.

The application of LEFM on corrosion fatigue behavior of materials has shown certain advantages in estimation of corrosion fatigue life and stress intensity threshold. However, some authors (K. J. Miller and E. R. de los Rios [55]; Philips and Newman [56]) recognized that short corrosion fatigue crack (10µm-1mm) could initiate and propagate at stress intensity range lower than the predicted threshold which subsequently leads to overestimation of fatigue life. The characteristics of short crack growth are shown in Figure 2.8. According to ASTM standard E647, cracks are considered as being small if (1) their size is small compared to microstructural dimension such as grain size (a continuum mechanics limitation), or (2) their size is small compared to the plastic zone size ahead of crack tip (a linear elastic fracture mechanics limitation), or (3) they are small in physical meaning (<1 mm). In this report, the third definition of small crack is applicable to distinguish it with long crack.

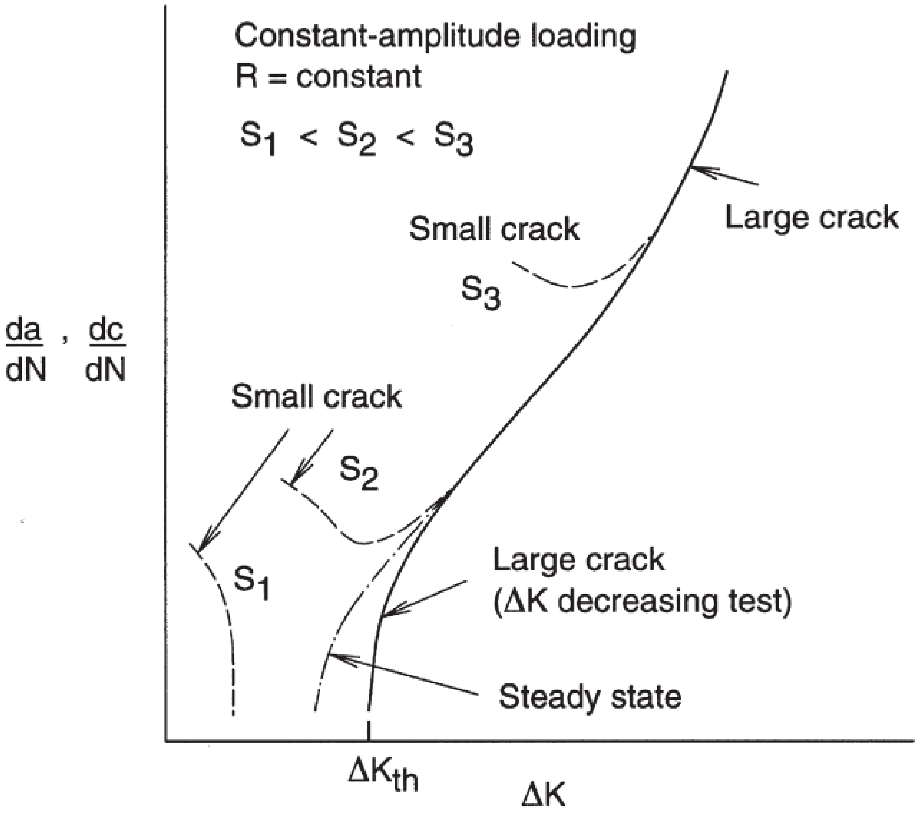

Figure 2.8 Crack growth behaviors of short and long crack [56]

Many factors are attributed to the invalidation of LEFM and stress intensity threshold in the short crack growth regime including plasticity effects, localized corrosion interactions, crack closure or microstructural defects. Piascik and Willard [57] noticed that cracks nucleated from corrosion pits tend to propagate intergranularly until they reach a critical length and then switch to transgranular propagation. Several researchers have attempted to understand the behavior of short crack growth and improve corrosion fatigue models for life prediction. J.C. Newman [58] applied elastic-plastic fracture mechanics (EPFM) theories to proposed a model describing small crack growth behaviors. Models based on microstructural fracture mechanics (MFMs) was extensively employed to characterize the behavior of short crack growth [59]. Akid et al. [60] investigated short fatigue crack growth in chloride environments and proposed a short crack growth model as follow:

$$\frac{da}{dN_{corrosionfatigue}} = \frac{da}{dN_{pitting}} + \frac{da}{dN_{EMSC}} + \frac{da}{dN_{EPSC}} \qquad (2.9)$$

where, EMSC and EPSC represent stage I shear crack and stage II short tensile crack respectively which are calculated as:

$$\frac{da}{dN_{EMSC}} = A(\Delta\gamma)^{\alpha}(d_i - a) \qquad (2.10)$$

$$\frac{da}{dN_{EPSC}} = B(\Delta\gamma)^{\beta}a - D \qquad (2.11)$$

in which, a is crack length, d_i is microstructural dimension, $\Delta\gamma$ is mechanical driving force, D is critical crack length and A, B, α, β are constants.

Cumulative damage mechanics are being extensively employed to predict corrosion fatigue life of various materials. Bolotin and Shipkov [61] considered pits as the initial fatigue cracks and predicted fatigue life of pre-corroded samples based on calculating the stress intensity factor in corresponding to crack growth rate. Beretta et al. [62] analyzed corrosion fatigue life of steel alloys operating in rainwater conditions. Palin-Luc et al. [63] investigated fatigue crack behavior of steel in seawater environments while Walde and

Hillderry [64] characterized corrosion damage of Aluminum alloys and provided a prediction for fatigue life based on continuum damage mechanics.

2.5 Mechanisms and kinetics of hydrogen assisted cracking

When fatigue loaded in a corrosive environment, crack growth resistance is downgraded by crack tip embrittlement due to the presence of hydrogen species generated by cathodic corrosion reactions. The existence of hydrogen in corrosive environments has been experimentally confirmed by polarizing the environment such that originally distributed hydrogen is accumulated at the negative electrode. A number of mechanisms have been proposed to explain the degradation of crack growth resistance caused by the presence of hydrogen species. The three most widely accepted interstitial mechanisms are: Hydrogen-enhanced localized plasticity (HELP), Hydrogen-enhanced decohesion (HEDE) and Adsorption Induced Dislocation Emission (AIDE). The mechanisms of these hydrogen assisted cracking theories are described as follows:

2.5.1 Hydrogen enhanced localized plasticity theory

The HELP mechanism is supported by observations that solute hydrogen facilitates dislocation motion ahead of crack tips by forming an enhanced plastic zone size [65, 66]. The fracture process exhibits plasticity phenomenon like reduction of material yield strength and micro-void coalescences rather than embrittlement. This mechanism assumed that hydrogen increases the plasticity of material in the vicinity of crack tip by interacting with the local stress field. Figure 2.9 illustrates the interaction of hydrogen with dislocation activities ahead of crack tip and crack propagation is caused by HELP. Hydrogen penetrates into the material ahead of crack tip and modifies the local stress field such that localized stress enhanced in one direction and reduced in the other direction. The dislocation interaction is also decreased in directions where stress field is lessened, which facilitates planar slip and restrains cross slip. Therefore, dislocation motions could occur at a lower stress level resulting in a reduction of tensile strength. Due to the present of high tensile stresses in front of crack tip, fracture surface shows ductile features such as dimples. However, this mechanism is only valid in a certain range of temperatures and strain rates. Contradictory results were observed at elevated temperatures and higher strain rates [67].

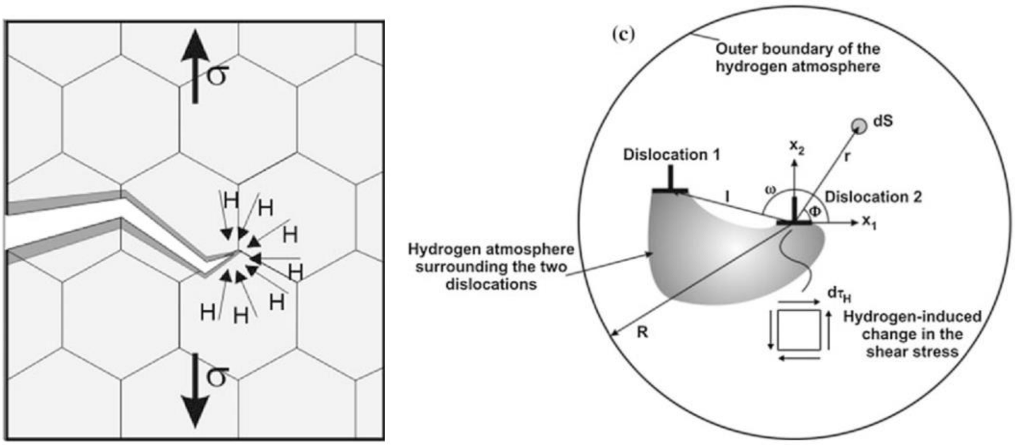

(a) (b)

Figure 2.9 (a) Schematic illustration of crack growth caused by HELP and (b) interaction of hydrogen with dislocations ahead of crack tip

2.5.2 Hydrogen enhanced decohesion theory

The second mechanism HEDE suggested that hydrogen adsorption weakened atomic bonds at crack tips resulting in decohesion (tensile separation) along cleavage planes or grain boundaries. Therefore, the fracture surface may exhibit either brittle intergranular or transgranular cleavage. This model was originally proposed by Troiano [68] and further improved by other authors [69, 70]. As demonstrated in Figure 2.10, hydrogen atoms diffuse into the crack tip and reduce cohesive energy of material ahead of crack tip ($U_{decohesion}$) which in turn lowers the tensile strength ($\sigma_{decohesion}$) of material. Consequently, the applied stresses caused material failure in a purely elastic manner. HEDE mechanism is supported by brittle characteristics similarly observed in solid-metal induced embrittlement and metal-vapor induced embrittlement where decohesion occurred in the absence of considerable local deformation.

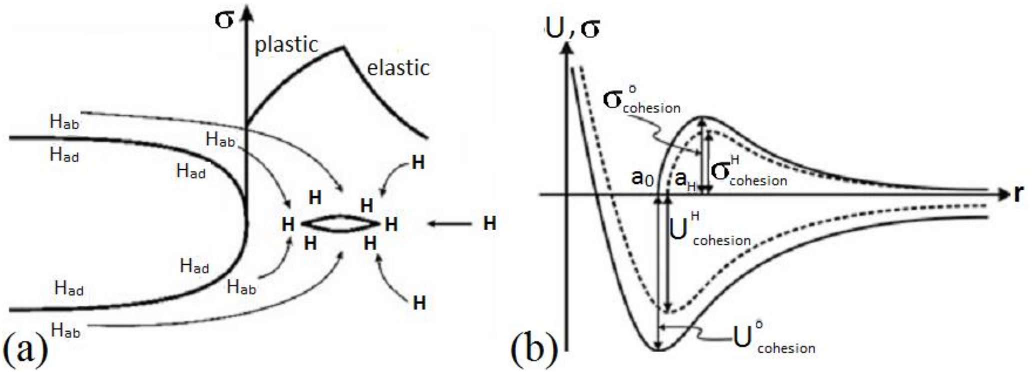

Figure 2.10 (a) Schematic diagram of crack propagation by HEDE and (b) cohesive strength $U_{decohesion}$ in corresponding with critical displacement (a_o is lattice parameter)

2.5.3 Adsorption Induced Dislocation Emission

S. P. Lynch [71] proposed the AIDE mechanism which considered hydrogen absorption and diffusion effects on crack growth behavior of Al-Zn-Mg alloys. This mechanism is based on fractographic observations such as extensive localized slip or nanoscopic dimples indicating that crack growth occurred by dislocation movement on suitable slip planes or void coalescence processes. There are certain resemblances between AIDE and HELP mechanisms as AIDE also suggested that hydrogen absorption affects the dislocation activities. Figure 2.11 demonstrated the AIDE mechanism. The author assumed that absorption of embrittling species weakened interatomic bonds and thereby enhanced dislocation emission at crack tip. Most of dislocation activity would result in crack advance on suitably inclined slip planes while a smaller portion would produce crack opening. Therefore, crack coalesces with microvoids ahead of crack tip at lower strains than in non-embrittling environment. The dimples formed by AIDE mechanism are smaller and difficult to resolve compared to those produced by HELP mechanism or by crack tip blunting in an inert environment. Crack growth activated by AIDE mechanism can be either intergranular or transgranular depending on which paths favor dislocation emission and void nucleation.

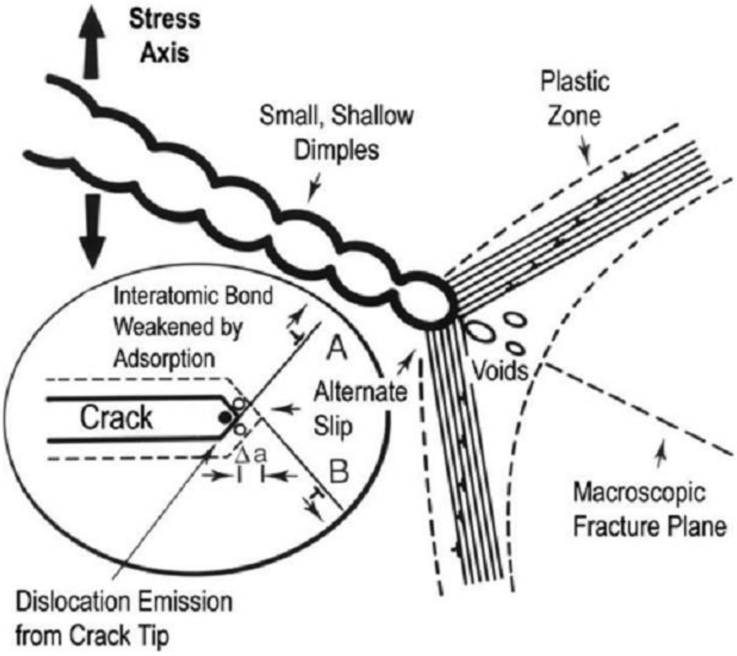

Figure 2.11 Schematic illustration of crack growth by AIDE mechanism

2.5.4 Grain boundary mechanisms

Regarding the intergranular crack propagation in an embrittling environment, there are two prominent mechanisms. The first one suggests that hydrogen can diffuse into grain boundaries and reduce cohesive energy between grains by impacting the structure of grain boundaries. The other mechanism assumed that segregation of alloying or impurity elements, for example, Mn, Si, S, and P, at grain boundaries contribute to decohesion process, which further facilitates crack advancement [72]. Over the last decade, several models combining HEDE and HELP mechanisms have been proposed to explain the nucleation and propagation of crack in an embritlling environment. Novak et al. [73] stated that the synergistic action of both HEDE and HELP mechanisms is involved in dictating intergranular fracture of steel. Barnoush et al. [74] conducted in situ electrochemical nanoindentation and observed a reduction in pop-in load induced by hydrogen. They concluded that the initiation of dislocation is dominated by HEDE, whereas HELP enhanced the propagation of dislocations. Similarly, other authors [75, 76] demonstrated that HEDE and HELP might concurrently influence the fracture processes of materials in a hydrogen containing environment.

2.6. Summary

In this chapter, fundamental theories and previous studies related to this research topic were reviewed. It can be seen that corrosion fatigue behavior of materials can be investigated in various aspects by different approaches. Fracture mechanics based modeling has been shown to be the most practical tool in investigating pitting corrosion fatigue behavior of materials. Nevertheless, depending on the way fracture mechanics are applied, these models require certain assumptions and simplifications which consequently disregard the 3-D nature of corrosion fatigue damage. This emphasizes that quantitative investigation of pitting corrosion damage in correlation with fatigue using three-dimensional models is of the essence. Various methods in characterizing pitting morphology were described. However, there is a lack of attempt to characterize both depth and shape of corrosion pits in 3-D models, especially the shape below the surface. Numerical simulation has been used to analyze pits induced stresses and to characterize pit morphology using 3-D models. Three-dimensional pitting surfaces were reconstructed using AFM or SEM based technique. However, these techniques have certain limitations as AFM is able to measure the height of surface but it is very poor at measuring sharp edges while SEM just can reveal the contrast of surface height and slope but cannot measure the actual height or depth of corroded surface [77]. Confocal microscopy has been proven to be an efficient tool in 3-D characterization of corrosion pits. In this research, the ability of 3-D characterization and volumetric measurement provided by confocal microscope has been shown to be a great assistance in characterizing corrosion damage and quantifying the effects of pit induced stresses on aluminum alloys. Combining confocal microscopic characterization with numerical modeling provides better understanding in corrosion process and further elucidates the influence of pits on stress-strain concentration.

In combination with fatigue, there is a lack of supporting evidence where and when critical fatigue cracks initiate under a corrosive environment. Largest or deepest pits are not always associated with fatigue crack initiation as reported by previous investigators [78, 79]. These observations indicate the importance of microstructures, grain orientation as well as the role of pit morphology, pit proximity on the corrosion fatigue behaviors of aluminum alloys. In an offshore environment, structures are naturally subjected to a great set of different loads and environmental actions. Nevertheless, the effects of microstructures and grain texture on pitting corrosion and anisotropic fatigue performance of aluminum alloys have not been sufficiently investigated.

Recent developments in microstructural analysis and measurement using EBSD techniques have enhanced our understanding of corrosion and fatigue crack initiation mechanism as well as pit to crack transition to a great extent [80]. The effects of grain texture and surface morphology of corrosion pits on fatigue crack initiation can be analyzed by the use of Orientation imaging microscopy. Moreover, the preferred orientation of grains having high susceptibility to pitting can be identified that could offer an important contribution to corrosion resistance aspect. Corrosion inhibitors might be developed to restrict the corrosion processes of particular crystallographic facets that could, in turn, improve fatigue performance of structures operating in a corrosive environment. Several studies have demonstrated that crystallographic orientation has a strong influence on pitting corrosion and crack growth behaviors of materials. However, there is a lack of consensus regarding the orientation dependence of pitting corrosion as the critical potential that initiates crystallographic pitting depends not only on crystal orientation but also on the alloying elements and corrosion environments. Furthermore, there was limited number of research investigating the influence of crystal orientation on corrosion behavior of polycrystalline Aluminum alloys.

Fundamental understandings of mechanisms and kinetics of hydrogen embrittlement have been appreciably achieved thanks to advances in high performance theoretical tools as well as high-resolution experimental instruments. Nevertheless, there are still many controversies regarding the embrittlement mechanisms and kinetics involved, as they cannot be generally applied to all materials in a particular environment. In addition, characterization of pit to crack transition as well as crack propagation behavior in a corrosive environment needs to be further investigated to improve existing models.

References

1. Jones, D.A., *Principles and prevention of corrosion*. 1992: Macmillan.
2. Cicek, V. and B. Al-Numan, *The Corrosion Process and Affecting Factors*, in *Corrosion Chemistry*. 2011, John Wiley & Sons, Inc. p. 3-5.
3. J. R. Davis, et. al, *Metals Handbook*, volume 13, pages 104-122 and 583-609 nineth edition, ASM International, Ohio, 1987.
4. Foley, R.T., *Localized Corrosion of Aluminum Alloys—A Review*. Corrosion, 1986. **42**(5): p. 277-288.
5. Baboian, R., *Corrosion tests and standards: application and interpretation*. Vol. 20. 2005: ASTM international.
6. Sato, N., *An overview on the passivity of metals*. Corrosion Science, 1990. **31**(0): p. 1-19.
7. McCafferty, E., *Introduction to corrosion science*. 2010: Springer.
8. Sukiman, N., et al., *Durability and corrosion of aluminium and its alloys: overview, property space, techniques and developments*. 2012.
9. Sukiman, N.L., N. Birbilis, and R.G. Buchheit. *Corrosion maps for aluminium alloys: Defining property space and the role of microstructure and chemistry in corrosion*. in *Meeting Abstracts*. 2012. The Electrochemical Society.
10. Davis, J.R., *Corrosion of aluminum and aluminum alloys*. 1999: ASM International.

11. Birbilis, N., et al., *Inhibition of AA2024-T3 on a phase-by-phase basis using an environmentally benign inhibitor, cerium dibutyl phosphate.* Electrochemical and solid-state letters, 2005. **8**(11): p. C180-C183.
12. Boag, A., et al., *Corrosion of AA2024-T3 Part I: Localised corrosion of isolated IM particles.* Corrosion Science, 2011. **53**(1): p. 17-26.
13. García, S., et al., *Self-healing anticorrosive organic coating based on an encapsulated water reactive silyl ester: Synthesis and proof of concept.* Progress in Organic Coatings, 2011. **70**(2): p. 142-149.
14. Nick, B., T.H. Muster, and G.B. Rudolph, *Corrosion of Aluminum Alloys*, in *Corrosion Mechanisms in Theory and Practice, Third Edition*. 2011, CRC Press. p. 705-736.
15. Itzhak, D., I. Dinstein, and T. Zilberberg, *Pitting corrosion evaluation by computer image processing.* Corrosion Science, 1981. **21**(1): p. 17-22.
16. Rokhlin, S., et al., *Effect of pitting corrosion on fatigue crack initiation and fatigue life.* Engineering Fracture Mechanics, 1999. **62**(4): p. 425-444.
17. North Atlantic Treaty Organization, R. and O. Technology, *Corrosion fatigue and environmentally assisted cracking in aging military vehicles La fatigue-corrosion et la fissuration en milieu ambiant des véhicules militaires vieillissants*. 2011, [Neuilly-sur-Seine Cedex]: N.A.T.O., Research and Technology Organization.
18. Codaro, E.N., et al., *An image processing method for morphology characterization and pitting corrosion evaluation.* Materials Science and Engineering: A, 2002. **334**(1–2): p. 298-306.
19. Silva, J.W.J., et al., *Morphological analysis of pits formed on Al 2024-T3 in chloride aqueous solution.* Applied Surface Science, 2004. **236**(1–4): p. 356-365.

20. Silva, J.W.J., et al., *Influence of chromate, molybdate and tungstate on pit formation in chloride medium.* Applied Surface Science, 2005. **252**(4): p. 1117-1122.
21. Ribeiro, R.B., et al., *Morphology Characterisation of Pitting Corrosion on Sensitized Austenitic Stainless Steel by Digital Image Analysis.* ISRN Corrosion, 2013. **2013**: p. 7.
22. Pereira, M.C.S., Jose W. J.; Acciari, Heloisa A.; Codaro, Eduardo N.; Hein, Luis R. O., *Morphology Characterization and Kinetics Evaluation of Pitting Corrosion of Commercially Pure Aluminium by Digital Image Analysis.*
23. Pidaparti, R.M. and A.S. Rao, *Analysis of Pits induced stresses due to metal corrosion.* Corrosion Science, 2008. **50**(7): p. 1932-1938.
24. Pidaparti, R.M. and R.R. Patel, *Correlation between corrosion pits and stresses in Al alloys.* Materials Letters, 2008. **62**(30): p. 4497-4499.
25. Cerit, M., K. Genel, and S. Eksi, *Numerical investigation on stress concentration of corrosion pit.* Engineering Failure Analysis, 2009. **16**(7): p. 2467-2472.
26. Turnbull, A., D.A. Horner, and B.J. Connolly, *Challenges in modelling the evolution of stress corrosion cracks from pits.* Engineering Fracture Mechanics, 2009. **76**(5): p. 633-640.
27. G. O. Ilevbare, O.S., R. G. Kelly, and J. R. Scully, *In Situ Confocal Laser Scanning Microscopy of AA 2024-T3 Corrosion Metrology: I. Localized Corrosion of Particles. J. Electrochem. Soc. 2004 151(8): B453-B464;.*
28. Huang, Y., et al., *Quantitative correlation between geometric parameters and stress concentration of corrosion pits.* Engineering Failure Analysis, 2014. **44**(0): p. 168-178.
29. Callister, W.D. and D.G. Rethwisch, *Fundamentals of materials science and engineering*. Vol. 21. 2013: Wiley New York.

30. Wenk, H. and P. Van Houtte, *Texture and anisotropy*. Reports on Progress in Physics, 2004. **67**(8): p. 1367.
31. Banumathy, S., R. Mandal, and A. Singh, *Texture and anisotropy of a hot rolled Ti–16Nb alloy.* Journal of Alloys and Compounds, 2010. **500**(2): p. L26-L30.
32. West, E. and G. Was, *A model for the normal stress dependence of intergranular cracking of irradiated 316L stainless steel in supercritical water*. Journal of Nuclear Materials, 2011. **408**(2): p. 142-152.
33. Wiame, F., V. Maurice, and P. Marcus, *Initial stages of oxidation of Cu (111).* Surface science, 2007. **601**(5): p. 1193-1204.
34. Hümann, S., J. Hommrich, and K. Wandelt, *Underpotential deposition of cadmium on Cu (111) and Cu (100).* Thin solid films, 2003. **428**(1): p. 76-82.
35. Yu, S. and P. Natishan, *Critical factors in localized corrosion III.* by RG Kelly, PM Natishan, GS Frankel and RC Newman, Pennington, NJ, 1999.
36. Davis, B., P. Moran, and P. Natishan, *Metastable pitting behavior of aluminum single crystals.* Corrosion science, 2000. **42**(12): p. 2187-2192.
37. Koroleva, E., et al. *Crystallographic dissolution of high purity aluminium*. in *Proceedings of the Royal Society of London A: Mathematical, Physical and Engineering Sciences*. 2007. The Royal Society.
38. Takayama, Y., M. Sato, and H. Watanabe. *Crystallographic Orientation Dependence of Corrosion Behavior of 5N Purity Aluminum in Different Concentrations of HCl Aqueous Solutions*. in *ICAA13: 13th International Conference on Aluminum Alloys*. Wiley Online Library.
39. Seo, J.H., J.-H. Ryu, and D.N. Lee, *Formation of crystallographic etch pits during AC etching of aluminum.* Journal of the Electrochemical Society, 2003. **150**(9): p. B433-B438.

40. Aballe, A., et al., *Localized alkaline corrosion of alloy AA5083 in neutral 3.5% NaCl solution.* Corrosion Science, 2001. **43**(9): p. 1657-1674.

41. Lapeire, L., et al., *Effect of neighboring grains on the microscopic corrosion behavior of a grain in polycrystalline copper.* Corrosion Science, 2013. **67**: p. 179-183.

42. Schuh, C.A., K. Anderson, and C. Orme, *Rapid assessment of anisotropic surface processes: experiments on the corrosion of Inconel 600.* Surface science, 2003. **544**(2): p. 183-192.

43. Wang, S. and J. Wang, *Effect of grain orientation on the corrosion behavior of polycrystalline Alloy 690.* Corrosion Science, 2014. **85**: p. 183-192.

44. Shahryari, A., J.A. Szpunar, and S. Omanovic, *The influence of crystallographic orientation distribution on 316LVM stainless steel pitting behavior.* Corrosion Science, 2009. **51**(3): p. 677-682.

45. Hoeppner, D.W. *Corrosion fatigue considerations in materials selection and design. Invited keynote paper*. in *International Conference on Corrosion Fatigue*. 1971.

46. H. P. Godard, *The Corrosion of Light Metals*, John Wiley and Sons, New York, NY, USA, 1967.

47. Lindley, T., P. McIntyre, and P. Trant, *Fatigue-crack initiation at corrosion pits.* Metals technology, 1982. **9**(1): p. 135-142.

48. Kawai, S. and K. Kasai, *Considerations of allowable stress of corrosion fatigue (focused on the influence of pitting).* Fatigue & Fracture of Engineering Materials & Structures, 1985. **8**(2): p. 115-127.

49. Kondo, Y., *Prediction of fatigue crack initiation life based on pit growth.* Corrosion, 1989. **45**(1): p. 7-11.

50. Fong, C. and D. Tromans, *Stage I corrosion fatigue crack crystallography in austenitic stainless steel (316L).* Metallurgical Transactions A, 1988. **19**(11): p. 2765-2773.

51. Magnin, T. *Advances in corrosion-deformation interactions*. in *Materials science forum*. 1996. Trans Tech Publications.
52. Ritchie, R. and J. Lankford, *Small fatigue cracks*. 1986, The Metallurgical Society Inc., Warrendale, PA.
53. Gangloff, R., et al., *Chemistry and physics of fracture.* Martinus Nijhoff, Dordrecht, 1987: p. 612-645.
54. Magnin, T. and J. Gras, *Corrosion-Deformation Interactions.* Proceedings CDI, 1993. **96**.
55. Miller, K.J. and E. De Los Rios, *The behaviour of short fatigue cracks.* Mechanical Engineering Publications, P. O. Box 24, Northgate Avenue, Bury St Edmunds, Suffolk IP 32 6 BW, UK, 1986., 1986.
56. Newman Jr, J., E.P. Phillips, and M. Swain, *Fatigue-life prediction methodology using small-crack theory.* International Journal of fatigue, 1999. **21**(2): p. 109-119.
57. Piascik, R. and S. Willard, *The growth of small corrosion fatigue cracks in alloy 2024.* Fatigue & Fracture of Engineering Materials & Structures, 1994. **17**(11): p. 1247-1259.
58. Newman Jr, J., *Fracture mechanics parameters for small fatigue cracks.* Small Crack Test Methods, ASTM STP, 1992. **1149**: p. 6-28.
59. Wei, L., E. de Los Rios, and M. James, *Experimental study and modelling of short fatigue crack growth in aluminium alloy Al7010-T7451 under random loading.* International journal of fatigue, 2002. **24**(9): p. 963-975.
60. Akid, R., *Modelling environment-assisted short fatigue crack growth.* Advances in Fracture Resistance and Structural Integrity, 1994: p. 261-269.
61. Bolotin, V. and A. Shipkov, *Mechanical aspects of corrosion fatigue and stress corrosion cracking.* International Journal of Solids and Structures, 2001. **38**(40): p. 7297-7318.

62. Beretta, S., et al., *Corrosion–fatigue of A1N railway axle steel exposed to rainwater.* International Journal of fatigue, 2010. **32**(6): p. 952-961.

63. Palin-Luc, T., et al., *Fatigue crack initiation and growth on a steel in the very high cycle regime with sea water corrosion.* Engineering Fracture Mechanics, 2010. **77**(11): p. 1953-1962.

64. Van der Walde, K. and B. Hillberry, *Characterization of pitting damage and prediction of remaining fatigue life.* International Journal of Fatigue, 2008. **30**(1): p. 106-118.

65. Birnbaum, H.K. and P. Sofronis, *Hydrogen-enhanced localized plasticity—a mechanism for hydrogen-related fracture.* Materials Science and Engineering: A, 1994. **176**(1-2): p. 191-202.

66. Robertson, I., *The effect of hydrogen on dislocation dynamics.* Engineering Fracture Mechanics, 2001. **68**(6): p. 671-692.

67. Borchers, C., T. Michler, and A. Pundt, *Effect of hydrogen on the mechanical properties of stainless steels.* Advanced Engineering Materials, 2008. **10**(1 ‐ 2): p. 11-23.

68. Troiano, A.R., *The role of hydrogen and other interstitials in the mechanical behavior of metals.* trans. ASM, 1960. **52**(1): p. 54-80.

69. Oriani, R., *Hydrogen embrittlement of steels.* Annual review of materials science, 1978. **8**(1): p. 327-357.

70. Oriani, R., *A mechanistic theory of hydrogen embrittlement of steels.* Berichte der Bunsengesellschaft für physikalische Chemie, 1972. **76**(8): p. 848-857.

71. Lynch, S., *Mechanisms of hydrogen assisted cracking–a review.* Hydrogen Effects on Material Behaviour and Corrosion Deformation Interactions, 2003: p. 449-466.

72. Bechtle, S., et al., *Grain-boundary engineering markedly reduces susceptibility to intergranular hydrogen embrittlement in metallic materials.* Acta Materialia, 2009. **57**(14): p. 4148-4157.

73. Novak, P., et al., *A statistical, physical-based, micro-mechanical model of hydrogen-induced intergranular fracture in steel.* Journal of the Mechanics and Physics of Solids, 2010. **58**(2): p. 206-226.

74. Barnoush, A. and H. Vehoff, *In situ electrochemical nanoindentation: A technique for local examination of hydrogen embrittlement.* Corrosion Science, 2008. **50**(1): p. 259-267.

75. Robertson, I.M., et al., *Hydrogen embrittlement understood.* Metallurgical and Materials Transactions B, 2015. **46**(3): p. 1085-1103.

76. Wang, S., et al., *Hydrogen-induced intergranular failure of iron.* Acta Materialia, 2014. **69**: p. 275-282.

77. P. Russell, D.B., J. Thornton, *SEM and AFM: Complementary Techniques for High Resolution Surface Investigations.*

78. Sankaran, K.K., R. Perez, and K.V. Jata, *Effects of pitting corrosion on the fatigue behavior of aluminum alloy 7075-T6: modeling and experimental studies.* Materials Science and Engineering: A, 2001. **297**(1–2): p. 223-229.

79. Clark, P.N. and D.W. Hoeppner, *Pitting Behavior and Residual Fatigue Life of 2024-T3 Aluminum Considering Loading and Sheet Thickness*, in *Journal of the Mechanical Behavior of Materials*. 2002. p. 91.

80. Roach, M.D., et al., *An EBSD based comparison of the fatigue crack initiation mechanisms of nickel and nitrogen-stabilized cold-worked austenitic stainless steels.* Materials Science and Engineering: A, 2013. **586**: p. 382-391.

Chapter 3

Experimental Methodology

This chapter presents the details of experimental methods employed in this study. Firstly, the material information and sample preparation procedures are introduced. Secondly, the methods to evaluate mechanical performance, including tensile and fatigue testing, are elaborated. Finally, the principles of equipment pertaining to material and mechanical characterization are explained.

3.1 Material information

The aluminum alloys investigated in this study were AA7075-T6 and AA6061-T6 in the form of rolled sheet with the thickness of 4.06mm. T6 indicates the materials were solution heat treated and then artificially aged. Table 3.1 and 3.2 showed the chemical composition of these aluminum alloys provided by the supplied company.

Table 3.1 Chemical composition of AA7075-T6 (wt%)

Alloy	Si	Fe	Cu	Mn	Mg	Cr	Zn	Ti	Other, each	Other, total
Min			1.2		2.1	0.18	5.1			
Max	0.40	0.5	2	0.3	2.9	0.28	6.1	0.2	0.05	0.15

Table 3.2 Chemical composition of AA6061-T6 (wt%)

Alloy	Si	Fe	Cu	Mn	Mg	Cr	Zn	Ti	Other, each	Other, total
Min	0.40		0.15		0.80	0.04				
Max	0.80	0.7	0.4	0.15	1.20	0.35	0.25	0.15	0.05	0.15

3.2 Sample preparation for corrosion testing

3.2.1 Metallographic preparation

Prior to corrosion test, the specimens were first cut into rectangular pieces then ground with 400 grit SiC paper to remove all the sheared edges. After that, they were mounted in phenolic hot mounting resin. These specimen surfaces were then ground with subsequent use of 800 and 1200 grit SiC paper followed by fine grinding with 9-micron diamond suspension. Final polishing was finished by 3-micron diamond and colloidal silica 0.04-µm suspensions.

3.2.2 Etching technique

In order to reveal microstructural details, etching was performed prior to examination and characterization. Before etching, the samples were polished until the final step with colloidal silica 0.04-µm suspensions. The etching technique consists of two steps. Firstly, the samples were pre-etched in Keller's reagent (95mL H_2O + 2.5mL HNO_3 + 1.5mL HCl + 1.0mL HF) for 3 minutes to completely remove mechanical damage produced by polishing processes. Then, the samples were color etched by Weck's reagent (100mL H_2O + 1g NaOH + 4g $KMnO_4$) for 30 seconds to reveal the precipitates and grain boundaries.

3.2.3 Roughness measurement

Surface roughness of polished specimens for corrosion tests was measured using Surftest SJ 301 Stylus Profilometer to ensure the maximum surface roughness R_a less than 0.02μm. As shown in Figure 3.1, surfaces of reduced section of fatigue specimen were also polished with subsequent use of 800 and 1200 grit SiC paper such that maximum surface roughness R_a is less than 0.15μm to minimize the effects of roughness on fatigue performance.

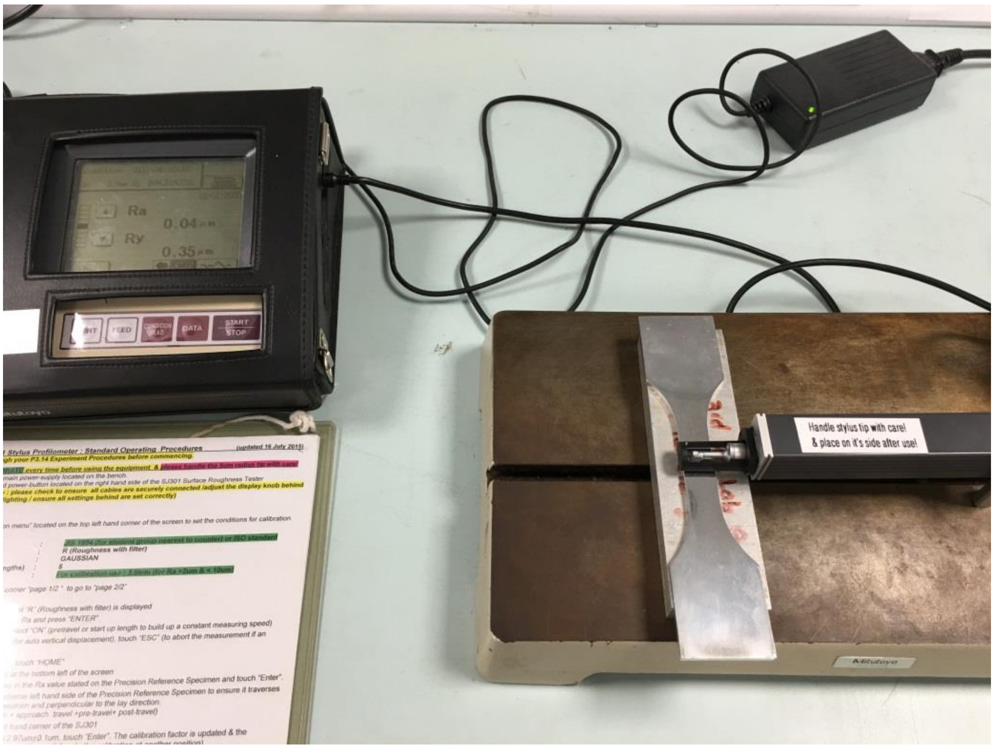

Figure 3.1 Surface roughness measurement

3.2.4 Preparing solution for evaluation of corrosion performance

Polished samples were exposed in simulated seawater 3.5% wt. NaCl solution in accordance with American Society for Testing and Materials (ASTM) standards G1-03 [1] and G46-94 [2]. Sodium chloride was mixed with deionized (DI) water obtained from a Millipore ultrapure water system to produce the testing solution. The pH value of this synthetic seawater solution was measured using a pH probe. The pH was then adjusted by adding HCl or NaOH buffer solutions until it was balanced at 8.2 as recommended by ASTM D1141 [3].

3.2.4 Cleaning and storage

The corroded specimens were subsequently rinsed in running water for 5 minutes and desmutted with nitric acid 70% concentration for 1 minute after immersion period. A Branson 8510 Ultrasonic Cleaner was used to clean the samples again with distilled water with the purpose of totally removing corrosion products. These samples were then dried by a dryer and stored in a dry cabinet until they were examined.

3.3 Mechanical testing

3.3.1 Tensile testing

Test specimens were cut from aluminum sheets with thickness of 4.06mm. Tensile tests were carried out using an INSTRON universal testing machine. An axial extensometer with 10mm gage length was attached on the central region of tensile specimens as shown in Figure 3.2 to accurately determine yield strength and Young’s modulus of tested materials. Displacement rate of tensile test was set up at 1mm/min. Ultimate strength, tensile yield strength and elastic modulus of tested materials were determined to estimate the amplitude of forces required for fatigue test.

Figure 3.2 Instron universal testing machine

3.3.2 Fatigue experiment

Fatigue tests were carried out at room temperature using MTS 810 Material Testing System. Force control mode with a frequency of 5 Hz was employed in this study. The dimensions of test specimens, which will be discussed later, were designed according to ASTM standards E466 [4] and E647 [5]. Surfaces of reduced section of fatigue specimens were polished with subsequent use of 800 and 1200 grit SiC paper such that maximum surface roughness R_a is less than 0.15μm to minimize the effects of roughness on fatigue performance.

In order to investigate the combination effect of fatigue load in conjunction with corrosive environment, an environmental chamber was designed according to ASTM F1801 [6] for conducting corrosion fatigue test. A peristaltic pump was used to circulate the test solution through the environmental chamber at constant flow rate 51 mL/minute to avoid erosion-corrosion phenomenon. NaCl 3.5% solution was pump into the bottom of environmental chamber and flows out by gravitational potential. The pH value of solution was adjusted to 8.2

prior to the test. Figure 3.3 illustrates the testing set-up for corrosion fatigue experiment in artificial seawater.

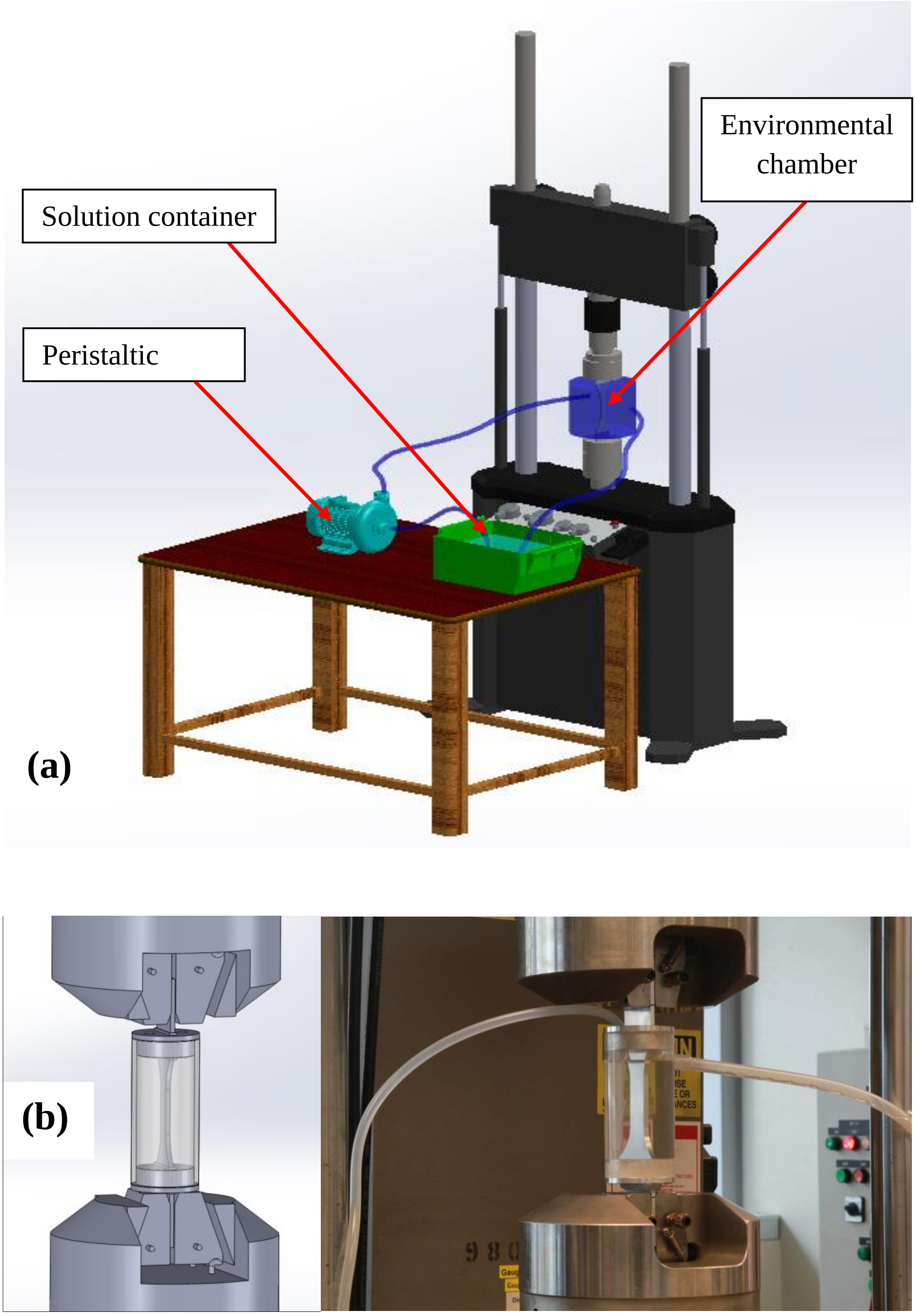

Figure 3.3 (a) Schematic illustration of corrosion fatigue set-up and (b) environmental chamber fitted on fatigue machine

Fatigue crack growth rate was measured by placing a high-speed camera in front of the MTS machine to monitor fatigue crack growth. A mirror was placed behind the specimen at 45° relative to the specimen surface. The mirrors would reflect the specimen surfaces such that the fatigue crack growth could be captured by the high-speed camera. The camera was setup to capture image at every few minute intervals in order to calculate crack length increment throughout the entire fatigue test. The images captured using the high-speed camera were then processed by image processing software, ImageJ. Previous experience was obtained from similar specimen configuration and testing apparatus to ensure that crack symmetry requirements are met consistently. Therefore, crack length measurement was made only on the front side of the sample. A LED light was placed at the front side of the specimen to increase the brightness such that the surface crack can be captured more clearly. Figure 3.4 shows the overall setup of the experiment.

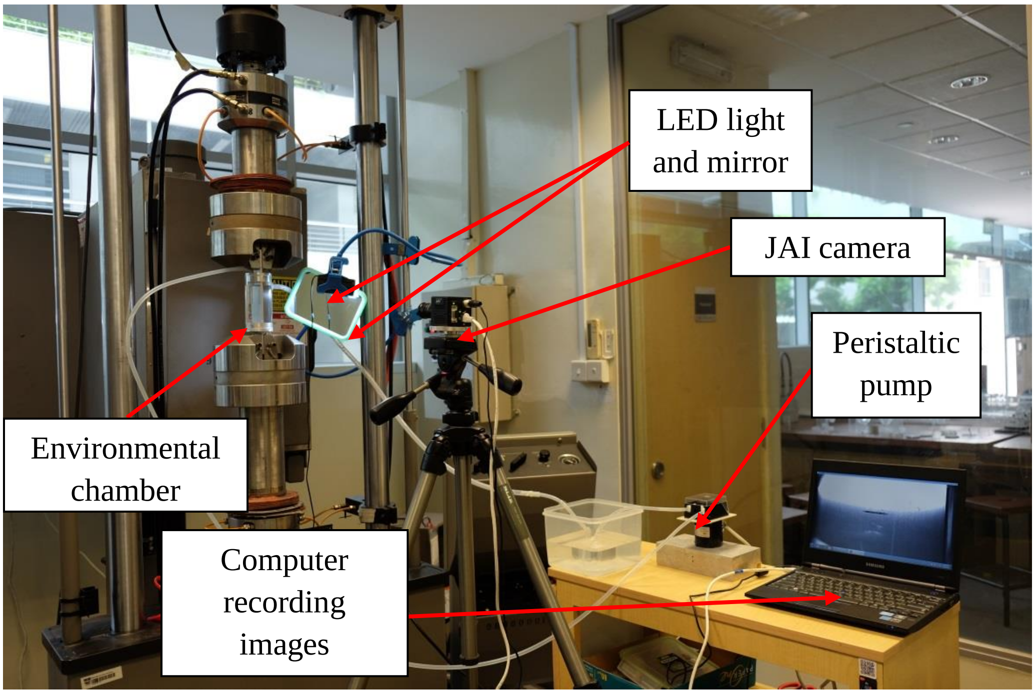

Figure 3.4 Overall setup of fatigue crack growth experiment

3.4 Characterization techniques

3.4.1 Confocal imaging microscopy

Confocal imaging can be described as a direct non-destructive serial optical sectioning of specimens. It allows for the generation of three-dimensional images and also for profiling of three-dimensional and multilayered structures. This allows for the accurate measurement of shapes and depths of pits that are required in this experiment. The principle of this technique is described in Figure 3.5. An image produced by a microscope just consists of a few in-focus planes while planes that are out of focus will become blurred. In a confocal microscope, only light come from well-focused planes is digitally recorded and stored in the computer. The out-of-focus light is cut off by one or a system of apertures. By changing the distance between the sample and objective lens step by step, the image stacks from each step are combined together to produce 3-D view of the sample. In this study, the corroded samples were examined by a 3-D confocal profilometry Sensofar PLμ to acquire three-dimensional views of the pitting surfaces. The data obtained from the confocal profilometry will then be processed for pitting characterization. Confocal data generated from the Sensofar PLμ software are set of x, y, z coordinates of every point on the surfaces of corroded samples with the resolution of 0.375μm in x and y directions and 0.1 μm in z coordinate, which represents the depth of corrosion pits. The obtained data will be simultaneously processed to quantify corrosion damage and characterize pitting morphology in 3-D. In recent years, the use of confocal microscopy has proved to be the most practical tool for analyzing the morphological characteristics of pitting corrosion. This tool has been used in a wide range of biological applications. However, it has not been widely utilized for metallic materials.

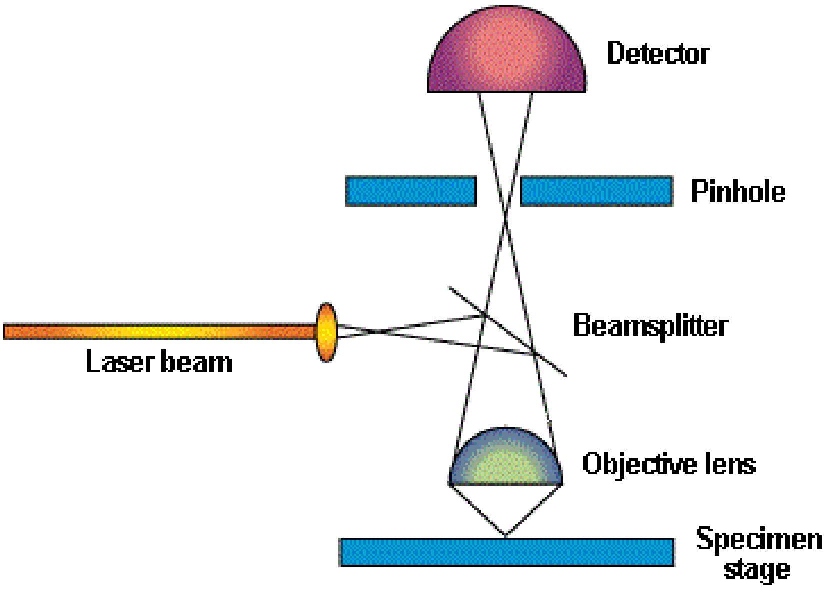

Figure 3.5 Principle of Confocal Imaging Microscopy [7]

3.4.2 Scanning electron microscopy

SEM is a versatile instrument for surface analysis and characterization of heterogeneous organic as well as inorganic materials. In the SEM, the investigated area is illuminated by a focused electron beam in two ways. The electron beam can scan across the surface of the sample from side to side in lines from top to bottom to create images or just stay at one interested area to analyze the required information. The images are formed by the beam position in conjunction with the acquired signals. As shown in Figure 3.6, there are various signals produced during the interactions between the electron beam and the atoms at the sample surface including secondary electrons, backscattered electrons, characteristic x-rays, specimen current, transmitted electrons and so on.

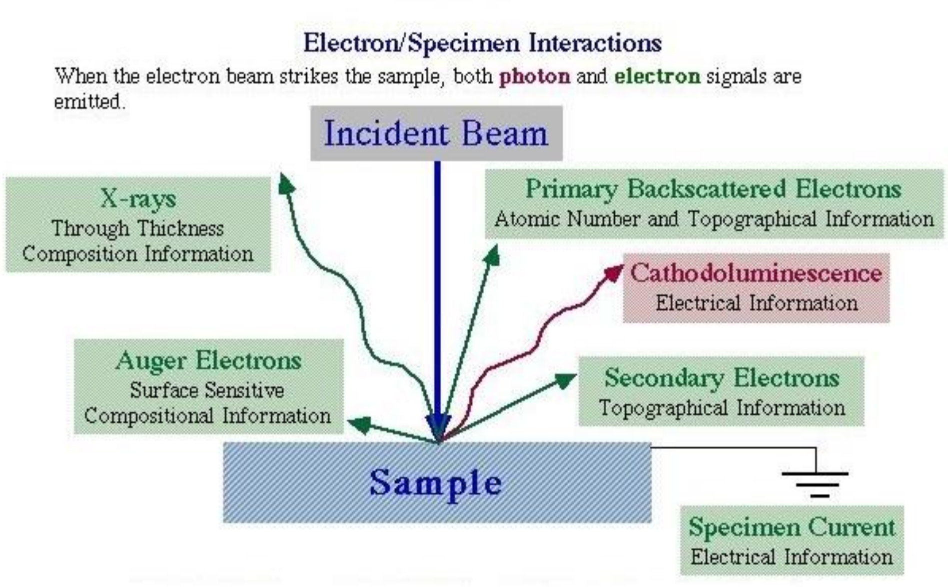

Figure 3.6 Signals produced by Electron-Specimen interactions [8]

These signals are acquired by corresponding detectors to reveal many characteristics of the investigated material such as chemical composition, crystalline structure, surface topography, etc. However, a single SEM machine is rarely equipped with detectors for all possible signals. The most common or standard of imaging signals are the secondary and backscattered electrons. As the electron beam is very narrow, the SEM machines can have a large depth of field, which creates the three-dimensional appearance of a two–dimensional image. This characteristic is very useful for analyzing the surface structure of the specimens. The magnification of SEM can vary from 20X to around 30000X with the selected area ranging from one square centimeter to five square microns. In the present study, a field emission scanning electronic microscopy (FESEM, JEOL JSM 7600F) equipped with EDS and EBSD detectors (Figure 3.7) was utilized to investigate corrosion fatigue damage and microstructural properties of aluminum alloys.

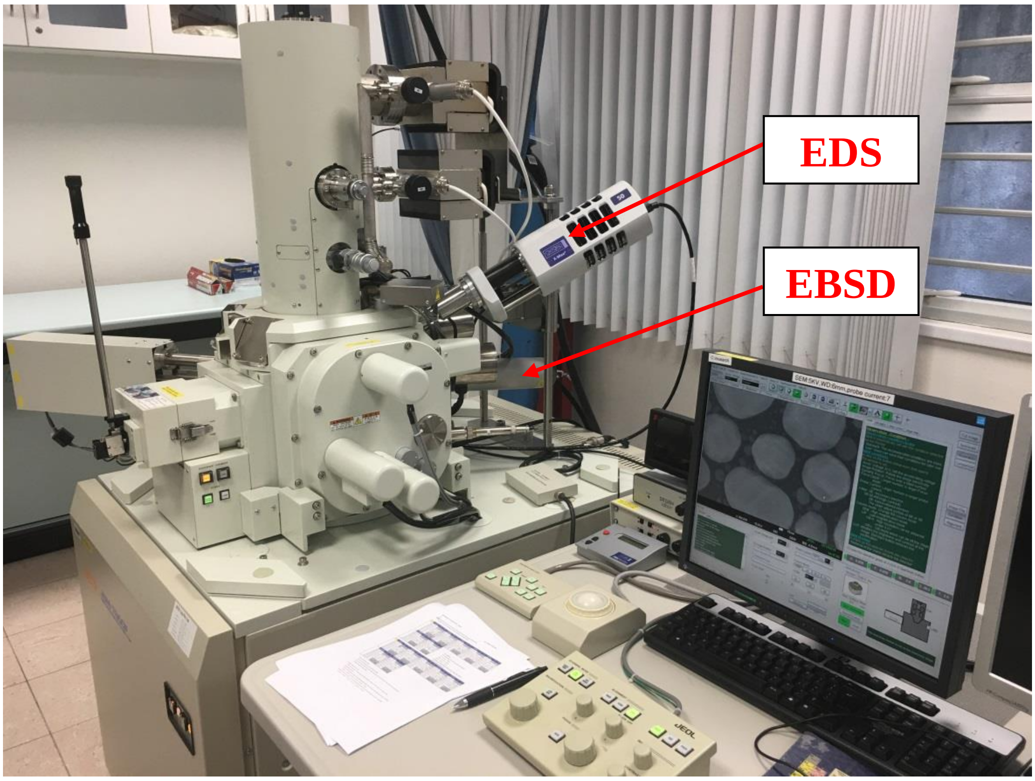

Figure 3.7 FE-SEM equipped with EDS and EBSD detectors

3.4.2.1 Energy-dispersive X-ray spectroscopy (EDS)

The elemental composition of different intermetallic particles in aluminum alloys was examined using EDS technique. For analyzing the chemical composition of the sample, a high energy beam of electrons or photons is focused on the sample surface to stimulate the emission of characteristic X-rays. The characteristic X-rays emitted from a specimen are converted to voltage signals by a detector and can be quantified by an energy dispersive spectrometer. These signals are then sent to an analyzer to acquire the elemental data of the sample [9].

3.4.2.2 Electron backscatter diffraction (EBSD) technique

EBSD is a powerful tool for microstructural analysis covering from macro (cm or mm) to nanometer scale. EBSD allows:

- Phase discrimination and identification
- Crystallographic Orientations

- Misorientations calculation
- Texture measurement
- Deformation/strain investigation
- Grain size and boundary types
- Fracture and failure analysis …

The principle of this technique is illustrated in Figure 3.8. A beam of electrons is directed onto a 70^0 tilted sample in a SEM. The electrons undergo various interactions with the atoms in the crystal lattice, and those which satisfy the Bragg condition ($n\lambda=2d.\sin\theta$) are channeled into two very open cones (almost flat discs). The cones intersect the phosphor screen and form the hyperbolae or Kikuchi bands which are captured by the camera and form electron beam scattering patterns (EBSP). Through band detection and Hough transform processes, Kikuchi patterns were indexed. After indexing, the orientation of the crystal lattice with respect to coordinates fixed in the sample is calculated which indicate crystal symmetry, orientation and any strain of the illuminated point. The grain mapping is constructed by moving electron beam or sample stage and repeating the whole process on the selected area.

Recent developments in microstructural analysis and measurement using EBSD techniques have enhanced our understanding of corrosion and fatigue crack initiation mechanism as well as pit to crack transition to a great extent [10]. In this study, the effects of grain texture and surface morphology of corrosion pits on fatigue crack initiation were analyzed by the use of EBSD. Furthermore, fatigue crack initiation and crack growth mechanisms were also investigated using EBSD technique.

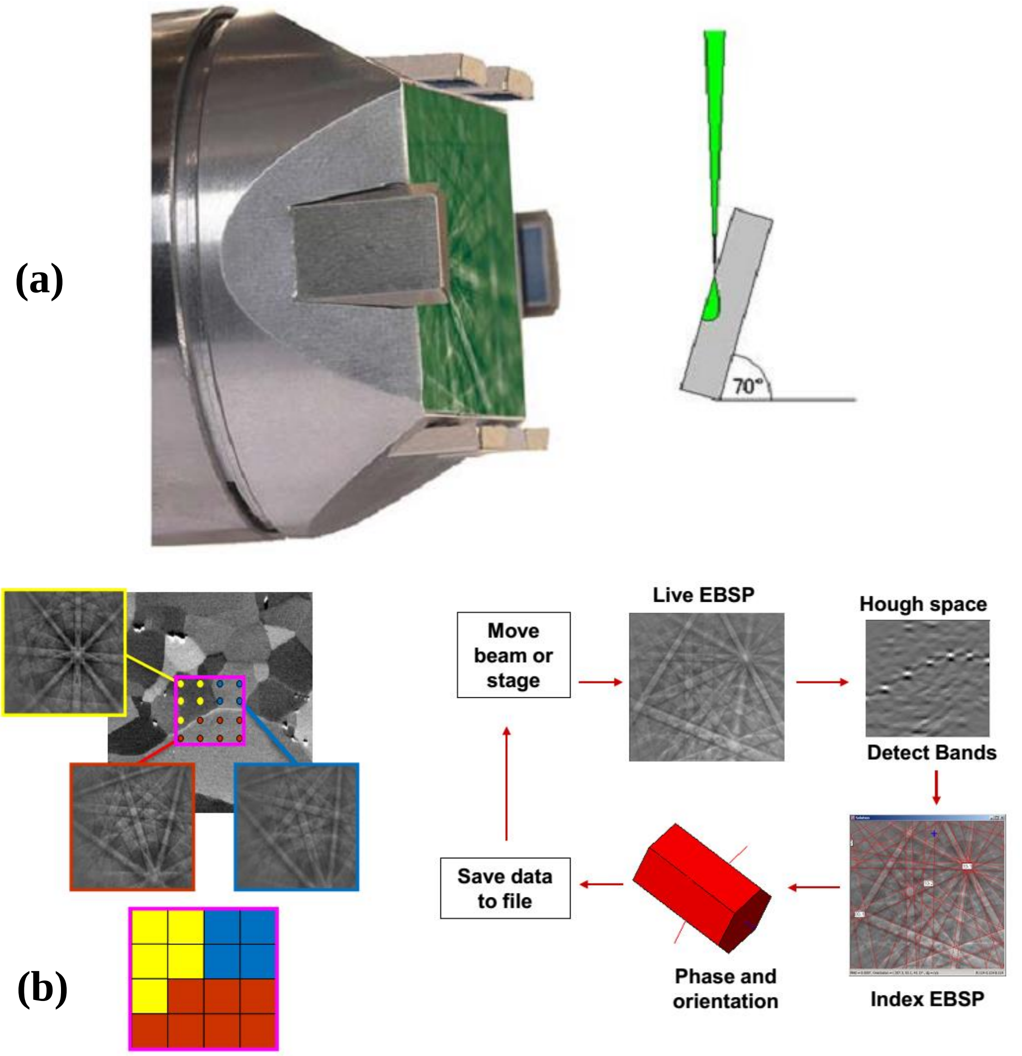

Figure 3.8 (a) SEM setup and (b) Mapping process to construct grains of selected area [11]

3.5 Summary

This chapter provides technical details of experimental methodologies used in this study. The underlying principles of characterization techniques were also discussed to provide useful information for pursuing further research on this topic.

References

1. Standard, A., *G1-03.* Standard Practice for preparing, cleaning, and evaluating corrosion test specimens, Annual Book of ASTM Standards, 2003. **3**: p. 17-25.
2. G46-94, A., *Standard Guide for Examination and Evaluation of Pitting Corrosion*. 2005, ASTM International West Conshohocken, PA.
3. D1141-98, A., *Standard Practice for the Preparation of Substitute Ocean Water*. 2008, ASTM International West Conshohocken, PA.
4. ASTM E466-07, *Standard Practice for Conducting Force Controlled Constant Amplitude Axial Fatigue Tests of Metallic Materials,* ASTM International, West Conshohocken, PA, 2007, www.astm.org.
5. Standard, A., *E647-11: standard test method for measurement of fatigue crack growth rates.* ASTM International, West Conshohocken, PA (USA), 2003.
6. ASTM F1801-97(2004), *Standard Practice for Corrosion Fatigue Testing of Metallic Implant Materials*, ASTM International, West Conshohocken, PA, 2004, www.astm.org.
7. http://www.cyto.purdue.edu/cdroms/micro1/7_spon/vaytek/fig1.gif.
8. Electron-Specimen Interactions ; Welcome to the world of the SEM; Iowa State University; http://www.eng.iastate.edu/~karie/.
9. Goldstein, J., *Scanning electron microscopy and x-ray microanalysis*. New York: Kluwer Academic/Plenum Publishers.
10. Roach, M.D., et al., *An EBSD based comparison of the fatigue crack initiation mechanisms of nickel and nitrogen-stabilized cold-worked austenitic stainless steels.* Materials Science and Engineering: A, 2013. **586**: p. 382-391.
11. http://www.ebsd.com/ebsd-explained/principle-components-of-an-ebsd-system.

Chapter 4

Morphological characterization of pitting corrosion of AA7075-T6

This chapter focuses on characterizing the morphological damage of pitting corrosion of aluminum alloy AA7075-T6, particularly in 3-D, and quantifying corrosion effects on pit induced stresses which are responsible for crack initiation. Confocal microscopy was utilized to characterize the morphology of corrosion pits with different times of immersion. Finite element analysis was carried out to evaluate the intensity of stress-strain concentration factor caused by the presence of pits. A method that simplified the complex and tortuous morphology of pits into idealized shapes was proposed in order to evaluate the equivalent effect of pit induced stresses which are responsible for stress concentration and crack initiation. Finite-element analysis showed that using semi-ellipsoid with equal surface area and maximum pit depth was a good approximation in predicting stress-strain distributions on corrosion surface and estimating stress-strain concentration factor caused by the presence of pits.

4.1 Introduction

Pitting corrosion has been a great concern for structural integrity of several materials that are used in offshore, civil and aerospace applications. It has been known as a dominant factor on the reduction of service life of many structures and other equipment operating in corrosive conditions, especially in an offshore environment. A number of studies have been conducted using various techniques to elucidate the pit initiation, propagation mechanisms and characterize corrosion behavior of metals under corrosive environment. Optical technique was used by early researchers to determine pitting probability [1]. This method was showed to be useful in analyzing the affected areas. Nevertheless, it was almost impossible to identify pit profile below the surface and pit depth, which are considered as the most critical parameters in characterizing pitting corrosion [2]. Recent methods focusing on pit depth and shape have been extensively applied by several investigators to develop an in-depth analysis. Codaro, Nakazato et al. [3] introduced a method for morphology characterization using a well-known shape descriptor, the area-box (AB) parameter, which is defined as the ratio between pit area and a minor rectangular area surrounding pit. Pit profile was determined after arbitrarily vertical sectioning corroded specimens. Silva et al. [4, 5] observed that pits are mainly conical, quasi-conical and grow more rapidly in depth than in width. In addition, there is a transformation of pit shape from hemispherical or conical to ramified shape with increasing time of immersion. Sheng-li et al. [6] analyzed the shape of pits on the surface using AB parameter and introduced a surface corrosion ratio to represent the progression of pitting corrosion. This method seems to be efficient to characterize pits in terms of depth and shape. However, this method cannot capture the intrinsic complexity of pit shape which is in three dimensions as randomly getting vertical cross sections of pits may not be accurate since one pit could have various shapes at different cross sections.

Numerical simulation has been extensively used to characterize pits in three-dimensional models and analyze pits induced stresses. Cerit et al.

systematically investigated the stress concentration factor (SCF) of corrosion pits using 3-D semi-elliptical models with different ratios of depth and diameter [7, 8]. Turnbull et al. developed a model to predict the evolution of corrosion cracks from pits, pit to crack transition and the development of small crack using 3-D models of hemispherical and bullet-shaped pits with various pit depths on cylindrical specimens [9, 10]. SEM or AFM images were utilized by some authors to reconstruct the pitting surface into three-dimensional models [6, 11-16]. It became clear that this method has some limitations as AFM is able to measure the height of surface, but it is very poor at measuring sharp edges while SEM just can reveal the contrast of height and the slope of the surface but cannot measure the height of the surface [17].

Confocal microscopy has been proved to be an efficient tool in 3-D characterization of corrosion pits [2].This tool has been successfully used to determine pit depth and allow more lucidity in 3-D observation of corrosion pits [18, 19]. Combining confocal microscopic characterization with numerical modeling provides better understanding in corrosion process and further elucidates the influence of pits on stress corrosion cracking. However, there is a scarcity of 3-D volumetric quantification and modeling 3-D pit to evaluate stress-strain distribution. The morphologic characteristics of pitting corrosion in 3-D should be given more consideration as the pit growth rate depends on potential distribution within the pit which is dominated by pit profile [20, 21].

This work aims at characterizing the morphological surface damage of pitting corrosion of aluminum alloy AA7075-T6, particularly in 3-D, and quantifying the corrosion effect of pitting on stress corrosion cracking. Confocal microscopy was utilized to characterize the morphology of pits with different times of immersion. Finite element analysis was carried out to evaluate the intensity of stress-strain concentration factor caused by the presence of pits. A method that simplified the complex and tortuous morphology of pits by idealized shapes was proposed in order to evaluate the equivalent effect of pit induced stresses which responsible for stress concentration and crack initiation.

4.2 Experimental methods

4.2.1 Materials and testing

Specimens of aluminum alloy AA7075-T6 sheet material with the thickness of $4.06mm$ were prepared for corrosion testing. The chemical composition of this alloy was shown in Table 3.1 in previous chapter. Pristine specimens were cut into rectangular pieces and mounted in phenolic hot mounting resin. The specimens were then ground with 400 grit SiC paper to remove all the sheared edges. Their surfaces were ground with subsequent use of 800 and 1200 grit SiC paper followed by fine grinding with 9-micron diamond suspension. The surfaces were finished by 3-micron diamond polishing and then oxide polishing (OP-S).

The microstructure of polished specimens was examined by optical microscope prior to immersion. Energy dispersive X-ray spectroscopy equipped in SEM was used to analyze the elemental composition of different intermetallic particles. Corrosion test was carried out according to ASTM standards G1-03 [22] and G46-94 [23]. These specimens were immersed in simulated seawater 3.5%wt NaCl solution in three different testing periods (24h, 120h, and 240h). The pH of this synthetic seawater solution was adjusted to 8.2 before the test. The corroded specimens were subsequently rinsed in running water for 5 minutes and desmutted with nitric acid 70% concentration for 1 minute after immersion period. A Branson 8510 Ultrasonic Cleaner was used to clean the samples again with the purpose of totally removing corrosion products. These samples were dried and stored in a desiccator until they were tested.

4.2.2 Pitting morphology and image analysis

The corroded samples were examined by a 3-D confocal profilometry Sensofar PLμ to acquire three-dimensional views of the pitting surfaces and data for pitting characterization. Confocal data generated from the Sensofar PLμ software are set of x, y, z coordinates of every point on the surfaces of corroded samples with the resolution of 0.375μm in x and y directions. The resolution in z coordinate, which represents the depth of corrosion pits, is 0.1μm. Simultaneously, these data were processed to characterize pitting morphology in 3-D and quantify the effects of pit induced stresses on aluminum alloys using three-dimensional models. The entire process is illustrated in Figure 4.1.

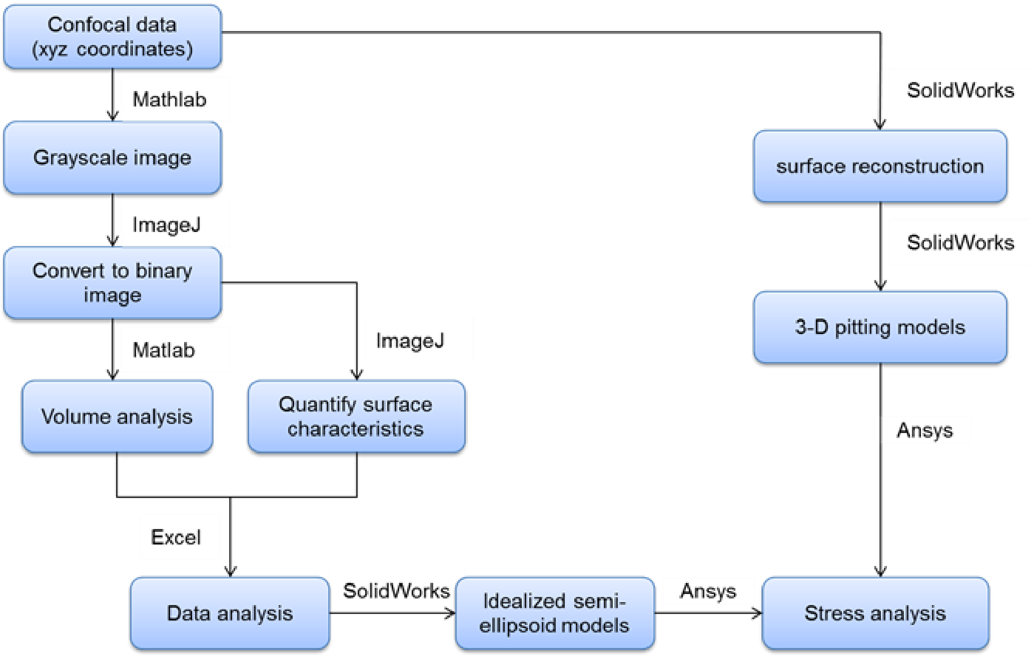

Figure 4.1 Procedure for 3-D pitting analysis

A public domain java-based image processing program ImageJ and commercial software Matlab are used consecutively in performing the area-volume analysis. Grayscale images with the resolution of 560x762 pixels are created from the data file of corroded sample using Matlab. The grayscale value of each pixel represents the depth z of each point on corroded sample as can be seen in Figure 4.2.

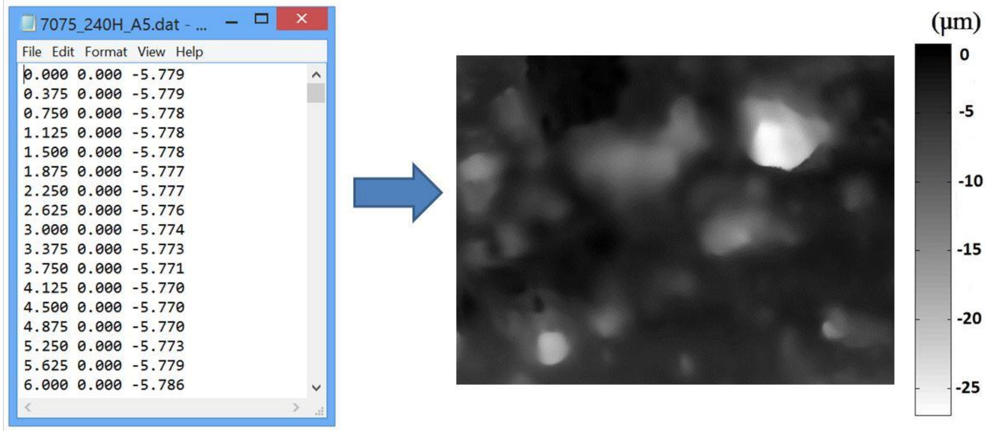

```
0.000 0.000 -5.779
0.375 0.000 -5.779
0.750 0.000 -5.778
1.125 0.000 -5.778
1.500 0.000 -5.778
1.875 0.000 -5.777
2.250 0.000 -5.777
2.625 0.000 -5.776
3.000 0.000 -5.774
3.375 0.000 -5.773
3.750 0.000 -5.771
4.125 0.000 -5.770
4.500 0.000 -5.770
4.875 0.000 -5.770
5.250 0.000 -5.773
5.625 0.000 -5.779
6.000 0.000 -5.786
```

Figure 4.2 Creating gray scale image from confocal data

These images were then converted into binary images by properly thresholding in ImageJ. Different methods such as Li’s Entropy, Minimum Cross Entropy available in ImageJ were used for comparison. The cross sections of several pits were plotted in ImageJ to find the optimum threshold for various pit areas. These thresholds were chosen carefully to avoid missing pit volume and pit area which can affect the characterization results. As shown in Figure 4.3, minimum cross entropy threshold was chosen for the pit in Figure 4.3(a) while Li's method was selected to determine the threshold for the pit in Figure 4.3(b). The basic criterion for defining optimum threshold is that it will subdivide the grayscale image of corrosion pits into meaningful non-overlapping regions of corroded areas (corrosion pits) and non-corroded areas, which could later provide a good approximation of stress-strain distribution. Noise or roughness on the pititng surface was removed by applying “Despeckle” option in ImageJ. The thresholded images were then analyzed to obtain the information of pitting surface such as area, centroid.

The pit volumes were calculated by sum up the z value of every point within the thresholded area of each pit. Surface morphology of corrosion pits, which is arbitrary in shape, were fitted by ellipses having identical area, centroid, and second order central moments [24]. This information was loaded into Excel for calculating volume, maximum depth, average depth and ellipsoid equivalent depth of individual pits in corresponding to the optimum threshold levels. Tortuous morphology of pits was simplified by equivalent semi-ellipsoids, which have the same surface area and either the same depth or same pit volume of actual shape, to evaluate the equivalent effect of pit induced stresses. These processes are illustrated in Figure 4.4.

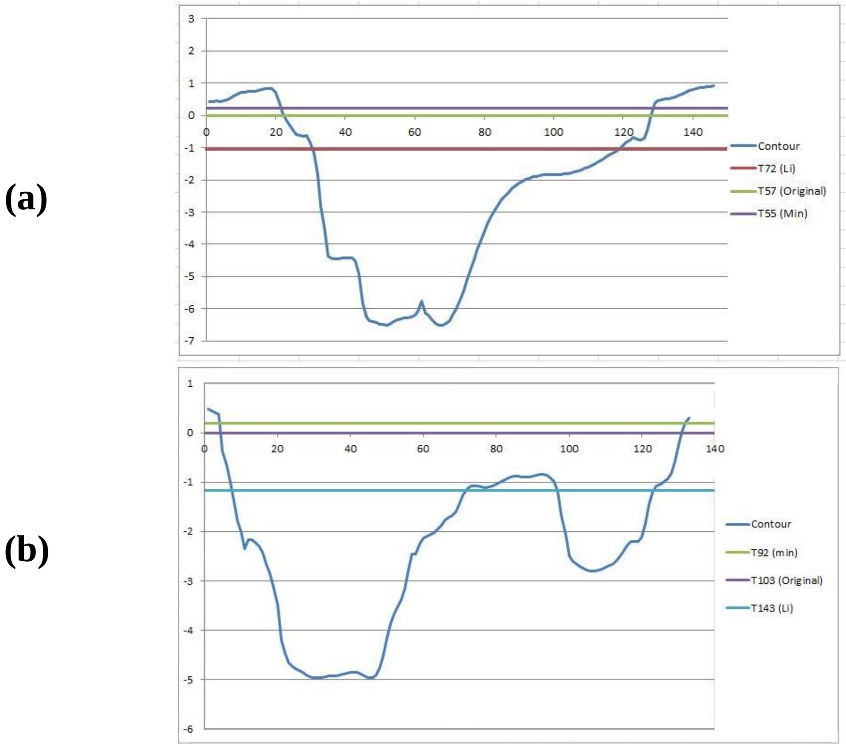

Figure 4.3 Determine optimum threshold value for grayscale image

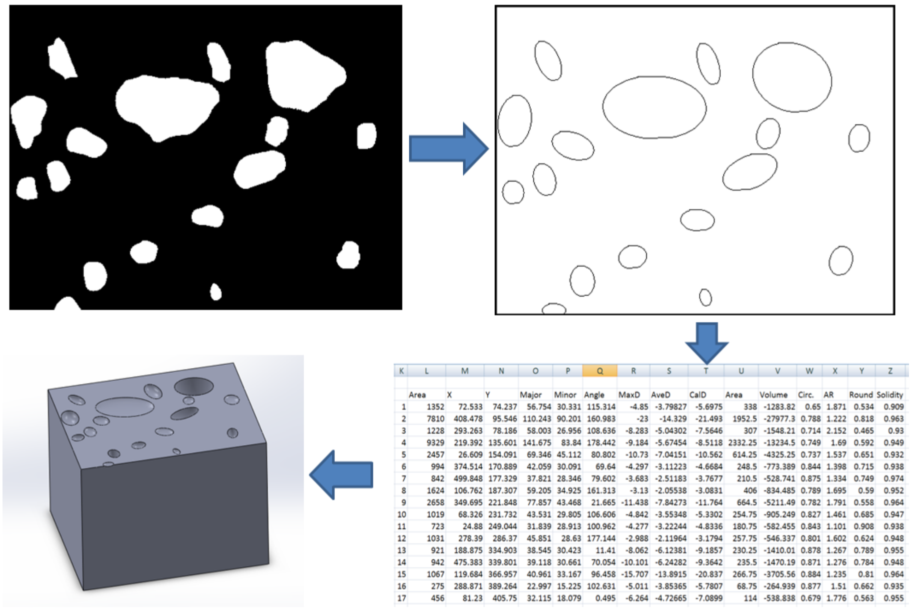

K	L	M	N	O	P	Q	R	S	T	U	V	W	X	Y	Z
	Area	X	Y	Major	Minor	Angle	MaxD	AveD	CalD	Area	Volume	Circ.	AR	Round	Solidity
1	1352	72.533	74.237	56.754	30.331	115.314	-4.85	-3.79827	-5.6975	338	-1283.82	0.65	1.871	0.534	0.909
2	7810	408.478	95.546	110.243	90.201	160.983	-23	-14.329	-21.493	1952.5	-27977.3	0.788	1.222	0.818	0.963
3	1228	293.263	78.186	58.003	26.956	108.636	-8.283	-5.04302	-7.5646	307	-1548.21	0.714	2.152	0.465	0.93
4	9329	219.392	135.601	141.675	83.84	178.442	-9.184	-5.67454	-8.5118	2332.25	-13234.5	0.749	1.69	0.592	0.949
5	2457	26.609	154.091	69.346	45.112	80.802	-10.73	-7.04151	-10.562	614.25	-4325.25	0.737	1.537	0.651	0.932
6	994	374.514	170.889	42.059	30.091	69.64	-4.297	-3.11223	-4.6684	248.5	-773.389	0.844	1.398	0.715	0.938
7	842	499.848	177.329	37.821	28.346	79.602	-3.683	-2.51183	-3.7677	210.5	-528.741	0.875	1.334	0.749	0.974
8	1624	106.762	187.307	59.205	34.925	161.313	-3.13	-2.05538	-3.0831	406	-834.485	0.789	1.695	0.59	0.952
9	2658	349.695	221.848	77.857	43.468	21.665	-11.438	-7.84273	-11.764	664.5	-5211.49	0.782	1.791	0.558	0.964
10	1019	68.326	231.732	43.531	29.805	106.606	-4.842	-3.55348	-5.3302	254.75	-905.249	0.827	1.461	0.685	0.947
11	723	24.88	249.044	31.839	28.913	100.962	-4.277	-3.22244	-4.8336	180.75	-582.455	0.843	1.101	0.908	0.938
12	1031	278.39	286.37	45.851	28.63	177.144	-2.988	-2.11964	-3.1794	257.75	-546.337	0.801	1.602	0.624	0.948
13	921	188.875	334.903	38.545	30.423	11.41	-8.062	-6.12381	-9.1857	230.25	-1410.01	0.878	1.267	0.789	0.955
14	942	475.383	339.801	39.118	30.661	70.054	-10.101	-6.24282	-9.3642	235.5	-1470.19	0.871	1.276	0.784	0.948
15	1067	119.684	366.957	40.961	33.167	96.458	-15.707	-13.8915	-20.837	266.75	-3705.56	0.884	1.235	0.81	0.964
16	275	288.871	389.264	22.997	15.225	102.631	-5.011	-3.85365	-5.7807	68.75	-264.939	0.877	1.51	0.662	0.935
17	456	81.23	405.75	32.115	18.079	0.495	-6.264	-4.72665	-7.0899	114	-538.838	0.679	1.776	0.563	0.955

Figure 4.4 Illustration of processes for idealizing pits by equivalent semi-ellipsoids

4.2.3 Finite element analysis

In order to quantify the effect of pit morphology and orientation on stress concentration, 3-D stress-strain distribution of corroded samples was analyzed using finite element analysis software Ansys. Three-dimensional pitting surface of corroded sample was reconstructed from the data file of confocal profilometer. This process was done by using a reverse engineering plugin of SolidWorks, ScanTo3D, which allows us to import point cloud data to create meshes and surfaces. The body of the corroded sample was then created by the Extrude command. Fig. 4.5 illustrates the procedure to reconstruct corroded surface for stress-strain analysis and quantifying corrosion damage from confocal data.

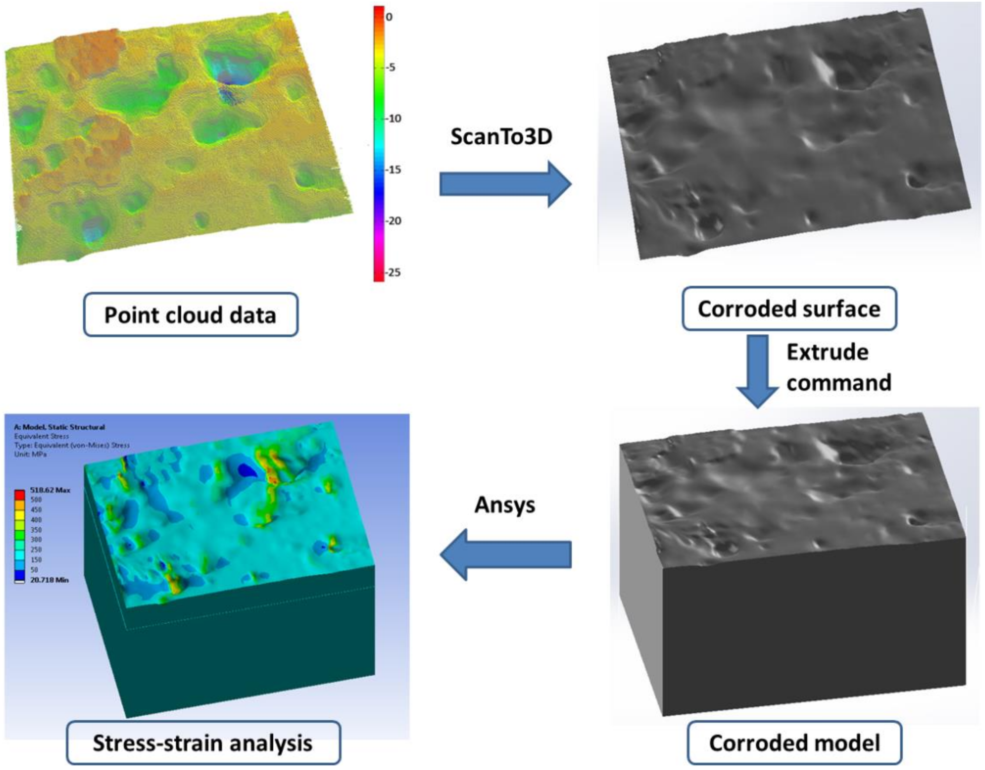

Figure 4.5 Schematic diagram illustrating the processes to reconstruct corroded surface for stress-strain analysis

Finite element meshes were generated using quadrilateral elements for the body and tetrahedral elements on the pitting surface. Curvature method was used for advanced mesh sizing such that meshes around pits were refined. There are about 150000 elements for one model. Convergence test was performed to ensure that the deviation in the stress concentration of a pit is less than 5%. The mesh and boundary conditions of finite element model are shown in Fig. 4.6. A uniform stress of 201.2MPa, which is 40% of material yield strength, is applied on one side of the model in the x-direction. The other side is constrained in the x-direction. A zero displacement along the y-direction is applied for the bottom edge of the constrained side, and the end point of that bottom edge is fixed in the z-direction. Elastic-perfectly plastic material was assumed with Young's modulus $E = 71.7GPa$ and Poisson's ratio of *0.33*

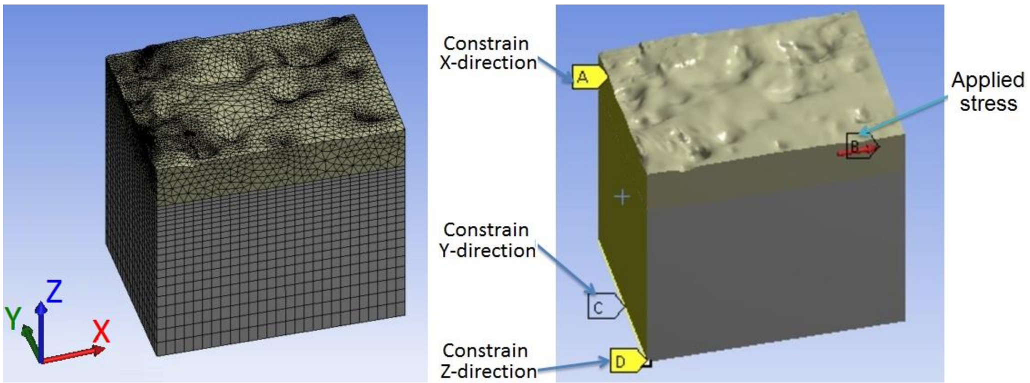

Figure 4.6 Mesh and boundary conditions of finite element models

4.3 Microstructural characteristics of AA7075-T6

Figure 4.7 shows the composite image of the grain structure of AA7075-T6 along three principle directions, namely longitudinal (L), transverse (T) and short transverse (S) directions. As a consequence of rolling processes, this alloy has a pancake shaped grain structure with the average size of $185.4 \times 128.5 \times 37.2\mu m^3$ $(L \times T \times S)$

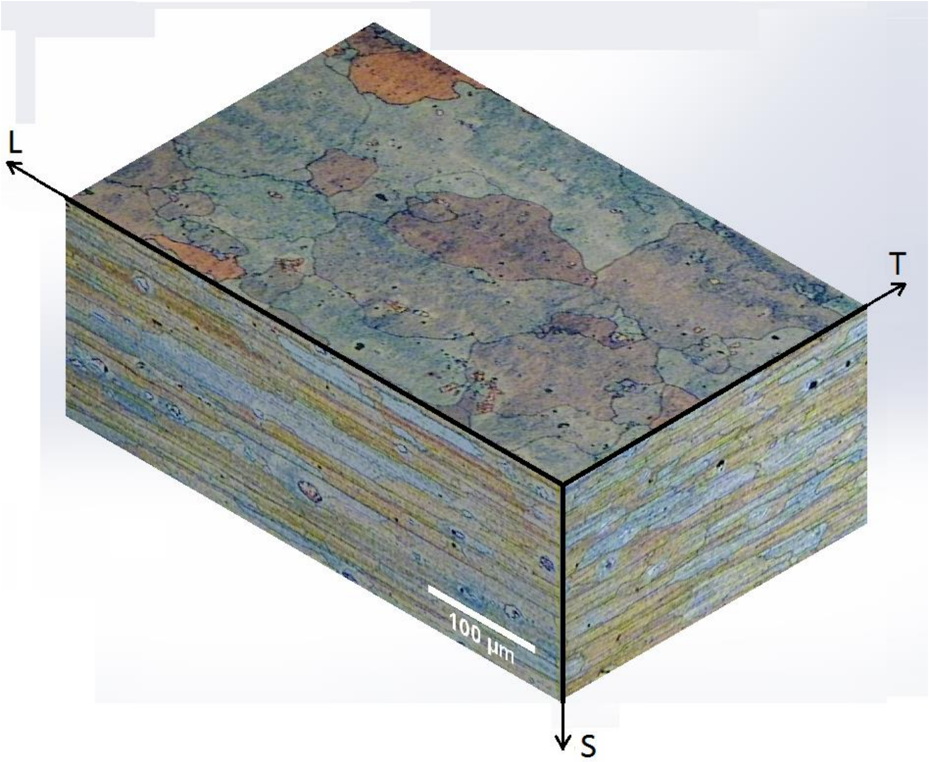

Figure 4.7 Grain structure of AA7075-T6

Corrosion occurs when there are dissimilar metals or metal alloys, which are different in chemical compositions and corrosion potential, exposed to a corrosive environment. Corrosion is a great concern for aluminum and its alloys as aluminum is very active compared to other metals. Therefore, the elemental composition of constituent particles plays an important role in corrosion performance of aluminum alloys because of chemical dissimilarity. Figure 4.8 shows EDS analysis of intermetallic particles of AA7075-T6 and their corresponding spectra. The results indicate that this alloy contains a large amount of zinc, which is uniformly distributed over the entire aluminum matrix. The addition of zinc promotes the formation of $MgZn_2$ (η phase) precipitates which significantly enhances mechanical strength of aluminum alloys. However, $MgZn_2$ is also reported to be responsible for stress corrosion cracking [25] in 7xxx series aluminum alloys. The size of this precipitate is just in the range of sub-micrometer. Al(Cu,Fe) particles, most likely to be Al_7Cu_2Fe according to [26], are typically irregular in shape with their size could be up to 30 μm^2. They are numerous in certain areas and have a bright tone in SEM image. Al(Mg_2Si) particles are smaller in size and less frequently observed than Al(Cu,Fe) particles. Al(Mg_2Si) particles have round shape and appear to be dark in SEM image.

As reported by previous researchers [27, 28] who also studied corrosion of AA7075 in NaCl medium, Mg_2Si (-1.54V_{SCE}) is the most anodic particle found in AA7075 and the second one is η phase (-1.03V_{SCE}). On the other hand, Al_7Cu_2Fe (-0.55V_{SCE}) acts as cathodic particles in comparison with the overall potential of aluminum matrix (around -0.8V_{SCE}). Based on potential differences between constituent particles, cathodic particles Al_7Cu_2Fe having adjacent anodic Mg_2Si particles are the most favorable nucleation sites for peripheral pitting. Potential difference between Al_7Cu_2Fe and Mg_2Si is the greatest (~1V_{SCE}) among other couplings such as η-Al_7Cu_2Fe (~0.5V_{SCE}) or η-matrix (~0.2V_{SCE}). However, η phase is distributed in aluminum matrix with higher density than Mg_2Si particles. Therefore, most of peripheral pits would initiate at cathodic particles (Al_7Cu_2Fe) surrounded by aluminum matrix having high density of η phase. Figure 4.9 shows an optical image of a corroded sample after it was cleaned and shortly polished with colloidal silica 0.04µm. It can be seen that several peripheral pits occurred with a trace of Al_7Cu_2Fe particles at the bottom. This observation is a direct support for the hypothesis that pitting in AA7075 favorably initiates at Al_7Cu_2Fe particles, which have the most cathodic potential among constituent particles of AA7075.

Another favorable nucleation site for pitting is grain boundaries with high concentration of η phase. Park et. al [29] reported that there is a significant enrichment of copper at grain boundaries having high concentration of η phase. The present of copper could deplete such grain boundaries or reduce the corrosive resistance of the alloy by forming copper clusters:

$$3Cu^{2+} + 2Al = 2Al^{3+} + 3Cu(cluster) \tag{4.1}$$

As η phase is distributed over the entire aluminum matrix with superior number density than Mg_2Si particles. Its contribution to the overall pitting processes of AA7075 is much more significant than Mg_2Si particles even although Mg_2Si is the most anodic constituent found in AA7075.

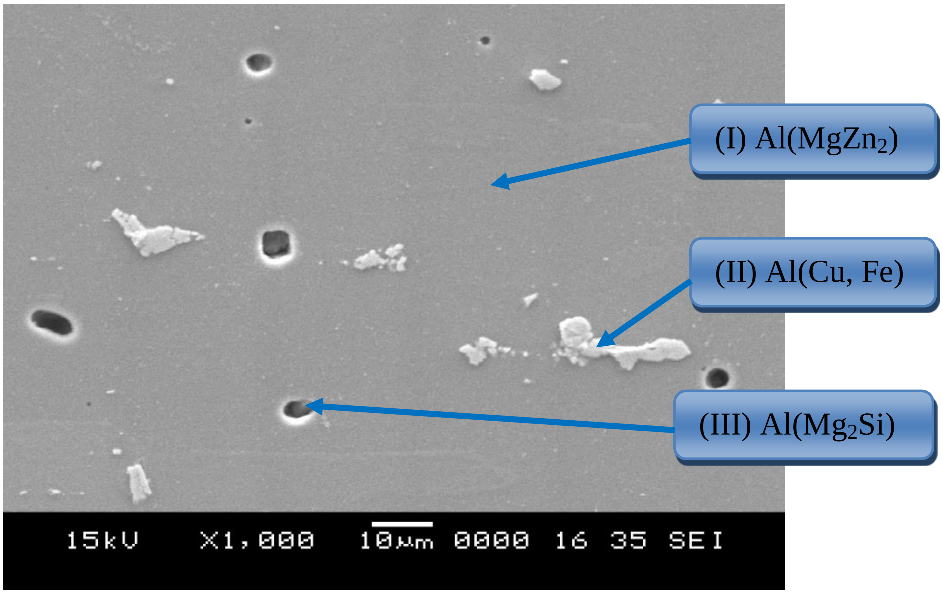

(I)

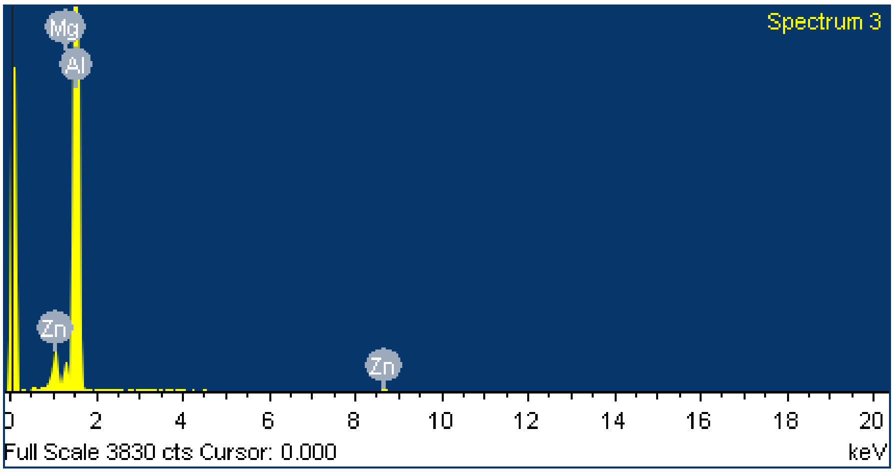

(II)

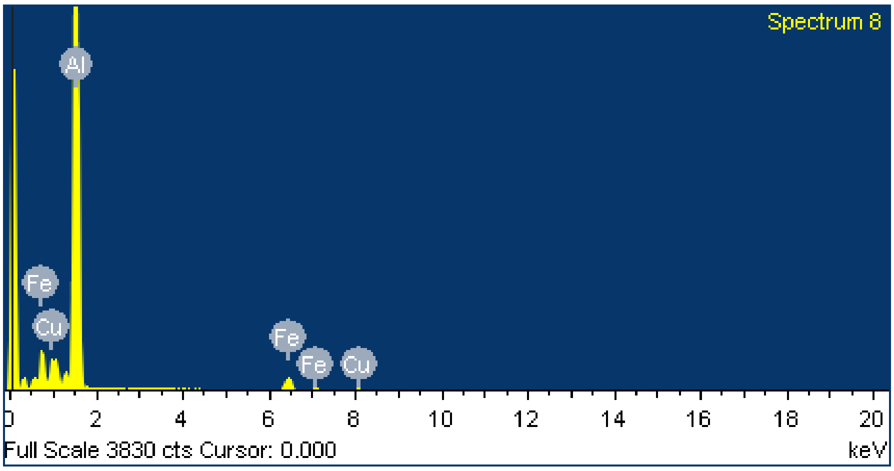

(III)

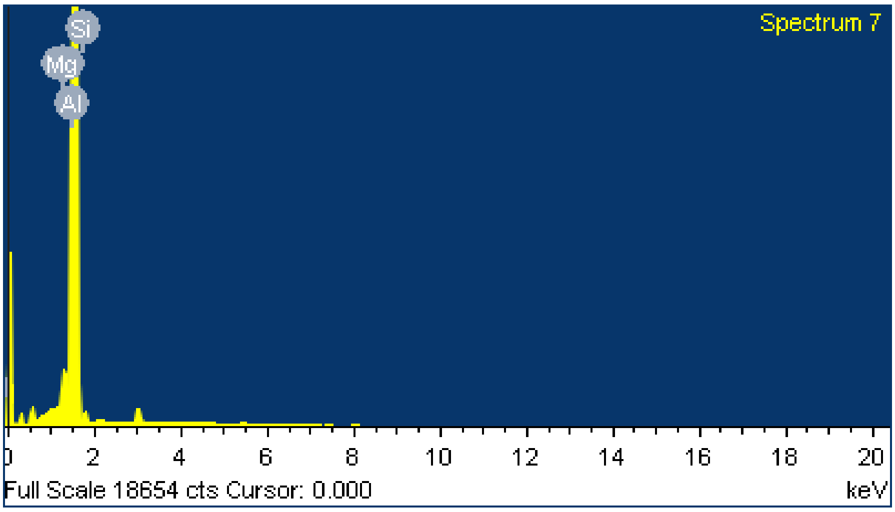

Figure 4.8 SEM image of intermetallic particles in AA7075-T6 sample and their corresponding spectra (I) Al($MgZn_2$), (II) Al(Cu,Fe) and (III) Al(Mg_2Si)

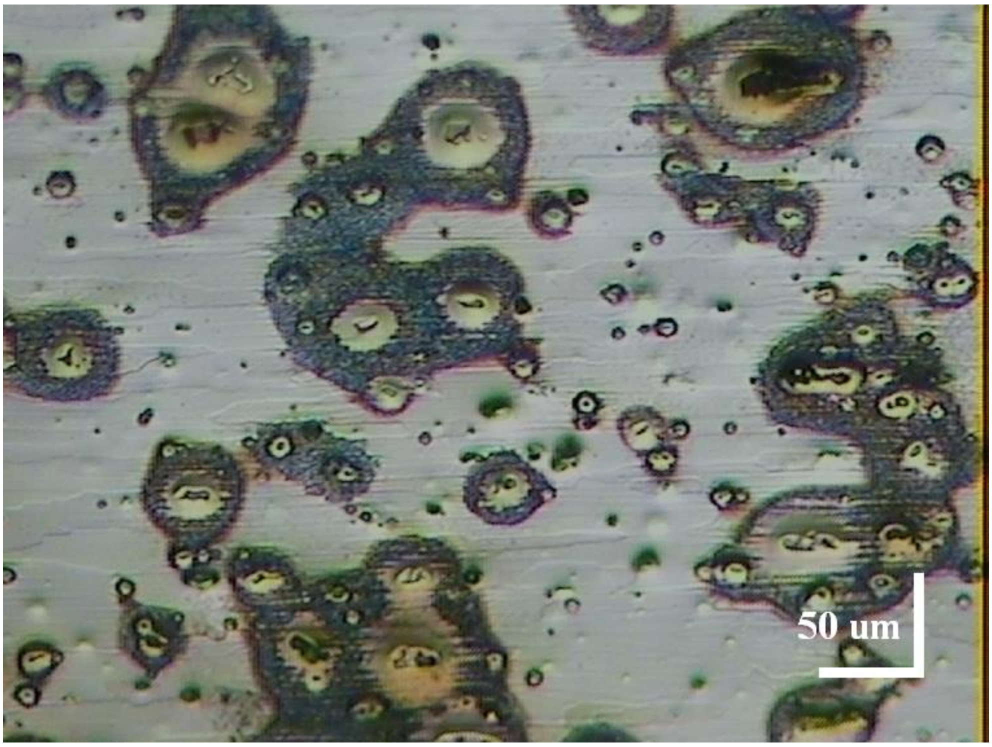

Figure 4.9 Optical image of a corroded sample after it was cleaned and shortly polished with colloidal silica 0.04µm

4.4 Pitting damage and morphology

Typical corroded surfaces with different immersion times obtained by confocal image profiler were visualized in ImageJ (Figure 4.10). The scale bar indicates the depth of corrosion pits in µm. As corrosion time increases, it can be seen that pit grows with various shapes and has a tendency to coalesce with surrounding ones to form a larger pit. Several tiny new pits continue to form and develop on the 240h corroded sample. The information of corrosion severity was calculated and summarized in Table 4.1. The results show that corrosion pits developed significantly in both affected area and depth. The increase of standard deviation in this table indicates that the variation of pit size becomes more and more significant with extended corrosion time. With the purpose of estimating corrosion resistance, corrosion mass loss per unit area after three corrosion periods was calculated by quantifying the total pit volume. According to Figure 4.11, the relative mass loss after 24h of immersion is trivial, about 0.015g/m^2. However, the corrosion resistance of this aluminum alloy reduces substantially with increasing corrosion time, whereas the mass loss after 240h is about 5.5 times of that obtained after 120h (2.085g/m^2 compared to 0.388g/m^2).

Table 4.1 Statistical dimensions of corrosion pits with different immersion times

	Corrosion times (h)					
	24		120		240	
Corrosion parameters	Mean	Standard deviation	Mean	Standard deviation	Mean	Standard deviation
Pitting area (%)	0.971	0.489	4.262	2.955	22.137	8.584
Surface size (µm^2)	21.011	16.102	137.037	117.122	321.321	314.439
Pit depth (µm)	1.303	0.503	5.385	3.507	7.384	3.412
Pit Volume (µm^3)	33.981	40.381	957.029	968.520	3010.888	4669.145

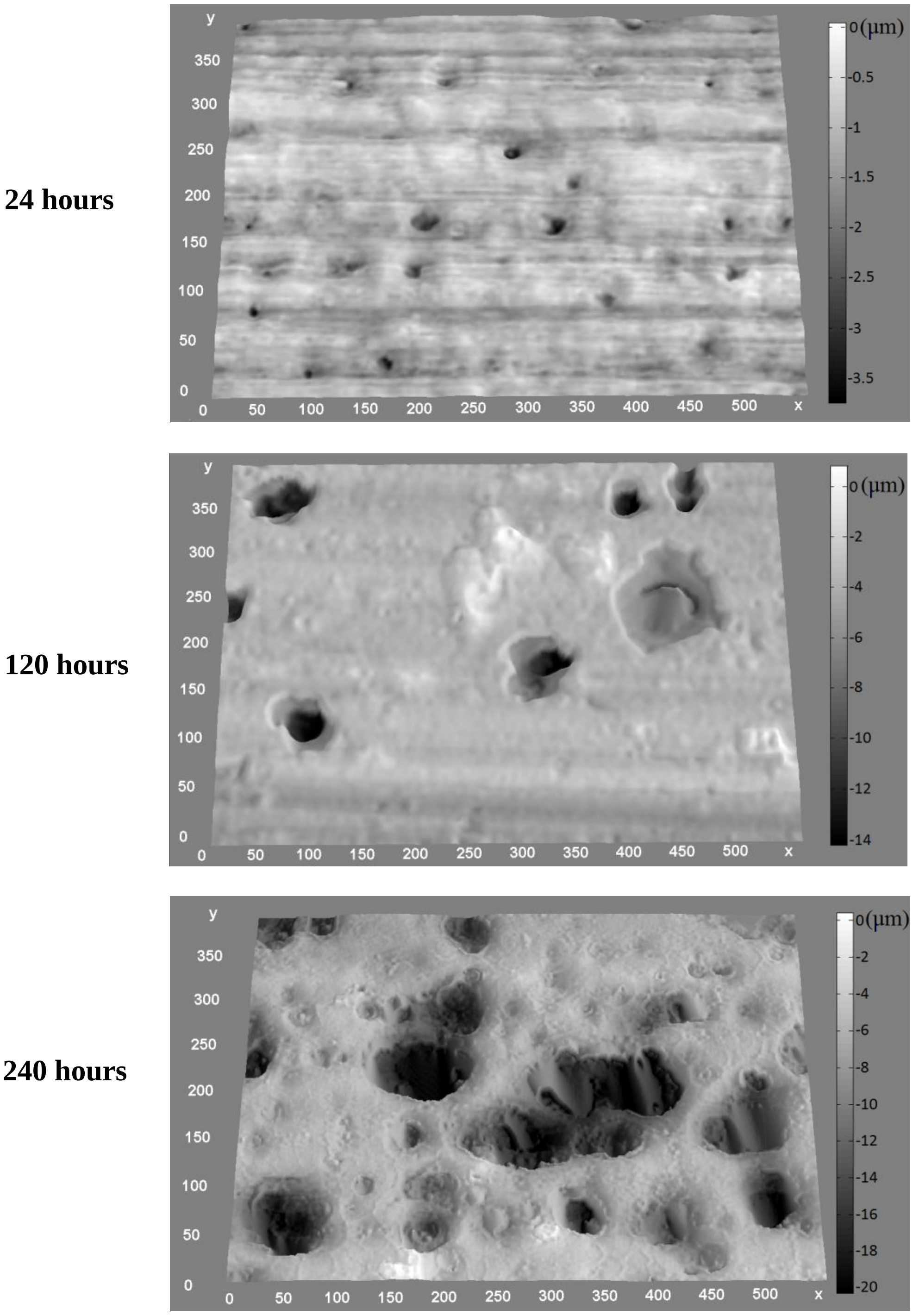

Figure 4.10 Images of corrosion pits after 24, 120 and 240 hours of immersion

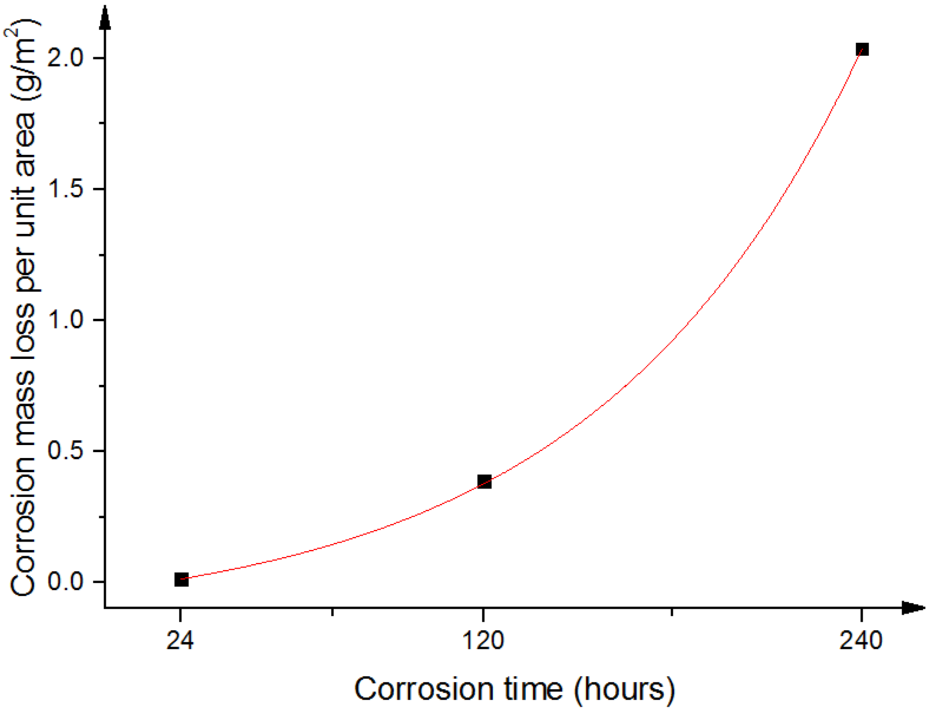

Figure 4.11 Corrosion mass loss per unit area after three immersion periods

Pit shapes are traditionally described by the Area-Box (AB) parameter, which is defined as the ratio between pit area and the smallest rectangular area surrounding pit at a random cross section. In this study, we propose a method to classify pitting morphology using three-dimensional volumetric information obtained from confocal microscope.

As surface morphology of pits can be fitted by equivalent ellipses, the volume of a single pit can be calculated as:

$$V = \pi ab\bar{h} \tag{4.2}$$

where,

a and b are semi-major and semi-minor of equivalent ellipse of pit on surface

$\bar{h}$ is the average depth of a single pit

The theoretical volumes of cylindrical, semi-ellipsoidal and conical shapes are known to be: πabh_{max}, $\frac{2}{3}\pi abh_{max}$ and $\frac{1}{3}\pi abh_{max}$,respectively, with h_{max} is the maximum depth. Therefore, we can classify various pit shapes by using a

3-D shape parameter defined by the ratio of average depth and maximum depth $(\bar{h}/h_{max})$ within a single pit.

- Pits are described as having conical shape if $(\bar{h}/h_{max})$ is around *1/3* (ranging from *1/4* to *5/12*), due to the expected volumetric ratio for conical shape.
- Pits are considered as having semi-ellipsoidal shape if $(\bar{h}/h_{max})$ is around *2/3* (ranging from *7/12* to *3/4*), due to theoretical volume of semi-ellipsoid.
- Pits are represented by cylindrical shape if $(\bar{h}/h_{max})$ is close to *1* due to the expected value of this ratio for cylinder.
- Pits are considered as having irregular shape if $\bar{h}/h_{max}$ is smaller than *1/4*. The transitional regions A and B are defined by $(5/12 < \bar{h}/h_{max} < 7/12)$ and $(3/4 < \bar{h}/h_{max} < 11/12)$, respectively.

Pit morphology was classified using 3-D shape parameter and plotted versus the ratio of equivalent diameter of pit on the surface and pit depth (Figure 4.12). The equivalent diameter of pit on the surface is calculated by the following equation:

$$Pit\ diameter = \sqrt{\frac{4\times Area}{\pi}} \tag{4.3}$$

From Figure 4.12, it can be seen that pits are generally wider on the surface than in depth. The average ratio of pit diameter versus pit depth is about 3.5, and there is no significant change of this ratio with different immersion periods. This result implies that pits developed faster on the surface than in depth; in other words, corrosion rate at pit mouth is noticeably higher than at the bottom. Due to the stochastic nature of pitting corrosion, the morphology of corrosion pits was statistically classified as shown in Table 4.2. This table reveals that pits present with high quantity in semi-ellipsoidal and A transitional region. There are just a small numbers of pits in conical and B transitional region. Irregular and cylindrical pits were not found in this aluminum alloys. The morphological distribution of pits found in this study is in contrary with previous work [4, 5] using AB parameter where pits were reported to be predominantly conical and irregular shape. The non-consensus here could be explained by the difference of alloying elements presented in aluminum or the limitation of 2-D classification of pit morphology. It should be noted here that randomly getting vertical cross sections of pits may not be accurate as one pit could have various shapes at different cross sections. According to the morphological characteristics of pitting corrosion found in this section, a method that simplified tortuous morphology of pits by idealized geometry was proposed in section 4.6 of this chapter.

Table 4.2 Pit morphology classification and distribution

Corrosion times	Irregular pits (%)	Conical pits (%)	Transitional region A(%)	Semi-ellipsoidal pits (%)	Transitional region B(%)	Cylindrical pits (%)
24h	0	13.80	37.93	31.03	17.24	0
120h	0	3.70	40.74	37.04	18.52	0
240h	0	0	52.63	31.58	15.79	0
Average	0	6.67	42.67	33.33	17.33	0

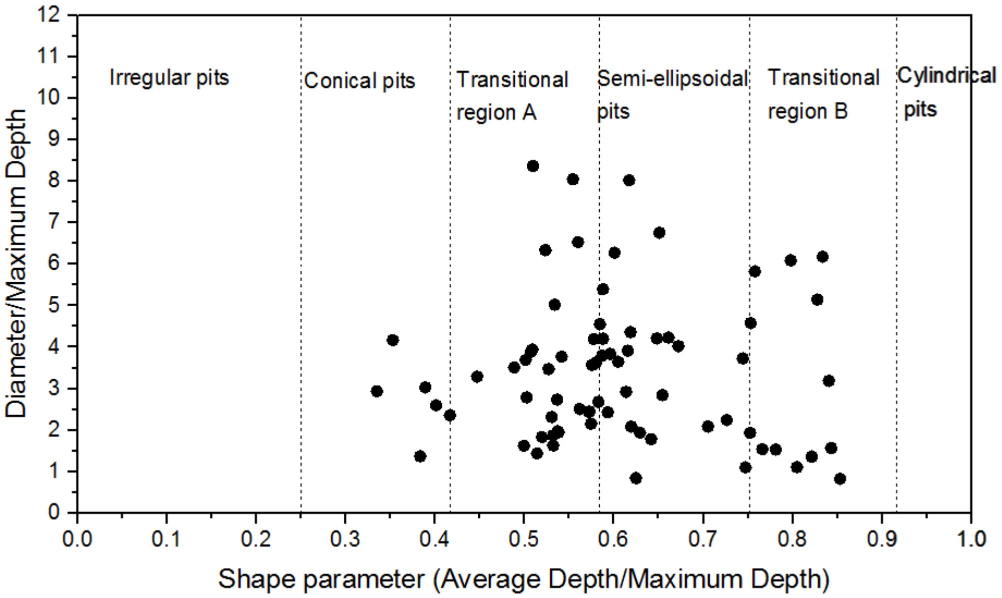

Figure 4.12 Pit geometry classification and distribution

4.5 Quantification of stress-strain concentration factor

Pits on corroded surface, which produce geometrical discontinuities, function as stress concentrators that produce a significant increase in the intensity of stress field and enhance localized damage causing crack initiation. Finite element analysis of the stress-strain distribution was carried out on 3-D pitting surface extracted from confocal image data to quantify the effect of pitting corrosion. It is well known that crack initiation is highly influenced by plasticity effects at stress concentration sites. Turnbull et al. [10] demonstrated that there is a redistribution of stress due to the localization of plastic strain at corrosion pits. In addition, the maximum stress cannot be implicitly associated with maximum strain as in the case of elastic deformation when yielding occurs. Therefore, a quantitative stress-strain parameter which considers the effect of both local stress concentration factor (k_σ) and strain concentration factor (k_ε) is employed in this study to analyze the effect of pitting corrosion on stress-strain distribution. This parameter was proposed by Gao et al. [30] as:

$$k_g = \sqrt{k_\sigma k_\varepsilon} \tag{4.4}$$

where, $k_\sigma = \sigma_{max}/\sigma_\infty$; $k_\varepsilon = \varepsilon_{max}/\varepsilon_\infty$

in which, σ_{max} and ε_{max} are the concentrated stress and strain normalized by the far field stress (σ_∞) and strain (ε_∞) respectively.

With the applied load of 40% yield strength, there is only mild stress concentration on pitting surface after 24h with maximum stress concentration was found to be 1.9 and the materials was still in elastic deformation region (Figure 4.13). From equation (4.4), we can deduce that $k_g = k_\sigma = k_\varepsilon$ when materials exhibit elastic behavior. However, these parameters will be distinct from each other when plastic deformation occurs. It was observed that during plastic deformation, k_ε is dominant while k_σ remains constant as local stress concentration just slightly increase after it reaches its yield strength. Previous researchers [31, 32] have shown that k_g is a suitable parameter for characterizing the evolution of fatigue cracks in short crack growth region.

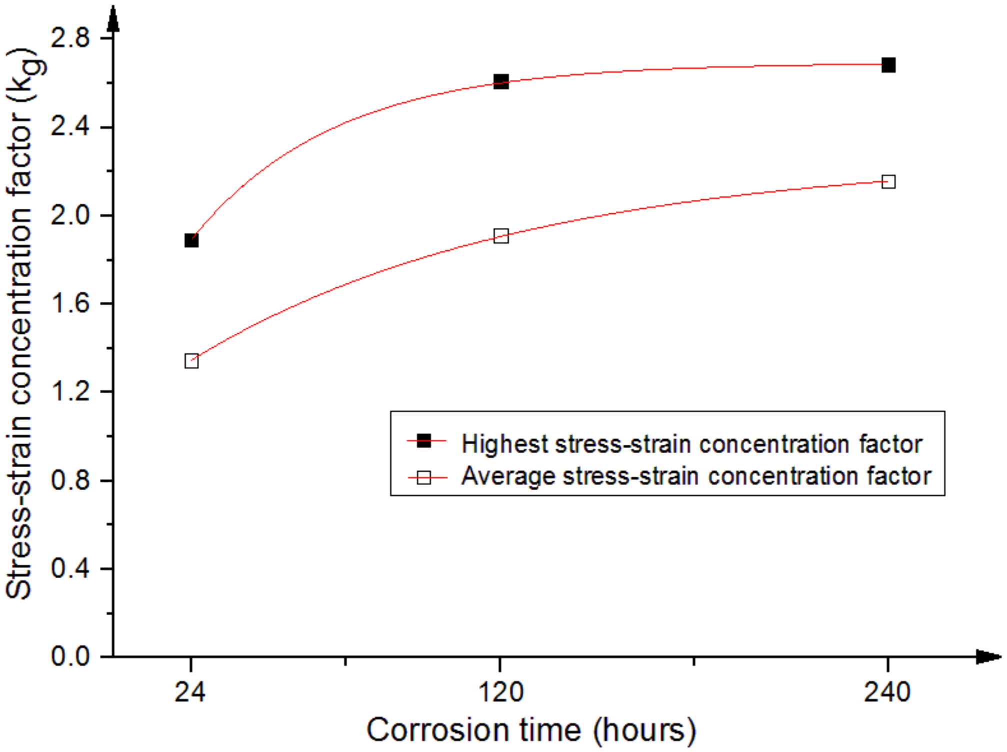

Figure 4.13 Stress-strain concentration factor calculated from finite element analysis

As can be seen from Figure 4.14, the severity of corrosion increased significantly with time in term of both affected area and depth, which in turn intensified the stress-strain concentration factor. When corrosion time increased from 24h to 120h, stress-strain concentration factor (k_g) rose by almost 30%. Although average k_g kept increasing with corrosion time, the highest k_g was about to reach a saturated point and did not significantly grow after 120h of immersion ($k_\sigma = \sim 2.6$ and $k_\varepsilon \sim 2.7$). Within a pit, highest stress-strain concentration occurred at both sides of pit mouth, which are 90^0 relative to loading direction. It should be noted that the highest k_g values found at different corrosion periods do not necessarily occur at the largest or deepest pits as they are also influenced by other factors such as pit orientation, defined by the angle between the major axis and the loading direction, pit shape ratio and the interaction with adjacent pits. However, pit depth is still a major factor that affects the stress-strain concentration factor.

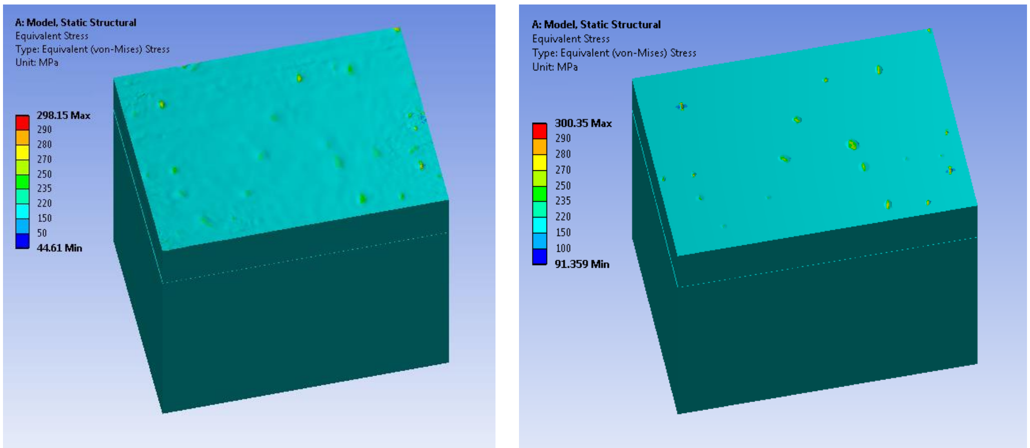

24 hours

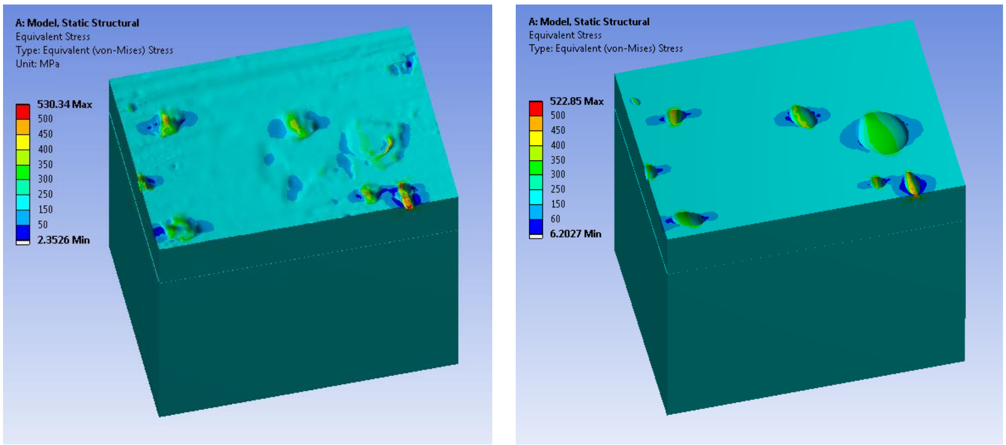

120 hours

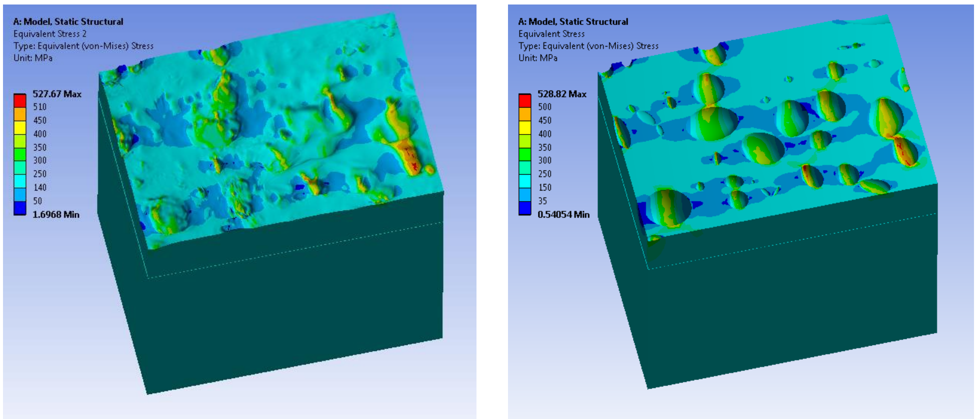

240 hours

Figure 4.14 Comparison of von-Mises stress distribution on corroded models and idealized models (having the same highest depth within a pit) with different corrosion periods

4.6 Simplification of 3-D pitting corrosion

Due to the tortuous morphology of pits, the mesh density surrounding pits needs to be critically refined in order to meet the requirement for convergence. The processes to construct a mesh from 3-D confocal data are labor intensive and not adaptable for automation. Furthermore, it is almost impossible to simulate the crack initiation and propagation processes due to the limitation of disk space and running time consideration. Therefore, a methodology was developed to simplify 3-D complex shapes of pits into idealized geometries for further understanding the initiation and propagation mechanism of cracks from pitting corrosion.

The pitting morphology analysis in section 4.4 has demonstrated that pits are predominantly semi-ellipsoidal. In this study, the tortuous morphology of pits was approximated by equivalent semi-ellipsoids, which have the same surface area and either pit volume (by adjusting the depth of semi-ellipsoid) or pit depth (using the highest depth within a pit while pit volume can be different) of actual shape. As shown in Figure 4.14, using semi-ellipsoids to idealize tortuous morphology of pits provides a good approximation in evaluating the equivalent effect of pits induced stresses. For better comparison, a same scale of the stress-strain range is applied such that the actual and idealized pit will have an identical color scale. It was found that using highest depth within a pit to idealize pit shape provides a better prediction of stress-strain distribution compared to the calculated depth, which is determined by pit volume. The average change in k_g using highest pit depth is less than 8% although there is a substantial variation in pit volume (about 30%). This result indicates that pit depth is a dominant parameter that affects stress-strain concentration factor. Note that stress-strain concentration factor is also affected by pit orientation, shape ratio and interaction with surrounding pits. Although there are some numerical studies which systematically investigate the effect of orientation and shape ratio on stress concentration of single idealized pit, i.e. using semi-ellipsoidal or hemispherical model [7, 19], none of them are able to capture the intrinsic complexity of local stress-strain distribution around a 3-D pit. The methodology proposed in this study incorporates the combined effect of pit morphology and orientation as well as its interaction with other pits in adjacent areas. Therefore, it provides a more realistic approximation in quantifying stress-strain concentration factor (k_g), which was demonstrated to be responsible for the initiation and non-isotropic development of fatigue crack.

4.7 Conclusions

EDS analysis was carried out to identify different intermetallic particles and their role in corrosion behavior of AA7075-T6. 3-D morphological characteristics of pitting corrosion and their effects on stress-strain concentration were investigated. Confocal microscopy has been proved to be a great assistance in quantifying corrosion damage and characterizing pitting morphology in 3-D. An analysis procedure was developed to quantify the severity of corrosion and classify pit morphology using a 3-D shape descriptor defined by the ratio of average depth and maximum depth within a single pit.

EDS analysis revealed that $MgZn_2$ (η phase) is distributed over the entire aluminum matrix of AA7075-T6 with superior number density than other intermetallic particles. Its contribution to the overall pitting processes of AA7075 is much more significant than Mg_2Si particles even although Mg_2Si is the most anodic constituent found in AA7075.

Corrosion severity increased with time in term of both affected area as well as pit depth. Pit width is generally larger than pit depth, which indicates that corrosion rate is higher at pit mouth than at the bottom. Pits are predominantly semi-ellipsoidal and in the transitional region between conical and semi-ellipsoidal shape. Irregular and cylindrical pits were not found in this aluminum alloy.

Stress-strain concentration factor significantly increased with corrosion duration. Highest stress-strain concentration reached a saturated point after 120h of immersion. Further increase of corrosion time to 240h does not significantly enhance highest stress-strain concentration. Within a single pit, highest stress-strain concentration occurred at both sides of pit mouth, which are 90^0 relative to loading direction.

A methodology was proposed to simplify tortuous morphology of corrosion pits into idealized geometry. It was found that idealizing pits by semi-ellipsoids with equivalent surface area and equal maximum pit depth provides a good prediction in evaluating stress-strain concentration factor and analyzing stress-strain distribution on pitting surface. The proposed method in this study provides a realistic approximation in quantifying stress-strain concentration factor, which can be used for the simulation of crack initiation and propagation processes to predict possible crack nucleation sites as well as the early stage of crack propagation behavior.

References

1. Itzhak, D., I. Dinstein, and T. Zilberberg, *Pitting corrosion evaluation by computer image processing.* Corrosion Science, 1981. **21**(1): p. 17-22.
2. North Atlantic Treaty Organization, R. and O. Technology, *Corrosion fatigue and environmentally assisted cracking in aging military vehicles La fatigue-corrosion et la fissuration en milieu ambiant des véhicules militaires vieillissants*. 2011, [Neuilly-sur-Seine Cedex]: N.A.T.O., Research and Technology Organization.
3. Codaro, E.N., et al., *An image processing method for morphology characterization and pitting corrosion evaluation.* Materials Science and Engineering: A, 2002. **334**(1–2): p. 298-306.
4. Silva, J.W.J., et al., *Morphological analysis of pits formed on Al 2024-T3 in chloride aqueous solution.* Applied Surface Science, 2004. **236**(1–4): p. 356-365.
5. Silva, J.W.J., et al., *Influence of chromate, molybdate and tungstate on pit formation in chloride medium.* Applied Surface Science, 2005. **252**(4): p. 1117-1122.

6. Lv, S.-l., et al., *Influence of morphology of corrosion on fracture initiation in an aluminum alloy.* Materials & Design, 2013. **45**(0): p. 96-102.
7. Cerit, M., K. Genel, and S. Eksi, *Numerical investigation on stress concentration of corrosion pit.* Engineering Failure Analysis, 2009. **16**(7): p. 2467-2472.
8. Cerit, M., *Numerical investigation on torsional stress concentration factor at the semi elliptical corrosion pit.* Corrosion Science, 2013. **67**(0): p. 225-232.
9. Turnbull, A., D.A. Horner, and B.J. Connolly, *Challenges in modelling the evolution of stress corrosion cracks from pits.* Engineering Fracture Mechanics, 2009. **76**(5): p. 633-640.
10. Turnbull, A., L. Wright, and L. Crocker, *New insight into the pit-to-crack transition from finite element analysis of the stress and strain distribution around a corrosion pit.* Corrosion Science, 2010. **52**(4): p. 1492-1498.
11. Pidaparti, R.K., Kittisak; Rao, Appajoysula, *Corrosion Pit Induced Stresses Prediction from SEM and Finite Element Analysis.* International Journal for Computational Methods in Engineering Science and Mechanics, vol. 10, issue 2, pp. 117-123.
12. Pidaparti, R.M. and A.S. Rao, *Analysis of Pits induced stresses due to metal corrosion.* Corrosion Science, 2008. **50**(7): p. 1932-1938.
13. Pidaparti, R.M. and R.R. Patel, *Correlation between corrosion pits and stresses in Al alloys.* Materials Letters, 2008. **62**(30): p. 4497-4499.
14. Pidaparti, R.M., et al., *Classification of corrosion defects in NiAl bronze through image analysis.* Corrosion Science, 2010. **52**(11): p. 3661-3666.
15. Pidaparti, R.M. and R.K. Patel, *Investigation of a single pit/defect evolution during the corrosion process.* Corrosion Science, 2010. **52**(9): p. 3150-3153.

16. Pidaparti, R. and R. Patel, *Modeling the Evolution of Stresses Induced by Corrosion Damage in Metals.* Journal of Materials Engineering and Performance, 2011. **20**(7): p. 1114-1120.
17. P. Russell, D.B., J. Thornton, *SEM and AFM: Complementary Techniques for High Resolution Surface Investigations.*
18. G. O. Ilevbare, O.S., R. G. Kelly, and J. R. Scully, *In Situ Confocal Laser Scanning Microscopy of AA 2024-T3 Corrosion Metrology: I. Localized Corrosion of Particles. J. Electrochem. Soc. 2004 151(8): B453-B464;.*
19. Huang, Y., et al., *Quantitative correlation between geometric parameters and stress concentration of corrosion pits.* Engineering Failure Analysis, 2014. **44**(0): p. 168-178.
20. Pickering, H.W., *The role of electrode potential distribution in corrosion processes.* Materials Science and Engineering: A, 1995. **198**(1–2): p. 213-223.
21. Engelhardt, G., M. Urquidi-Macdonald, and D.D. Macdonald, *A simplified method for estimating corrosion cavity growth rates.* Corrosion Science, 1997. **39**(3): p. 419-441.
22. ASTM G1-03(2011), *Standard Practice for Preparing, Cleaning, and Evaluating Corrosion Test Specimens*, ASTM International, West Conshohocken, PA, 2011, www.astm.org.
23. ASTM G46-94(2013), *Standard Guide for Examination and Evaluation of Pitting Corrosion*, ASTM International, West Conshohocken, PA, 2013, www.astm.org.
24. Scheffe, H., *Review: H. Cramer, Mathematical methods of statistics.* 1947: p. 733-735.
25. Carroll, M., et al., *Effects of Zn additions on the grain boundary precipitation and corrosion of Al-5083.* Scripta Materialia, 2000. **42**(4): p. 335-340.

26. Birbilis, N., et al., *Understanding damage accumulation upon AA7075-T651 used in airframes from a microstructural point of view.* MATERIALS SCIENCE AND TECHNOLOGY-ASSOCIATION FOR IRON AND STEEL TECHNOLOGY-, 2005. **1**: p. 1.
27. Birbilis, N. and R. Buchheit, *Investigation and discussion of characteristics for intermetallic phases common to aluminum alloys as a function of solution pH.* Journal of The Electrochemical Society, 2008. **155**(3): p. C117-C126.
28. Dey, S., M.K. Gunjan, and I. Chattoraj, *Effect of temper on the distribution of pits in AA7075 alloys.* Corrosion Science, 2008. **50**(10): p. 2895-2901.
29. Park, J. and A. Ardell, *Microchemical analysis of precipitate free zones in 7075-A1 in the T6, T7 and RRA tempers.* Acta metallurgica et materialia, 1991. **39**(4): p. 591-598.
30. Gao, Y.X., et al., *The effect of porosity on the fatigue life of cast aluminium-silicon alloys*.* Fatigue & Fracture of Engineering Materials & Structures, 2004. **27**(7): p. 559-570.
31. Shyam, A., J. Allison, and J. Jones, *A small fatigue crack growth relationship and its application to cast aluminum.* Acta materialia, 2005. **53**(5): p. 1499-1509.
32. Li, P., et al., *Quantification of the interaction within defect populations on fatigue behavior in an aluminum alloy.* Acta Materialia, 2009. **57**(12): p. 3539-3548.

Chapter 5

Microstructural characteristics of pitting corrosion and effect of prior corrosion on fatigue performance of AA6061-T6

In this chapter, the effect of crystallographic texture on pitting susceptibility and fatigue performance of aluminum alloy AA6061-T6 were investigated. Characteristics of pitting corrosion and fatigue crack initiation were examined using SEM and OIM based analysis technique. The results show that pits formed by iron-containing particles have smooth profile, which is markedly distinguishable from crystallographic pits. Crystallographic pits were found to be the main cause of fatigue failure and preferably initiate from the inside of grains having orientation close to $\langle 001 \rangle$*. OIM analysis revealed that critical fatigue crack nucleated from grain boundaries that were damaged by corrosion processes around a crystallographic pit. Fatigue crack nucleation was further assisted by surrounding grains that have multiple active slip systems associating with high Schmid factor value. Fatigue endurance along rolling direction is higher than along transverse direction due to the morphology of crystallographic pits and grain texture.*

5.1 Introduction

Pitting corrosion in conjunction with fatigue is a complex phenomenon involving various processes and mechanisms. There are a number of factors that can affect the corrosion fatigue performance of materials, for instance, temperature, corrosive environment, stress state, load-time history and microstructure of materials. Previous studies [1, 2] have demonstrated that pitting of pure aluminum is highly dependent on crystal orientation. It was reported that pH value and chloride concentration are critical factors that determine dissolution rates of face-centered cubic Aluminum single crystal with various orientation [3, 4]. In order to enhance its mechanical performance, several alloying elements are included into aluminum. These elements produce inhomogeneity into the microstructure of aluminum, which adjusts the pitting potential and makes the pitting processes more complicated [5]. In combination with fatigue, there is a lack of supporting evidence where and when critical fatigue cracks initiate under a corrosive environment. Largest or deepest pits are not always associated with fatigue crack initiation as reported by previous investigators [6, 7]. These observations indicate the importance of microstructures, grain orientation as well as the role of pit morphology, pit proximity on the corrosion fatigue behaviors of aluminum alloys. Furthermore, rolling processes, which cause anisotropic properties in materials, considerably affect corrosion and fatigue performance of aluminum alloys along longitudinal and transverse directions. During service life in an offshore environment, a structure could encounter fatigue loads from various directions. However, the effects of microstructures of materials on pitting susceptibility and anisotropic fatigue performance of aluminum alloys subjected to prior corrosion have not been sufficiently investigated.

Recent developments in microstructural analysis and measurement using electron backscattered diffraction (EBSD) techniques have enhanced our understanding of corrosion and fatigue crack initiation mechanism as well as pit to crack transition to a great extent [8]. This chapter investigates the effect of microstructures on corrosion behaviors and fatigue performance of hot rolled AA6061-T6 to provide a realistic life prediction for structures operating in an offshore environment. The effects of grain texture and surface morphology of corrosion pits on fatigue crack initiation were analyzed by the use of Orientation imaging microscopy. Moreover, the preferred orientation of grains having high susceptibility to pitting was identified that could offer an important contribution to corrosion resistance aspect.

5.2 Materials and testing

The material investigated in this study was AA6061-T6 in the form of rolled sheet, which is 4.06mm in thickness. The chemical composition of this alloy was shown in Table 3.2 of chapter 3. The grain of this alloy has a pancake-shaped structure with the average size of $100.2 \times 87.6 \times 27.8 \mu m^3$ $(L \times T \times S)$ as shown in Figure 5.1. From the color code of inverse pole figure (IPF) map, it can be seen that grains are randomly orientated which indicates a weak texture in this aluminum alloy.

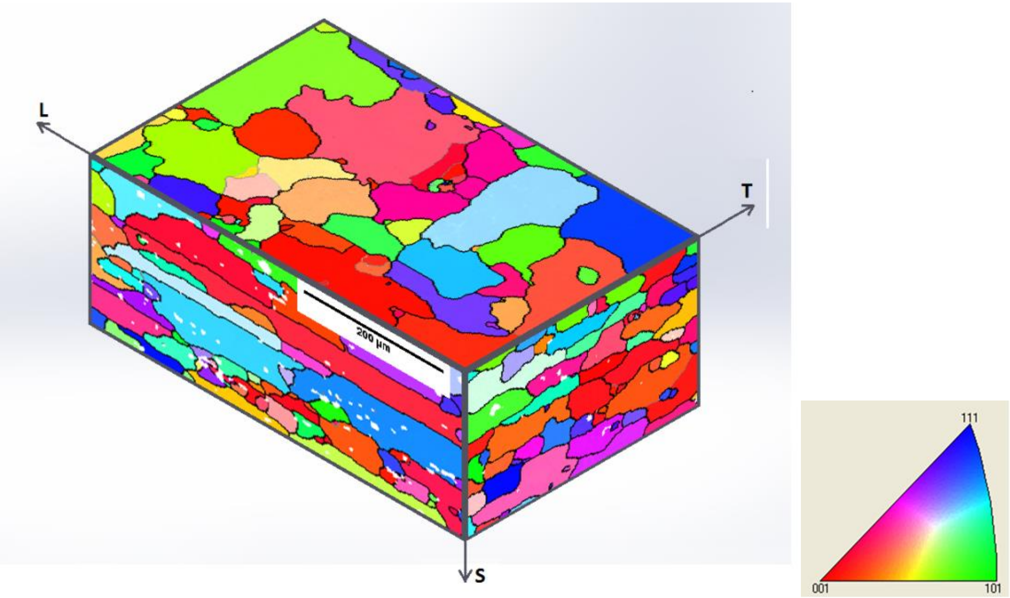

Figure 5.1 Grain structure of AA 6061-T6

In order to investigate the effect of rolling induced anisotropy on corrosion and fatigue performance of AA6061-T6, corrosion test was carried out on surfaces normal to three principle directions, namely longitudinal (L), transverse (T) and short transverse (S) directions. Prior to corrosion test, the specimen surfaces were ground with subsequent use of 800 and 1200 grit SiC paper followed by fine grinding with 9-micron diamond suspension. Final polishing was finished by 3-micron diamond and colloidal silica 0.04-micron suspensions. These surfaces were exposed in simulated seawater 3.5% NaCl for 1, 6, 12, 24,120 and 240 hours, respectively, in accordance with American Society for Testing and Materials (ASTM) standards G1-03 and G46-94. The immersion times were chosen to provide a systematically increasing of corrosion damage level that is adequate for evaluating fatigue performance. After immersion test, corroded samples were cleaned by ultrasonic with the purpose of totally removing corrosion products.

Tensile and fatigue tests were carried out using MTS 810 Material Testing System with the samples fabricated along rolling direction (LT samples) and transverse direction (TL samples). Test specimens were designed according to ASTM standards E466-07 with the dimensions shown in Figure 5.2.

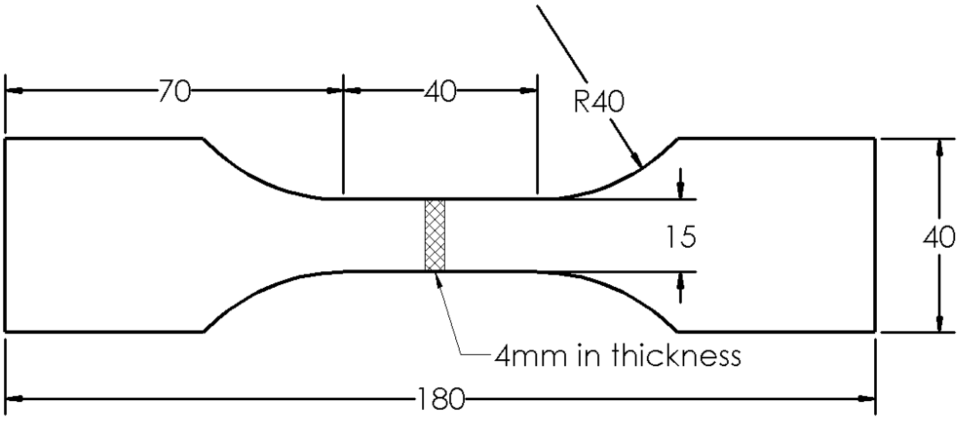

Figure 5.2 Sample dimensions for tensile and fatigue tests

Surfaces of reduced section were polished to ensure the maximum surface roughness R_a is less than 0.15μm. Displacement rate of tensile tests was set up at 0.5 mm/min. Ultimate and tensile yield strength of AA6061-T6 along rolling and transverse directions were determined to be 327.5MPa and 257.4MPa; 328.5MPa and 248.9MPa, respectively. Figure 5.3 presents stress-strain relationship of this aluminum alloy along rolling direction and transverse direction. As aluminum alloys do not exhibit a yield point, tensile yield strength was determined by an offset yield point at 0.2% strain.

Fatigue endurance of as-received samples was measured under fully reversed tension-compression loading (load ratio $R = -1$) at room temperature. A sinusoidal load waveform with frequency of 5 Hz was used in this study. After obtaining the plot of S-N curve for non-corroded samples, maximum stress amplitude of 140MPa was chosen for corroded samples to evaluate fatigue performance of this aluminum alloys when subjected to different pre-corrosion periods. Some fatigue tests were terminated after certain numbers of cycles in order to investigate fatigue crack initiation characteristics of corroded samples. Once a critical fatigue crack was identified, the surrounding area of this crack was shortly polished by colloidal silica 0.04-micron suspension for 2 minutes and then etched by Keller's reagent in 30 seconds to reveal the microstructure for examination.

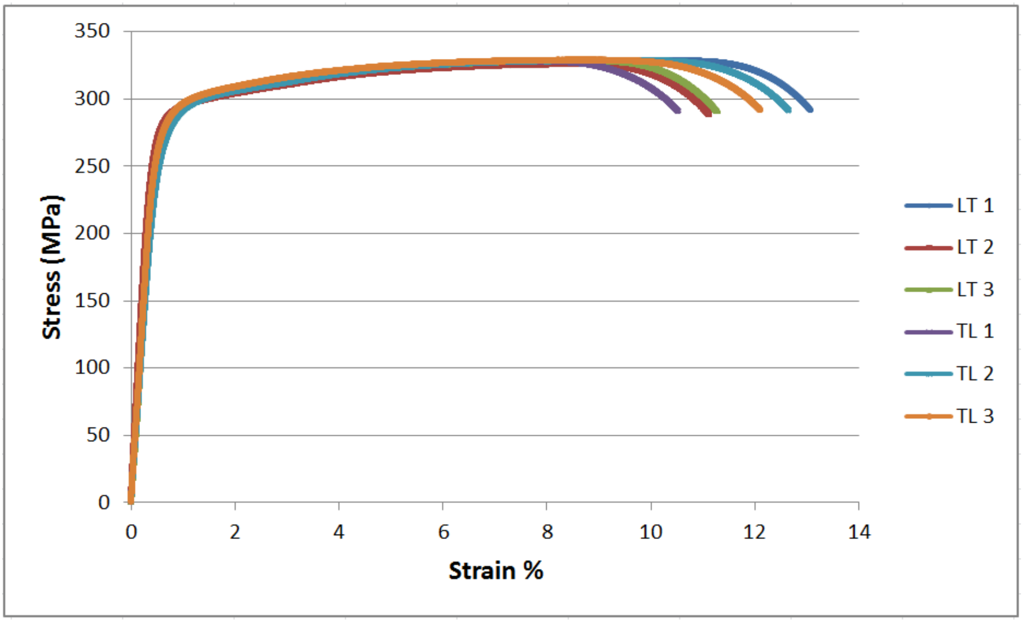

Figure 5.3 Engineering stress-strain relationship of AA6061-T6

Pitting morphology and fatigue crack initiation characteristics of corroded samples were examined using a FESEM JEOL7600 equipped with orientation imaging microscopy. Elemental composition of different intermetallic particles in this aluminum alloy was identified using Energy dispersive X-ray spectroscopy (EDS). Profiles of corrosion pits were measured by a 3-D profilometer with the resolution of 2µm.

5.3 Microstructural characteristics and corrosion behaviors of AA6061

In order to evaluate corrosion damage of the test, the microstructure of polished specimens was examined prior to immersion. Figure 5.4 shows EDS analysis of various intermetallic particles of AA6061-T6 and their corresponding spectra.

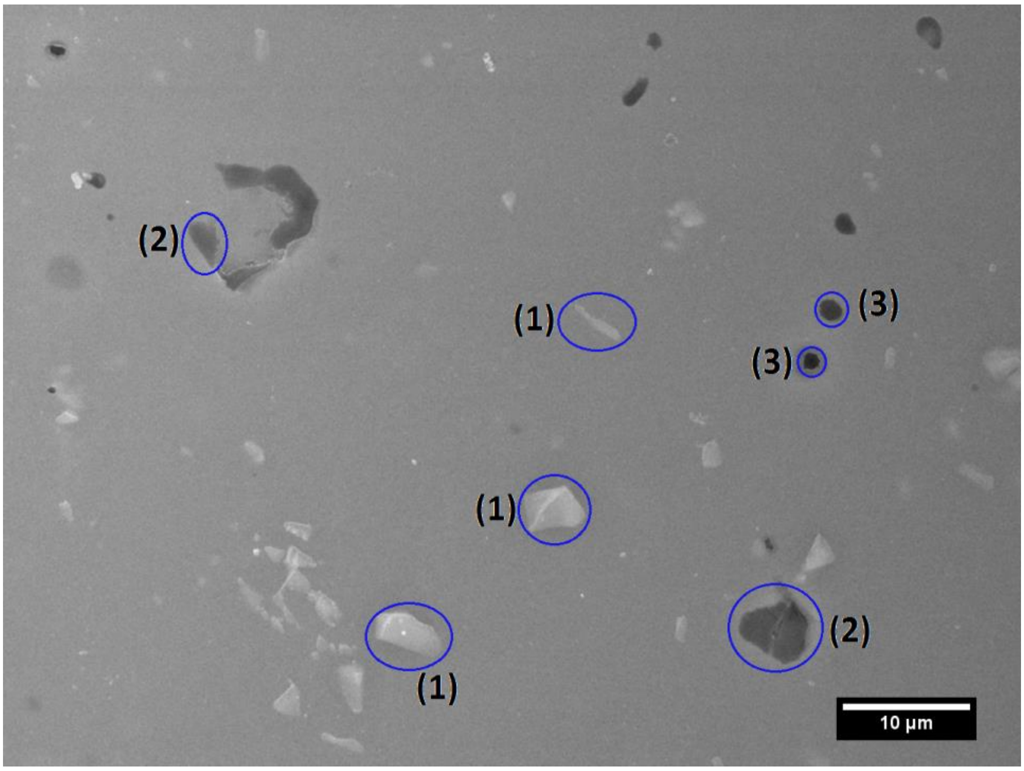

SEM image of intermetallic particles

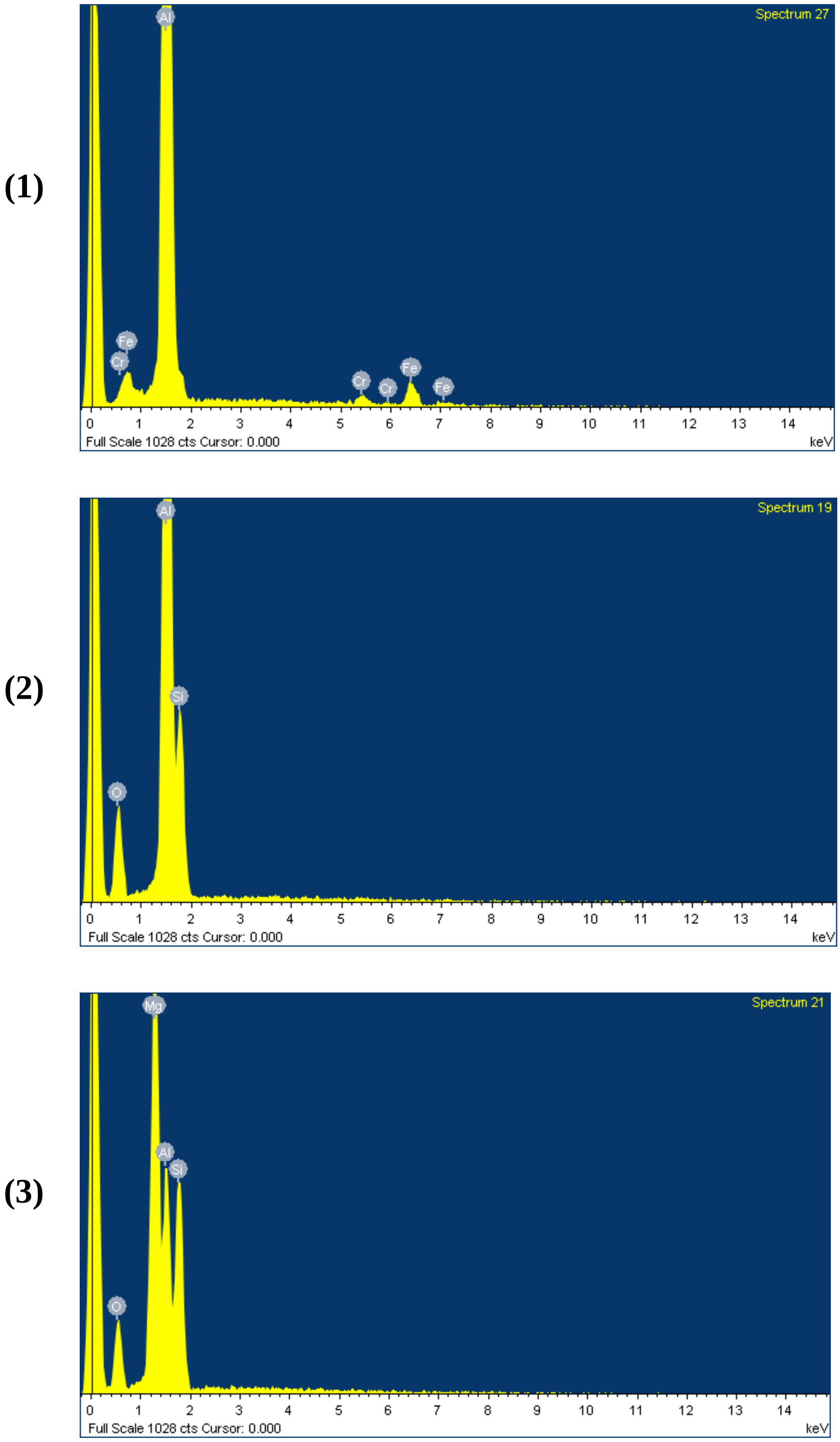

Figure 5.4 SEM image of intermetallic particles and their corresponding spectra (1) Al(Fe,Mn,Cr); (2) Al(Si); (3) Al(Mg_2Si)

The results indicate that there are three main types of intermetallic particles in this aluminum alloy. Al(Fe,Mn,Cr) particles have typical shape of needles or plates with their size could be up to 300 μm^2. They are abundantly distributed over the whole surface and have a bright tone in SEM image. Al(Mg_2Si) and Al(Si) particles are smaller in size and less frequently observed than Al(Fe,Mn,Cr) particles. These types of particles have an irregular shape and appear to be dark in SEM image, where Al(Mg_2Si) particles are slightly darker. The chemical composition of intermetallic particles that were found in this study is in conformity with that inspected by previous work for the same alloy [9, 10].

The formation and evolution of pitting damage were investigated by SEM/EDS analysis in conjunction with OIM after various corrosion times to elucidate the corrosion behavior of AA6061-T6 in artificial seawater 3.5% NaCl. It was found that this alloy is subjected to two different types of localized attack resulting in the formation of hemispherical pitting and crystallographic pitting. Figure 5.5 presents the SEM images of pits, which have hemispherical morphology on the surfaces of LT, LS, and TS after 24 hours of immersion. This kind of pitting has certain characteristics that are markedly distinguishable from crystallographic pits shown in Figure 5.6. The hemispherical pits have smooth morphology and are smaller in size (pit diameter ranging from a few microns to maximum of 30 microns after 240h immersion) compared to crystallographic pits, which could develop up to 250 microns in diameter. EDS analysis revealed that this type of pitting was formed by the alkalization processes around Al(Fe,Mn,Cr) precipitates. Various researchers have reported similar corrosion behaviors when cathodically polarizing aluminum alloys in aerated NaCl solution [11, 12]. The formation of this type of pitting when the sample is freely corroded in 3.5% NaCl solution can be explained by the fact that cathodic reactions, supported by iron-containing particles, locally increase the pH value of test solution which in turn leads to the dissolution of surrounding aluminum matrix. Since this type of pitting developed from

Al(Fe,Mn,Cr) particles, it was found to be numerous and occupies up to 8% of surface area after 24 hours of immersion.

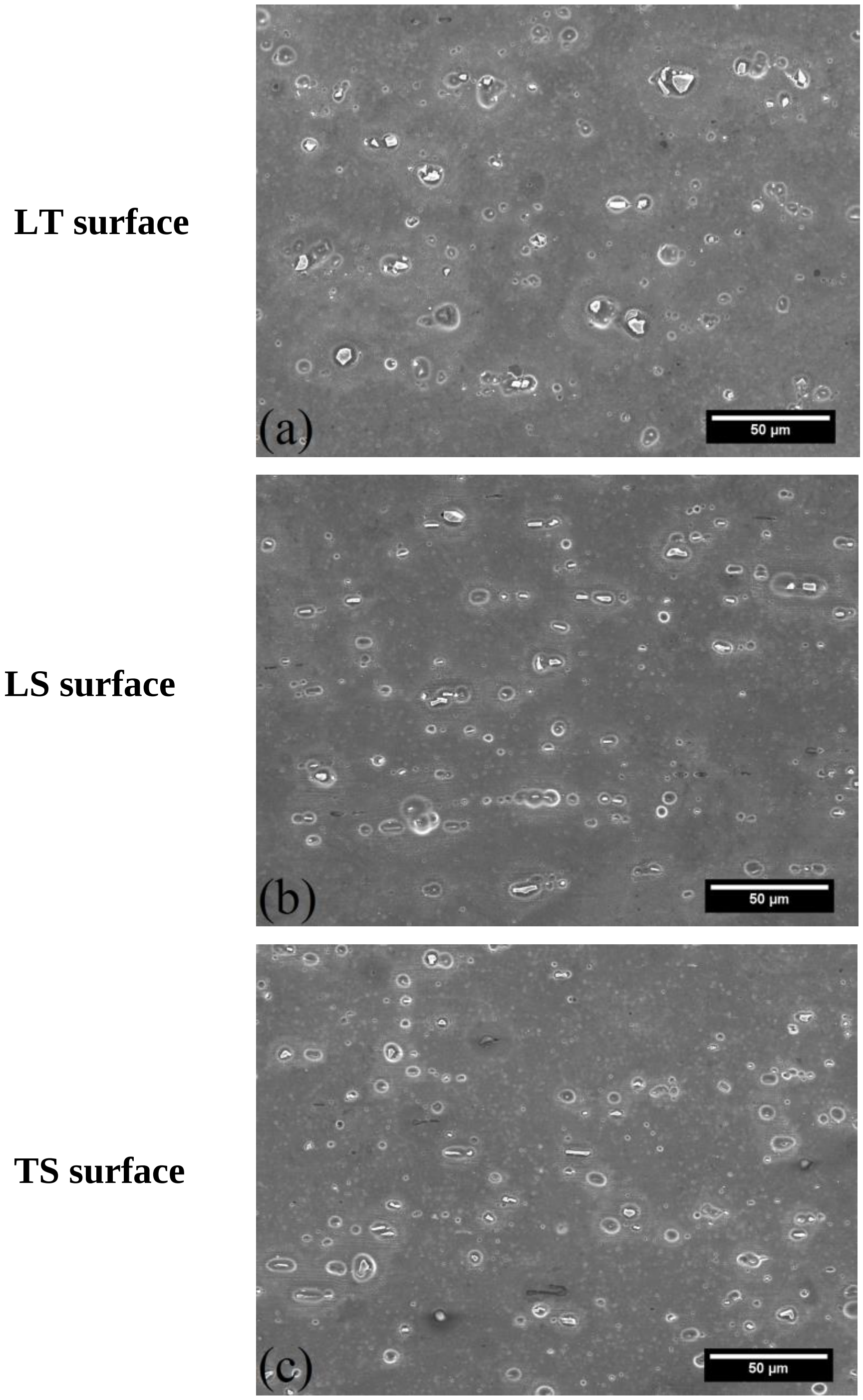

Figure 5.5 SEM images of hemispherical pits after 24 hours of immersion on (a) LT surface; (b) LS surface and (c) TS surface

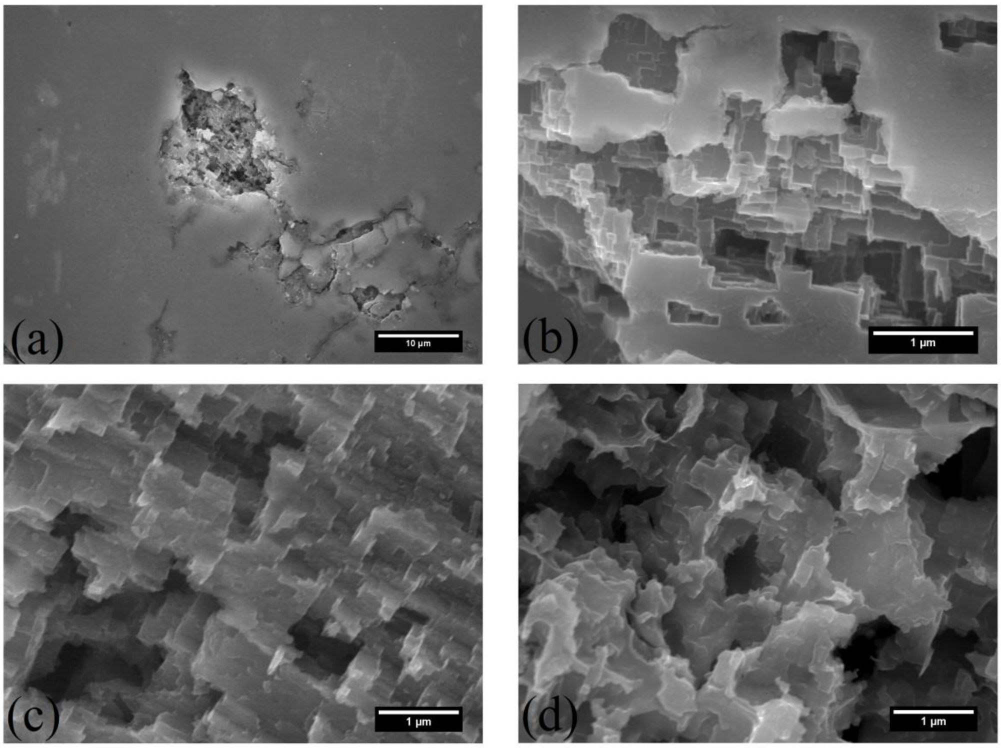

Figure 5.6 (a) SEM image of a crystallographic pit on LT surface after 1 hour corrosion and morphological details of crystallographic pits after (b) 1h; (c) 12h; (d) 120h corrosion

As can be seen in Figure 5.5, there are many remnants of Al(Fe,Mn,Cr) particles at the bottom of pits while Al(Mg_2Si) and Al(Si) particles remain intact and are not affected as corrosion time increases. Many intermetallic particles are fractured and allocated along the rolling direction on L-T and L-S surfaces while particles on T-S surface scatter randomly as a result of rolling processes. This leads to the preferred distribution and orientation of hemispherical pits along the rolling direction. As corrosion time increases, there is a development of an oxide layer on the surface of corroded samples. However, the alkalization processes around Al(Fe,Mn,Cr) particles impede the formation of this oxide film and continue to develop until those particles are completely detached from the matrix due to the dissolution of the contact area.

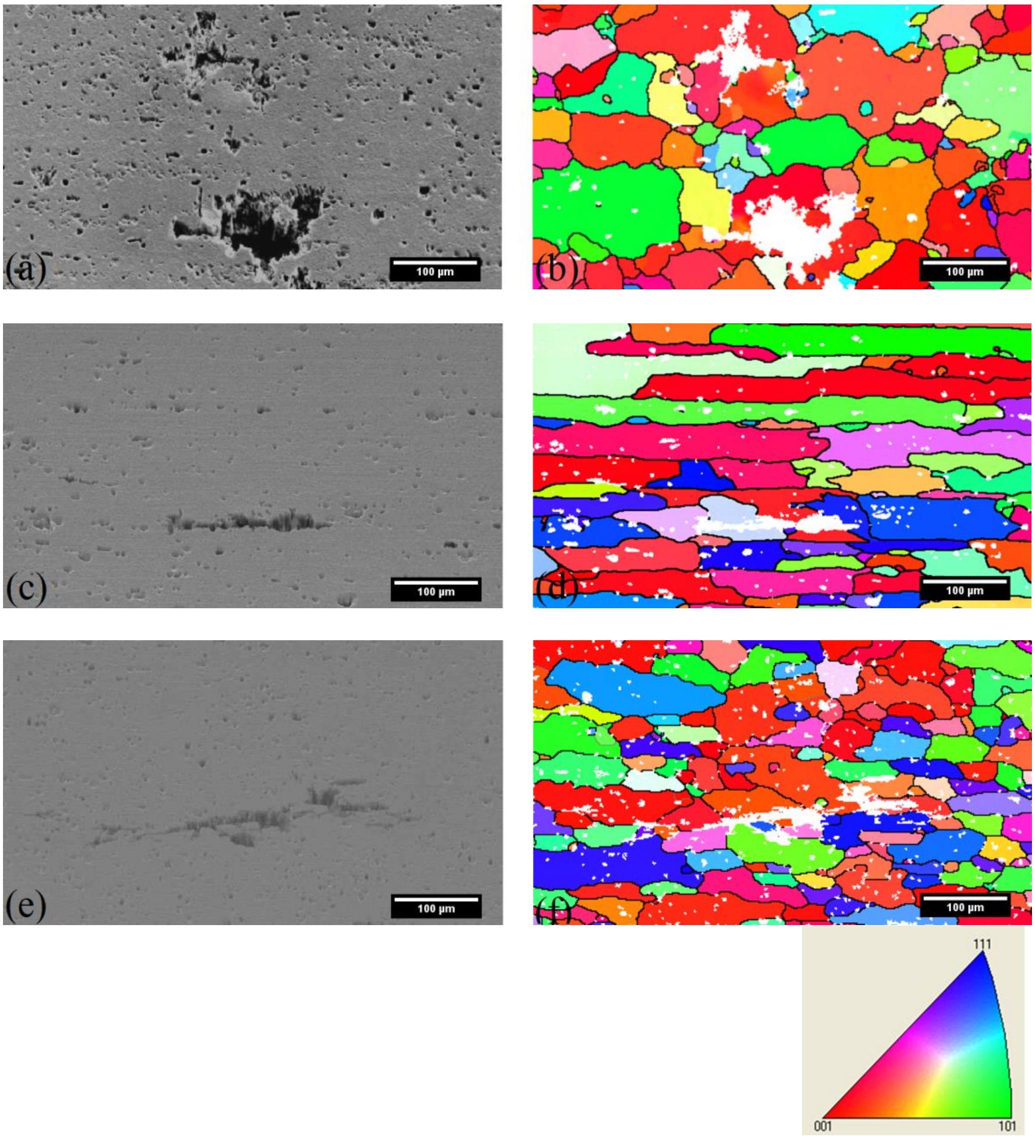

Figure 5.7 SEM images and corresponding IPF maps of crystallographic pits on (a,b) LT surface; (c,d) LS surface and (e,f) TS surface

In contrast to the smooth appearance of hemispherical pits, Figure 5.6 showed pits with very rough morphology. At high magnification, it can be observed that these pits have rectangular shape with many sharp facets referred by previous authors [13, 14] to be {001} crystallographic planes. Previous authors [1, 15] who studied corrosion of single fcc Aluminum crystals reported that pitting potential of single crystal fcc Al in 0.5M NaCl solution reduced in the order $\{001\} > \{110\} > \{111\}$. This means dissolution rate and corrosion severity of pure Al crystals increase in the order $\{001\} < \{110\} < \{111\}$. Davis and Koroleva [2, 3] also demonstrated that dissolution rate of pure Al in HCl is highest at planes close to $\{001\}$. However, Takayama [5] stated that corrosion severity of pure Al in HCl solution is higher on $\{001\}$ planes at low concentration of HCl while $\{111\}$ planes corrode faster at high concentration. Therefore, it can be concluded that the critical potential that initiates crystallographic pitting in Aluminum alloys depends not only on crystal orientation but also on the alloying elements and corrosion environments. An interesting finding in this study is that during the first stage of corrosion process, faceted pitting of AA6061-T6 preferably initiated from the inside of grains, which have orientation close to $\langle 001 \rangle$ directions denoted by the red color in OIM images (Figure 5.7). Davis [16] examined morphology of corrosion pits on single crystals of aluminum and reported that (110) and (111) orientated crystals have pits with V-shaped and tetrahedral morphology respectively while pits with rectangular morphology were observed in (001) orientated crystals. The rectangular morphology of crystallographic pits after one-hour corrosion as shown in Figure 5.6(b) confirmed the observations from OIM images that grains having $\langle 001 \rangle$ orientation are more susceptible to this type of corrosion. The surface profiles of these pits are also influenced by the texture of grains. On LT surface, crystallographic pits have equiaxed shape and are slightly elongated along rolling direction. On the other hand, pits on LS and TS surfaces are stretched out with respect to the grain texture. The formation of crystallographic pits is associated with anodic reactions of aluminum alloys in a corrosive environment. As reported by Aballe [11] who investigated corrosion process of AA5083, the initiation of crystallographic pits required anodic polarization at current density above a critical level. Once faceted pits formed, the local environment becomes acidic and creates a precipitate free zone nearby which facilitates intergranular corrosion at pit walls as can be seen in Figure 5.6(a) and 5.7(a). It should be noted here that intergranular corrosion only occurred around the perimeter of crystallographic pits. The areas that do not crystallographically pit are invulnerable to intergranular corrosion.

In order to have an estimation of the corrosion damage of crystallographic pitting, critical pit depth as well as pit profile after various corrosion times were measured using a 3-D profilometer. The depth of crystallographic pits in this study was observed to follow Godard's model [17]:

$$d_{max} = At^{\alpha} \tag{5.1}$$

where $d_{max}$is the maximum pit depth (μm), t is corrosion time (hour),A and α are experimental parameters depending on materials properties and corrosion environment. By fitting the measured depth from profilometer, the constants A and α in equation (5.1) were found to be 11.88 and 0.2 in this study. Figure 5.8 shows the measured profile of corrosion pits and the plot of maximum pit depth with respect to immersion time.

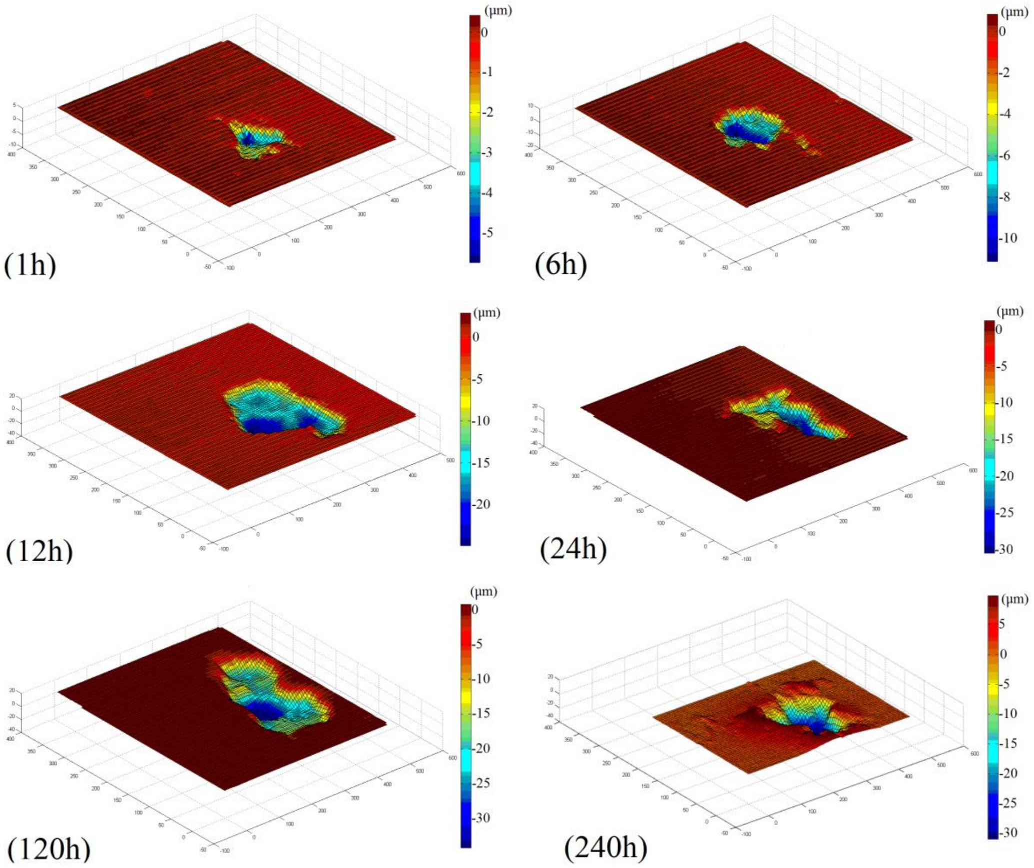

(1h) (6h)

(12h) (24h)

(120h) (240h)

Measured profile of corrosion pits

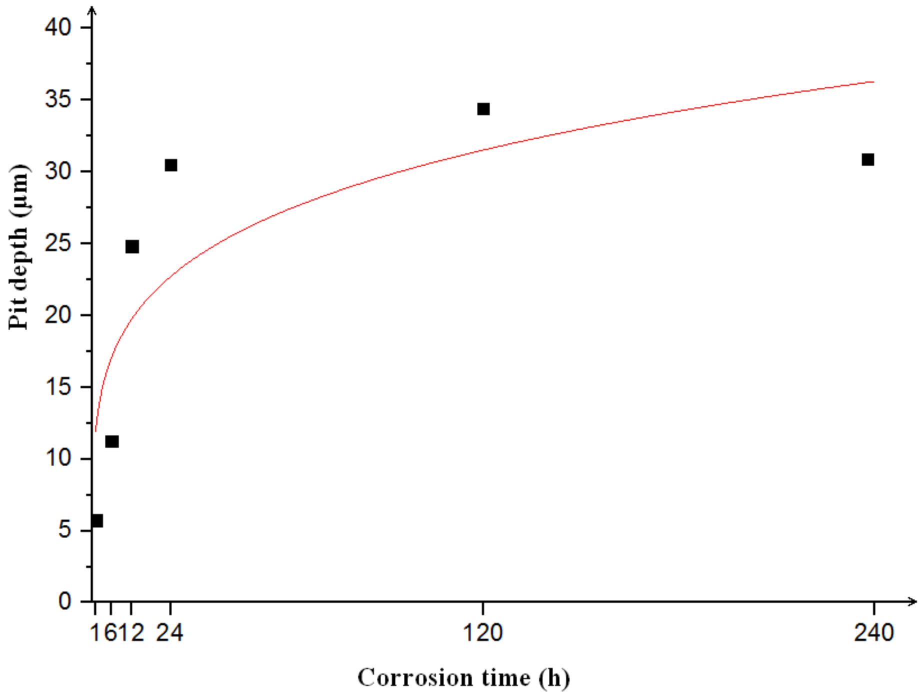

Figure 5.8 Measured profile of corrosion pits and the plot of maximum pit depth with respect to immersion time

From Figure 5.8, it can be seen that the attack of crystallographic pits is only significant during the first day of immersion. The morphology of crystallographic pits appears to play an important role in the behavior of pit development. As corrosion time increase, the sharp facets of crystallographic pits become rounded (Figure 5.6(d)) and pitting process does not significantly attack the materials although tunneling may occur below the pitting surface. The changes of pit morphology could result in local modification of pitting potential within crystallographic pits. Surface energy or metallic bonding was mostly used to describe the corrosion progress of crystallographic pits. Breakdown of oxide layer has also been used to analyze relationships between pit propagation and crystallographic orientation. However, there is no general consensus to explain for the propagation of oriented pits. Further investigation is required to elucidate the propagation mechanism of pitting corrosion of aluminum alloys in a corrosive environment.

5.4 Effect of prior corrosion on fatigue performance

In order to quantify the effects of pitting corrosion on fatigue performance of this aluminum alloys, fatigue lives of non-corroded samples, as well as corroded samples after various corrosion times, were measured. In Figure 5.9, the cyclic stress amplitude versus cycles to failure of as-received samples fabricated along rolling direction and transverse direction were compared and plotted in logarithmic scale. It can be seen that this aluminum alloy does not exhibit a strong anisotropic fatigue performance although the grain structure was affected by rolling processes. There is a linear relationship between fatigue life N and maximum stress amplitude S in logarithmic scale, which can be described by the following equation:

$$logN = logA - mlogS \tag{5.2}$$

where, m is the slope and $logA$ is the intercept. The fitting curve of fatigue endurance in Figure 5.9 has m equals to *9.8* and A equals to *1.42*$\times 10^{27}$

In contrast with isotropic fatigue performance of non-corroded AA6061-T6 samples, we can observe that samples fabricated along rolling direction have better fatigue performance than transverse samples when subjected to prior corrosion as shown in Figure 5.10. At each corrosion intervals, four samples were tested, and the calculated values of average fatigue lives were indicated. The anisotropy fatigue behavior of this aluminum alloy, when subjected to prior corrosion, can be attributed to the variations of pit morphology on three principle surfaces LT, LS, and TS. For non-corroded samples, fatigue cracks can initiate from either LT or LS surfaces although LT surface is preferential for fatigue crack formation. However, corroded samples were always failed by a crack originating from LT surface due to the orientation along the loading direction of pits on LS and TS surfaces. As discussed in section 5.3, crystallographic pits on LT surface are slightly stretched out along rolling direction because of grain texture. Therefore, pits on LT surface of longitudinal samples have less stress concentration in comparison with transverse samples since they are orientated along loading direction. The anisotropic fatigue performance becomes significant after 6 hours of corrosion where fatigue lives of TL samples are only 70% compared to that of LT samples.

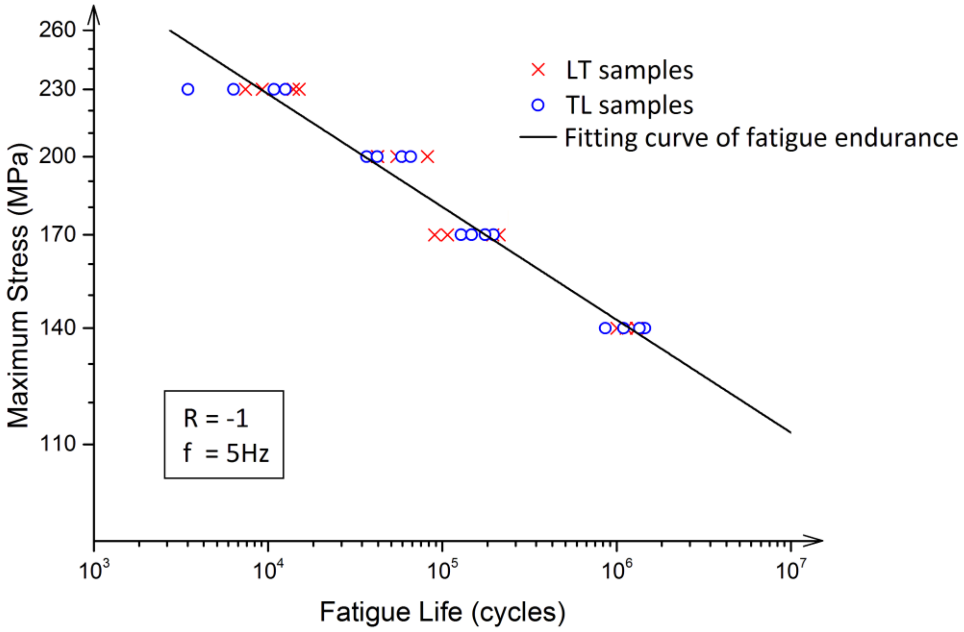

Figure 5.9 Relationship between stress amplitude and cycles to failure of AA6061-T6

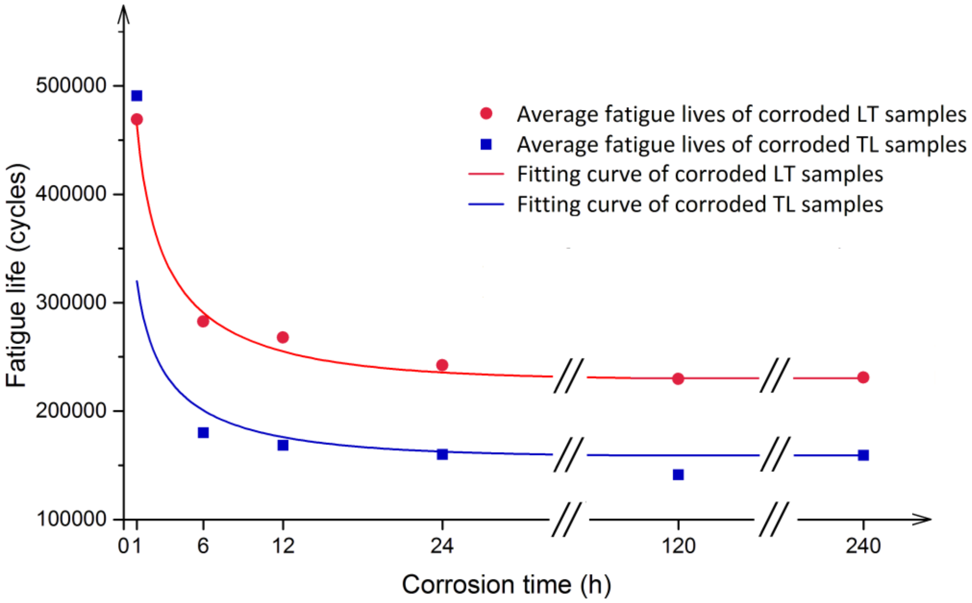

Figure 5.10 The effect of corrosion time on fatigue performance of samples fabricated along rolling direction and transverse direction

Compared with the plot of maximum depth of crystallographic pits in Figure 5.8, we can observe a dramatical decrease of fatigue life in association with a substantial escalation of pit depth within one day of corrosion. It can be concluded that evolution of crystallographic pits is the main cause of fatigue reduction of AA6061-T6 corroded in artificial seawater NaCl 3.5%.

The formation of crystallographic pits functions as stress concentration sites that produce a significant increase in the intensity of stress field and enhance localized damage causing crack initiation. Even one hour of immersion can cause a degradation of more than 50% fatigue life, which indicates the initiation time of a fatigue crack is reduced by a half. After 24 hours of corrosion, fatigue lives of corroded samples reach a threshold value as corrosion processes of crystallographic pits do not considerably develop after 24 hours of immersion as discussed in the previous section.

Based on the fatigue life results of corroded samples, a constitutive equation to estimate fatigue life (N) versus corrosion time (t) was proposed using the exponential law:

$$N = A(1 - e^{-bt})^{\ c}\ (1) \qquad (5.3)$$

where, b and c are decay constants which were estimated to be *0.1* and *-0.3*

A is the offset value which indicates the threshold value of fatigue life of AA6061-T6 when subjected to prior corrosion. At the stress level of 140MPa in this study. It was calculated to be 229027 for LT samples and 158084 for TL samples.

Although, there are a number of factors that can affect the corrosion fatigue performance of materials, for instance, temperature, stress state, load-time history and microstructure of materials. The equation (5.3) can be used as a guideline for structural design to determine the stress level that a structure, subjected to prior corrosion and subsequent fatigue damage, can operate safely within the threshold value of fatigue life.

5.5 Fatigue crack initiation characteristics

To better understand the corrosion fatigue behavior, it is important to characterize the effect of microstructure on pit-to-crack transition. Crack initiation behavior of corroded samples was examined by SEM in conjunction with OIM.

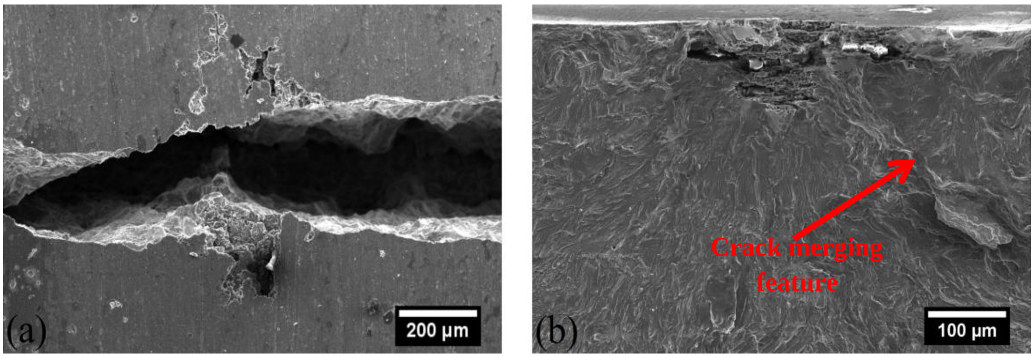

Figure 5.11 (a) Typical fatigue crack developed from a crystallographic pit and (b) fracture surface

Figure 5.11(a) revealed the location of a fatigue crack on the free surface of a corroded sample. We can clearly see that critical fatigue crack, which caused material failure, nucleated from a crystallographic pit on the free surface. Three stages of fatigue damage were identified from the fracture surface in Figure 5.11(b): crack initiation, crack propagation and final fracture. Cleavage fractures are clearly observed in short crack growth region, which indicates transgranular propagation of fatigue crack. These cleavage lines exhibit a radiating pattern which can be traced back to fatigue crack origin which is a crystallographic pit. Below the corroded surface, crystallographic tunnels formed and crept into the material. Therefore, the measurement of pit profile and depth can only give an estimation of corrosion damage as well as stress concentration. Propagation region appears to be flat near crack origin and becomes fibrous as crack grows further. When crack grows to a critical size, final failure occurred by shear fracture where micro-voids coalesce and form dimples on the fracture surface.

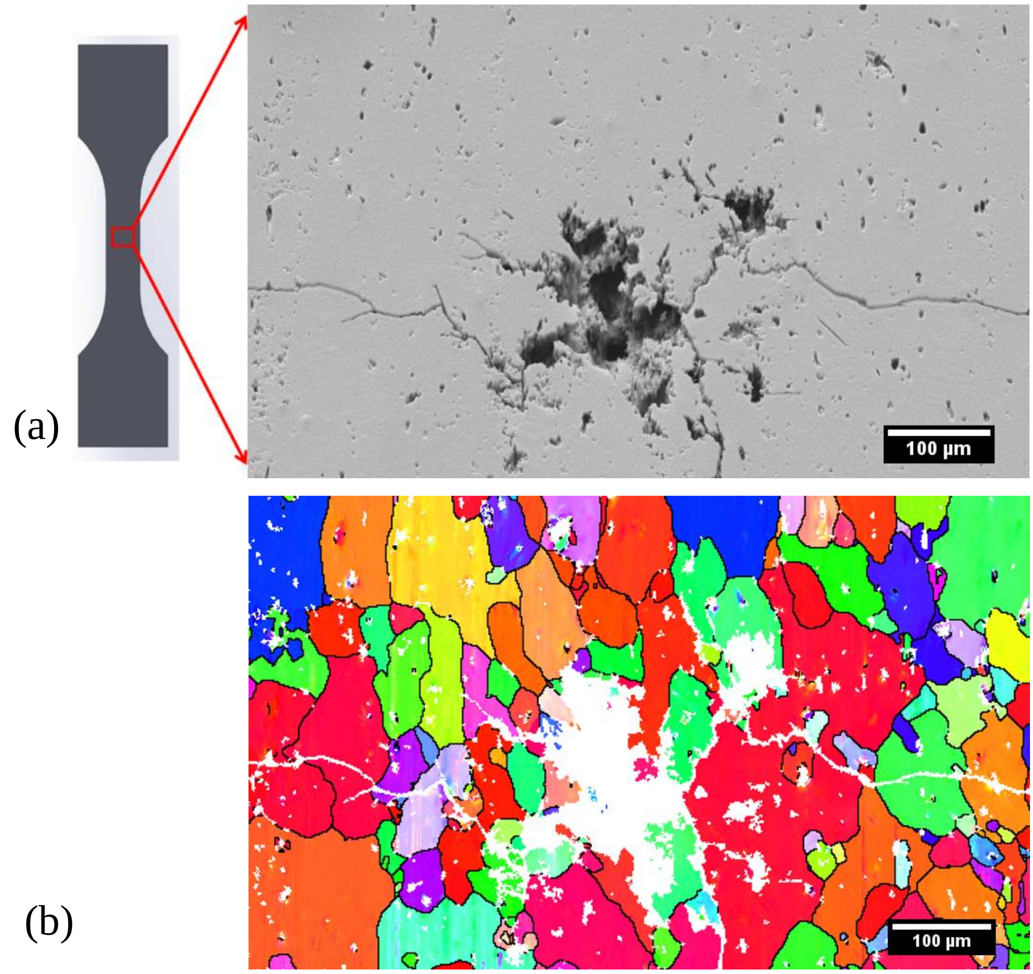

Figure 5.12 Fatigue crack initiation of a 12-hour corroded sample subjected to 200000 fatigue cycles. (a) SEM image, (b) corresponding IPF map

In order to characterize the effect of microstructure on pit to crack transition, fatigue tests were terminated prior to failure at various intervals and the crack nucleation sites were analyzed by OIM. It was noticed that fatigue cracks are only visually detected after 80% of fatigue life under an optical microscope with a magnification of 500 times. Figure 5.12 shows the orientation map of an area around a crack nucleation site on a LT sample. It can be seen that the initiation of fatigue crack is intergranular at the first stage. Fatigue cracks initiate from grain boundaries at both sides of pit mouth, which were attacked by prior corrosion processes.

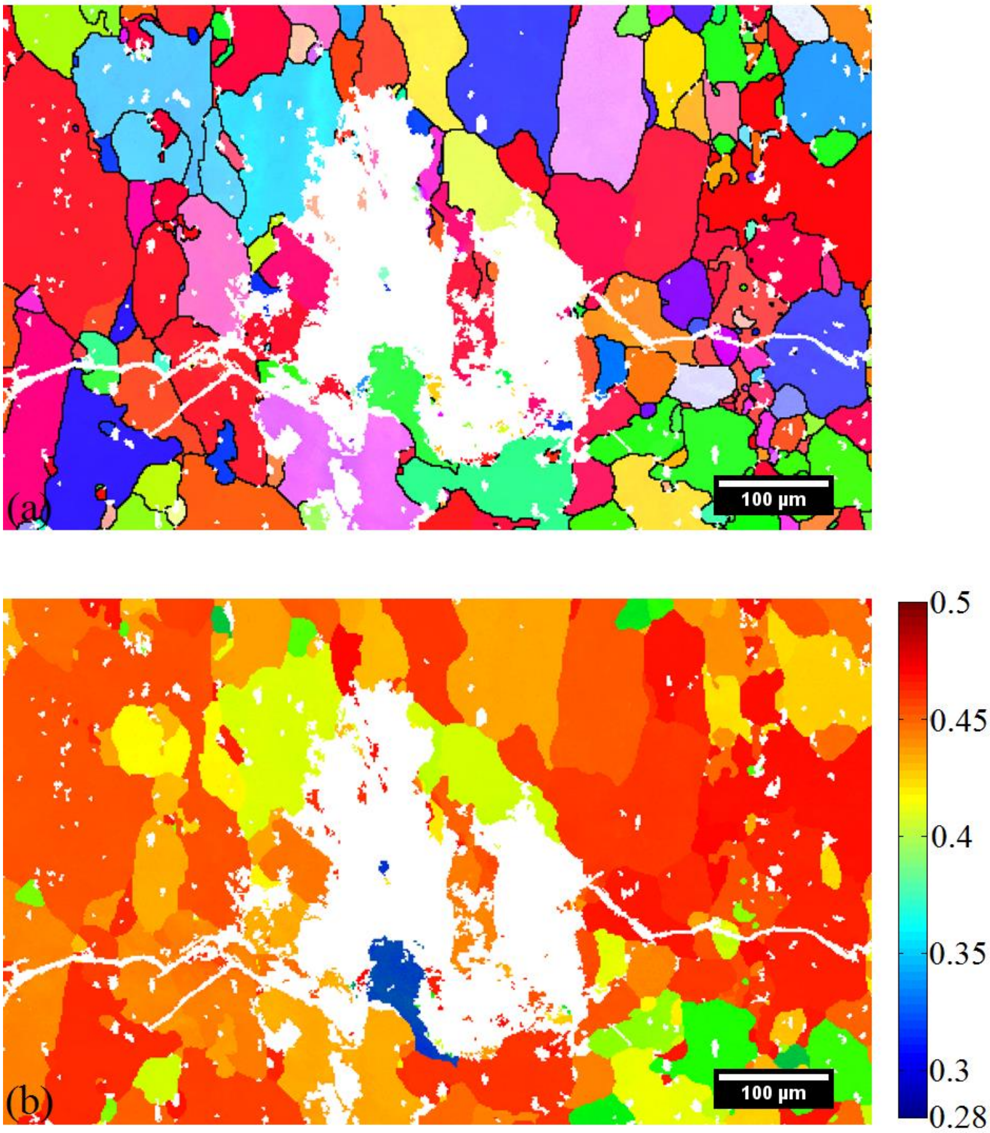

Figure 5.13 Subsurface damage of a 12-hour corroded sample subjected to 200000 fatigue cycles. (a) Euler map and (b) Schmid map

After further polishing the sample to reveal subsurface damage as shown in Figure 5.13, we can see that the initiation of fatigue crack during the next stage is transgranular along the direction of maximum shear stress, which is 45^o relative to the loading direction. Since Aluminum has face center cubic (FCC) crystal structure, Schmid Factor was calculated from OIM data using the primary slip system of <111> planes along <110> directions with respect to the direction of applied load. The grains that fatigue crack nucleates have relative high Schmid factor values (0.45 to 0.48). Previous authors [8, 18, 19] have demonstrated that grains having high value of Schmid factor possess many active slip systems in them. Thus, the results obtained from OIM analysis indicates that critical fatigue crack preferably developed from a crystallographic pit surrounded by multiple active slip systems and grain boundaries damaged by prior corrosion processes.

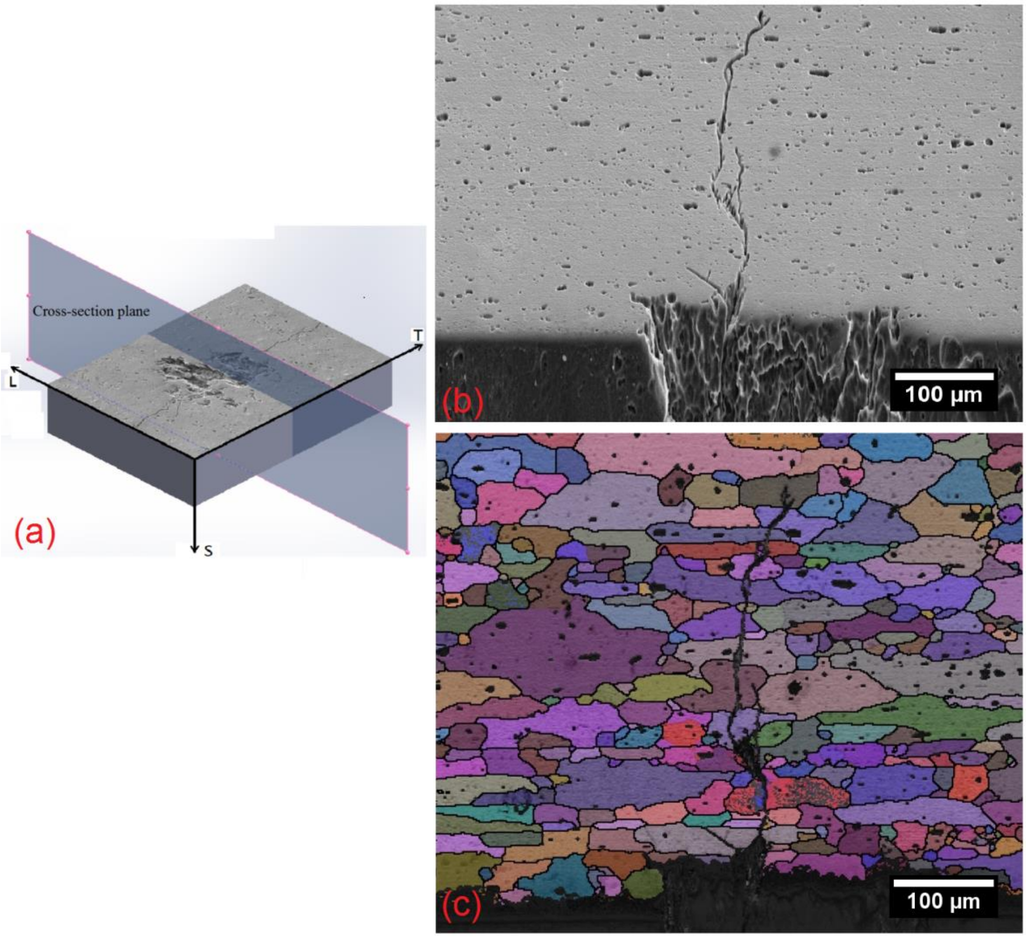

Figure 5.14 Cross section view of a crystallographic pit initiating fatigue crack. (a) Illustration of cross-section plane; (b) projected view SEM image of cross-section area; (c) corresponding Euler map of cross-section area

Figure 5.14 reveals the cross-section view at the center of a crystallographic pit that initiates fatigue crack. It can be observed that there are two fatigue cracks propagating into the material. This indicates that fatigue cracks were firstly formed at both sides of pit mouth, which are the highest stress concentration locations. As soon as these two cracks propagate further, they merge into a single fatigue crack that leads to fatigue failure. As can be seen in Figure 5.11(b), there is a tearing ridge on the fracture surface, which was formed at the area that fatigue cracks from both sides of pit mouth connect to each other. From the cross-section view, we can also see that pits developed faster on the free surface than in depth due to the morphology of grain structure. It confirmed that pitting potential is strongly dependent on grain orientation as well as grain morphology. The preferred dissolution of certain orientated grain having higher pitting potential than neighbor grains could explain for the development of crystallographic pits through tunneling. Figure 5.13 also reveals that grain orientation governs the propagation of crack's path by active slips systems during short crack growth region. The crack path is not perpendicular to loading direction while many secondary cracks, which are 45^{o} in relative to the applied stress direction, can be found around the main crack. Furthermore, the existence of nearby crystallographic pits could also affect the crack path. Once fatigue crack developed to a stable state, it propagated transgranularly on the plane normal to the maximum principle stress. Microstructures of corroded surface no longer affect the crack path, as the resistance to crack evolution is dependent on materials properties as a bulk metal at this stage.

5.6 Conclusion

In this chapter, the corrosion and fatigue behaviors of AA6061-T6 were investigated with the great assistance of OIM analysis. The following conclusions can be drawn from this study:

- There are two types of pitting occurring in AA6061-T6: hemispherical pitting and crystallographic pitting. Crystallographic pits were found to be more detrimental and preferably initiated from the inside of grains that have orientation close to ⟨001⟩.
- As corrosion time increase, the sharp facets of crystallographic pits become rounded and pitting process does not significantly attack the materials although tunneling may occur below the pitting surface.

- Surface morphology of crystallographic pits is strongly influenced by the grain structure on three different principle surfaces LT, LS, and TS. On LT surface, crystallographic pits have equiaxed shape and are slightly elongated along rolling direction. On the other hand, pits on LS and TS surfaces are stretched out with respect to the grain texture. The morphology of crystallographic pits was demonstrated to be a key factor that affects the behavior of pit propagation as well as the anisotropic fatigue performance of aluminum alloys.
- When subjected to prior corrosion, fatigue endurance along rolling direction of AA6061-T6 is higher than along transverse direction due to the morphology of crystallographic pits and grain texture. The evolution of crystallographic pits is the main cause of fatigue life reduction.
- Critical fatigue crack nucleated from grain boundaries that were damaged by corrosion processes around a crystallographic pit. Fatigue crack nucleation was further assisted by surrounding grains that have multiple active slip systems associating with high Schmid factor value.

References

1. Yu, S. and P. Natishan, *Critical factors in localized corrosion III.* by RG Kelly, PM Natishan, GS Frankel and RC Newman, Pennington, NJ, 1999.
2. Davis, B., P. Moran, and P. Natishan, *Metastable pitting behavior of aluminum single crystals.* Corrosion science, 2000. **42**(12): p. 2187-2192.
3. Koroleva, E., et al. *Crystallographic dissolution of high purity aluminium*. in *Proceedings of the Royal Society of London A: Mathematical, Physical and Engineering Sciences*. 2007. The Royal Society.
4. Takayama, Y., M. Sato, and H. Watanabe. *Crystallographic Orientation Dependence of Corrosion Behavior of 5N Purity Aluminum in Different*

Concentrations of HCl Aqueous Solutions. in *ICAA13: 13th International Conference on Aluminum Alloys*. Wiley Online Library.

5. Davis, J.R., *Corrosion of aluminum and aluminum alloys*. 1999: ASM International.
6. Sankaran, K.K., R. Perez, and K.V. Jata, *Effects of pitting corrosion on the fatigue behavior of aluminum alloy 7075-T6: modeling and experimental studies.* Materials Science and Engineering: A, 2001. **297**(1–2): p. 223-229.
7. Clark, P.N. and D.W. Hoeppner, *Pitting Behavior and Residual Fatigue Life of 2024-T3 Aluminum Considering Loading and Sheet Thickness*, in *Journal of the Mechanical Behavior of Materials*. 2002. p. 91.
8. Roach, M.D., et al., *An EBSD based comparison of the fatigue crack initiation mechanisms of nickel and nitrogen-stabilized cold-worked austenitic stainless steels.* Materials Science and Engineering: A, 2013. **586**: p. 382-391.
9. Mutombo, K. and M.d. Toit, *Corrosion fatigue behaviour of aluminium alloy 6061-T651 welded using fully automatic gas metal arc welding and ER5183 filler alloy.* International Journal of Fatigue, 2011. **33**(12): p. 1539-1547.
10. Nikseresht, Z., et al., *Effect of heat treatment on microstructure and corrosion behavior of Al6061 alloy weldment.* Materials & Design, 2010. **31**(5): p. 2643-2648.
11. Aballe, A., et al., *Localized alkaline corrosion of alloy AA5083 in neutral 3.5% NaCl solution.* Corrosion Science, 2001. **43**(9): p. 1657-1674.
12. Zaid, B., et al., *Effects of pH and chloride concentration on pitting corrosion of AA6061 aluminum alloy.* Corrosion Science, 2008. **50**(7): p. 1841-1847.
13. Knörnschild, G., *Mechanism of Pit Growth in Homogeneous Aluminum Alloys*. 2012: INTECH Open Access Publisher.

14. Seo, J.H., J.-H. Ryu, and D.N. Lee, *Formation of crystallographic etch pits during AC etching of aluminum.* Journal of the Electrochemical Society, 2003. **150**(9): p. B433-B438.

15. Yasuda, M., F. Weinberg, and D. Tromans, *Pitting Corrosion of Al and Al‐Cu Single Crystals.* Journal of the Electrochemical Society, 1990. **137**(12): p. 3708-3715.

16. Davis, B.W., *The Influence of Crystal Orientation on the Corrosion Behavior of Aluminum*. 1997, DTIC Document.

17. Godard, H.P., *The corrosion behavior of aluminum in natural waters.* The Canadian Journal of Chemical Engineering, 1960. **38**(5): p. 167-173.

18. Villechaise, P., L. Sabatier, and J.C. Girard, *On slip band features and crack initiation in fatigued 316L austenitic stainless steel: Part 1: Analysis by electron back-scattered diffraction and atomic force microscopy.* Materials Science and Engineering: A, 2002. **323**(1–2): p. 377-385.

19. Bridier, F., P. Villechaise, and J. Mendez, *Analysis of the different slip systems activated by tension in a α/β titanium alloy in relation with local crystallographic orientation.* Acta Materialia, 2005. **53**(3): p. 555-567.

Chapter 6

Corrosion fatigue behavior of AA6061-T6

In this chapter, fatigue crack initiation characteristics and crack growth behaviors of AA6061-T6 when simultaneously subjected to a corrosive environment were investigated using SEM and OIM based analysis technique. High stress concentration at both sides of pit mouth in conjunction with attacked grain boundaries favoured fatigue crack nucleation while the presence of hydrogen formed by corrosion reactions caused crack tip embrittlement and intensified crack growth rate. Fractography analysis showed that there is a change in crack growth mechanism of short fatigue crack when tested in NaCl solution. Near crack origin, which is a crystallographic pit, crack developed transgranularly along crystallographic planes due to Hydrogen-enhanced decohesion process. Further crack growth was dominated by Adsorption Induced Dislocation Emission process resulting in mixed mode of intergranular and transgranular crack growth with higher portion of transgranular. The mathematical concept of pivot point was used to model the transition of crack growth rate during stage II region with different exponential laws.

6.1 Introduction

While aluminum alloys exhibit adequate corrosion resistance in atmospheric environments, they are more susceptible to pitting corrosion when working in offshore conditions due to the presence of chlorides in seawater, which facilitates pitting processes of alloying elements. Pitting corrosion in conjunction with fatigue is a complex phenomenon involving various processes and mechanisms. The pitting processes cause local discontinuities in a structure and enhance the nucleation as well as propagation processes of small fatigue cracks. It has been shown that short cracks can initiate and develop even below the threshold of stress intensity factor determined for long crack growth due to the presence of these local discontinuities [1]. In a corrosive environment, hydrogen is generated by cathodic corrosion reactions and then absorbs at crack tips. There is broad consensus that degradation of crack growth resistance is caused by crack tip embrittlement due to the presence of hydrogen species. Of the many proposals, three most widely accepted interstitial mechanisms are: Hydrogen-enhanced localized plasticity (HELP), Hydrogen-enhanced decohesion (HEDE) and Adsorption Induced Dislocation Emission (AIDE). The HELP mechanism is supported by observations that solute hydrogen facilitates dislocation motion ahead of crack tips by forming an enhanced plastic zone size [2, 3]. The fracture process exhibits plasticity phenomenon like reduction of material yield strength and micro-void coalescences rather than embrittlement. However, this mechanism is only valid in a certain range of temperatures and strain rates. Contradictory results were observed at elevated temperatures and higher strain rates. The second mechanism HEDE assumed that hydrogen adsorption weakened atomic bonds at crack tips resulting in decohesion (tensile separation) along cleavage planes or grain boundaries. Therefore, the fracture surface may exhibit either brittle intergranular or transgranular cleavage. This model originally was proposed by Troiano [4] and further improved by other authors [5, 6]. It is supported by brittle characteristics similarly observed in solid-metal induced embrittlement and metal-vapor induced embrittlement where decohesion occurred in the absence of considerable local deformation. The third mechanism AIDE was proposed by Lynch [7] based on fractographic observations such as extensive localized slip or nanoscopic dimples indicating that crack growth occurred by dislocation movement on suitable slip planes or void coalescence processes. The author assumed that absorption of embrittling species weakened interatomic bonds and thereby enhanced dislocation movements ahead of crack tip. Fundamental understandings of hydrogen embrittlement mechanisms have been appreciably achieved thanks to advances in high performance theoretical tools as well as high-resolution experimental instruments. Nevertheless, the embrittlement mechanisms and kinetics involved are not fully resolved and are still controversial disputes as they cannot be generally applied to all materials in a particular environment.

The joint effects of corrosion and fatigue, which have been considered as hazardous threats to structural integrity, are highly dependent on many factors including temperature, stress state, working conditions, and kind of materials [8]. The corrosion fatigue behavior of materials in marine structures has long been a topic of practical importance. Nevertheless, a number of failures have been encountered in many offshore structures and components in spite of several published reports. This work investigates the effects of pitting corrosion on fatigue behaviors of AA6061-T6 with the aim of having a better understanding of fatigue crack initiation and propagation mechanisms of aluminum alloys in a corrosive environment and providing a more realistic corrosion fatigue life prediction for marine structures.

6.2 Experimental Procedure

The experiment was conducted using sheets of AA6061-T6 with a thickness of 4.06mm. The chemical composition and mechanical properties of this aluminum alloy were indicated in previous chapters. Two types of fatigue sample fabricated along rolling direction were used to investigate crack initiation as well as crack propagation behavior of this aluminum alloy. The sample surfaces were polished with subsequent use of 800 and 1200 grit SiC paper prior to fatigue testing to ensure surface roughness R_a is less than 0.15μm.

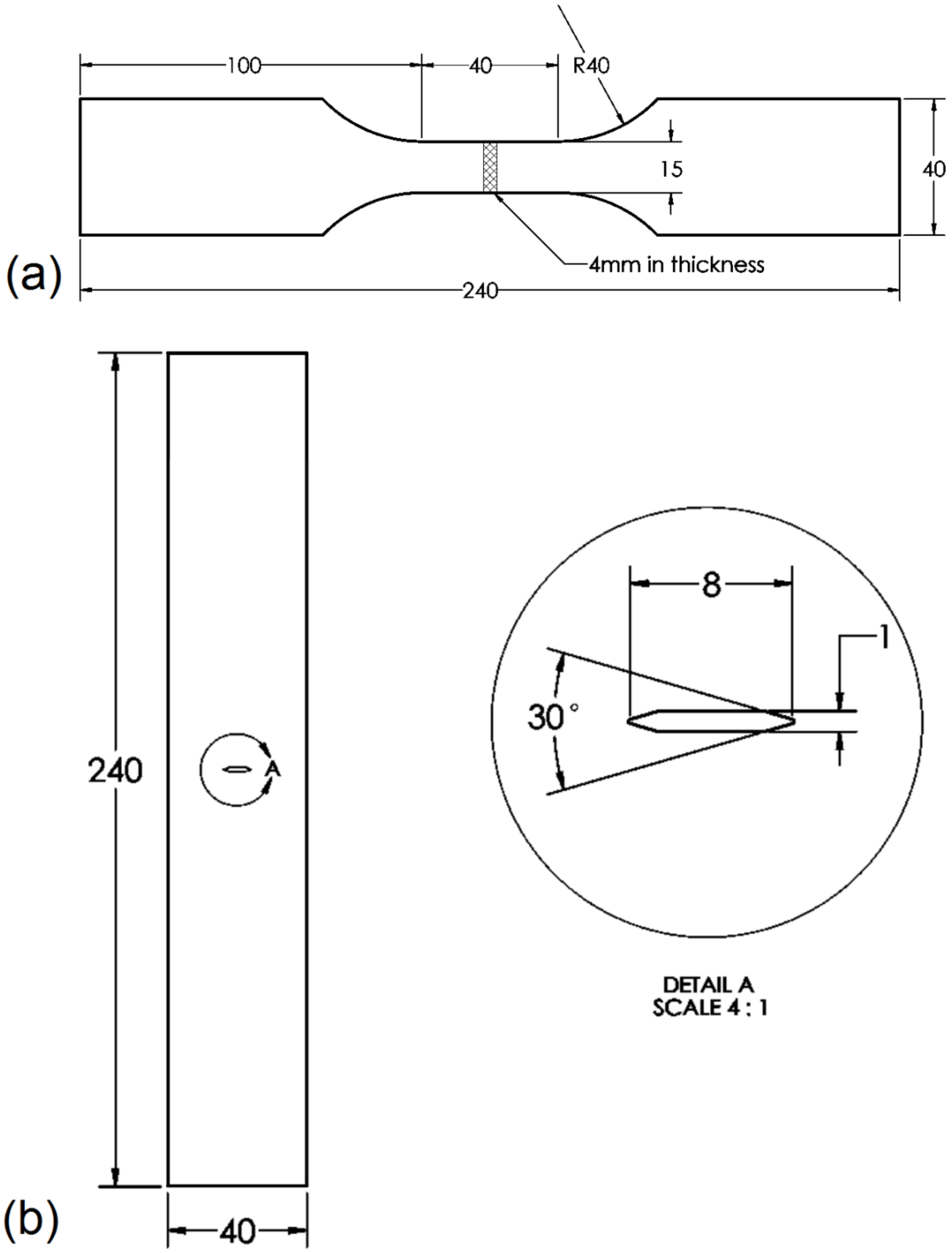

Figure 6.1 Specimen dimensions for fatigue testing (a) Dog-bone specimen and (b) Middle tension specimen

Dog-bone specimens were designed according to ASTM E466 requirement with the dimensions as shown in Figure 6.1(a) to study crack initiation and short fatigue crack behavior. This type of sample was loaded under fully reversed tension-compression loading (load ratio $R = -1$) at room temperature with load frequency of 5Hz using the MTS 810 Material Testing System. At each stress level, three tests were repeated and the average number of cycles to failure was calculated to determine the S-N curve (cyclic stress amplitude versus cycles to failure) of this material.

Fatigue crack growth tests were performed using Middle Tension (MT) samples with a load ratio of $R = 0.1$ $(\sigma_{min}/\sigma_{max} = 4.5MPa/45MPa)$ to minimize crack closure effects during testing. The geometry of the MT samples was in agreement with the ASTM E647 standard. It has a notch of 8mm with radius 0.2mm at the notch tips fabricated using electrical-discharge machining (EDM). EDM can minimize the residual stress near the notch so that the fatigue life will be least affected. The gage length is set at 160mm with a grip length of 40mm. Figure 6.1(b) shows the geometry of the MT sample used in this study.

An environmental chamber consisting of 3.5% NaCl by weight was used to analyze the effect of corrosion on fatigue behavior of aluminum alloy. The solution was circulated through the environmental chamber by a peristaltic pump to provide continuous aeration and replenishment of the test solution. The flow rate was kept constant at 51 mL/minute to avoid erosion-corrosion phenomenon. The pH of this synthetic seawater solution was adjusted to 8.2, and the specimens were exposed to the test solution for 1 hour before applying cyclic loading. Figure 6.2 shows the overall setup of operating the MTS 810 machine in the conduct of fatigue testing of dog-bone and MT specimens in an environmental chamber. Samples subjected to corrosion fatigue were taken out and cleaned immediately after failure to preclude corrosion processes from obscuring fine details of fracture surfaces.

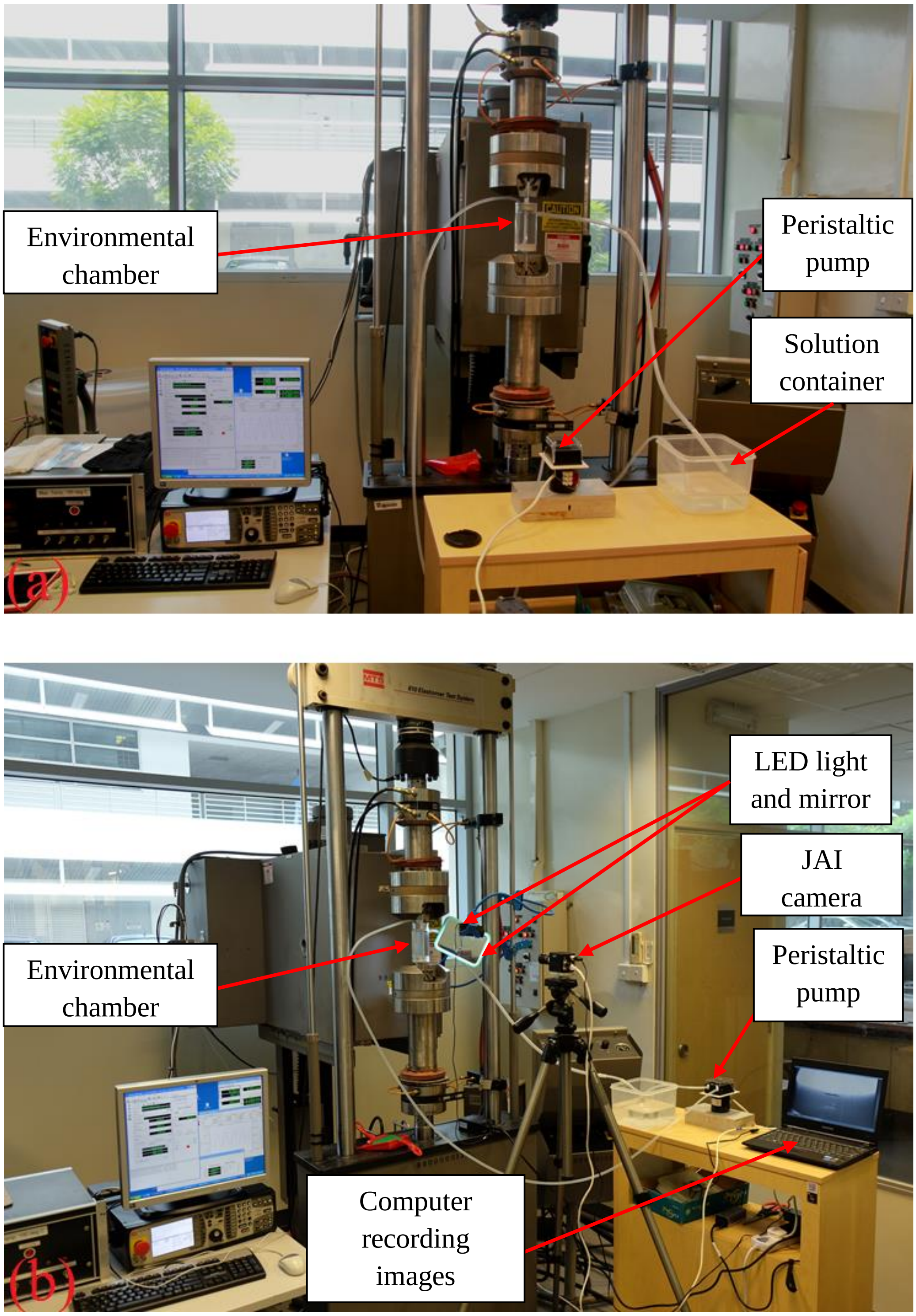

Figure 6.2 Experimental set-up for corrosion fatigue testing of (a) Dog-bone specimen and (b) MT specimen

The fatigue crack growth rate of each MT specimens was obtained by placing a high-speed camera in front of the MTS machine to monitor fatigue crack growth. A mirror was placed behind the specimen at 45° relative to the specimen surface. The mirrors would reflect the specimen surfaces such that the fatigue crack growth could be captured by the high-speed camera. As the fatigue pre-crack reached the length of 1mm, the camera will start to capture image at every few minute interval in order to calculate crack length increment throughout the entire fatigue test. Images captured by the high-speed camera were then processed using an image processing software, ImageJ. Previous experience was obtained from similar specimen configuration and testing apparatus to ensure that crack symmetry requirements are met consistently. Therefore, crack length measurement was made only on the front side of the sample. The front left and front right crack lengths in each image were measured using ImageJ by drawing a straight line from the notch tip to the fatigue crack tip as shown in Figure 6.3. As crack tip may deviate from the plane of symmetry due to the formation of shear lip, the projected length of the notch tip to the crack tip on the plane of symmetry would be used instead. Average crack lengths were calculated and plotted against the corresponding number of cycles.

Using these data, the fatigue crack growth rate and stress intensity factor ranges were calculated using the equations:

Fatigue crack growth rate:

$$\left(\frac{da}{dN}\right)_{\bar{a}} = \frac{(a_{i+1} - a_i)}{(N_{i+1} - N_i)} \tag{6.1}$$

Stress intensity factor range:

$$\Delta K = \frac{\Delta P}{B}\sqrt{\frac{\pi\alpha}{2W} sec\frac{\pi\alpha}{2}} \tag{6.2}$$

where,

$$\bar{a} = \frac{a_{i+1} + a_i}{2}$$

$$\alpha = 2\bar{a}/W$$

$\Delta P = P_{max} - P_{min}$

B is specimen thickness

W is specimen width

Some of the fatigue tests were terminated after certain numbers of cycles in order to investigate fatigue crack initiation and propagation mechanisms of aluminum alloy in a corrosive environment. Once a critical fatigue crack was identified, the surrounding area of this crack was shortly polished then subsequently etched with Keller's reagent for 3 minutes and Weck's reagent for 30 seconds to reveal the microstructure. Fatigue crack initiation and propagation characteristics of corrosion fatigue samples were examined using a FESEM-JEOL7600 equipped with orientation imaging microscopy. Lastly, fracture features at different crack lengths of dog-bone specimens tested in NaCl solution were examined and compared with those of fatigue specimens tested in air to predict the initiation and propagation behaviors of small fatigue crack.

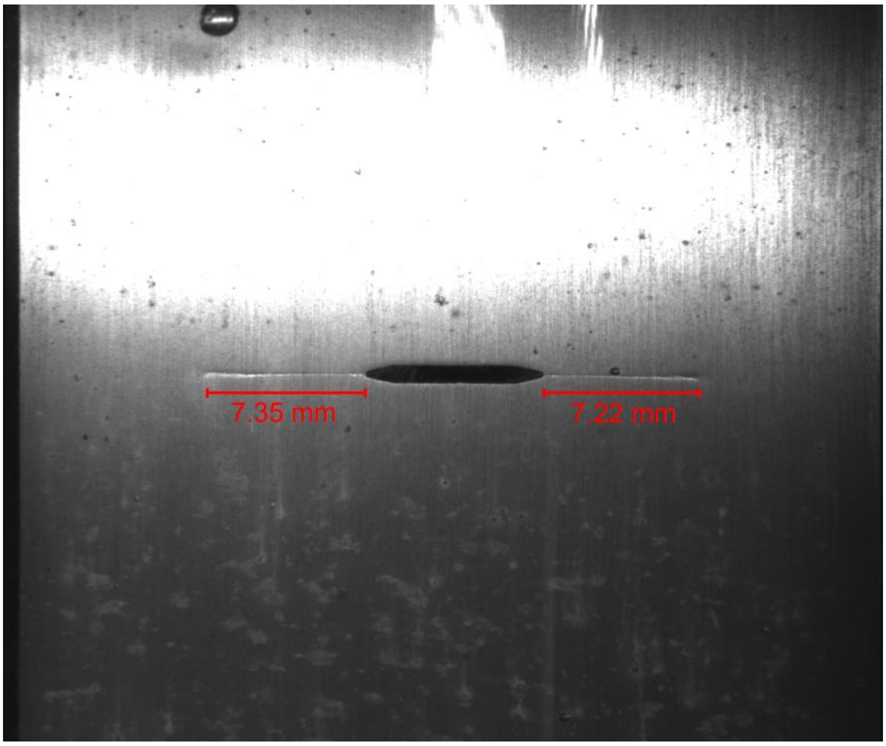

Figure 6.3 Crack length measurements from camera image of MT specimen

6.3 Evaluation of fatigue performance

The fatigue lives of AA6061-T6 samples subjected to fatigue loading in air and in NaCl 3.5% solution were shown in Figure 6.4. As aluminum does not exhibit a typical fatigue endurance limit, there is a continuous reduction of the number of cycles to failure N as maximum stress amplitude S increases when plotted on a logarithmic scale. The following equation described the underlying relationship between fatigue lives versus maximum stress amplitude:

$$logN = logA - mlogS \tag{6.3}$$

where, m is the slope and $logA$ is the intercept. This equation can be rewritten in the form traditionally used to describe S-N relationship:

$$S^m N = A \tag{6.4}$$

The fitting curves of fatigue endurance for samples tested in air and in NaCl 3.5% solution were calculated using average fatigue lives at each stress amplitude:

$S^{9.82}N = 1.41 \times 10^{27}$ for samples tested in air

and $S^{3.94}N = 1.94 \times 10^{13}$ for samples tested in NaCl 3.5% solution.

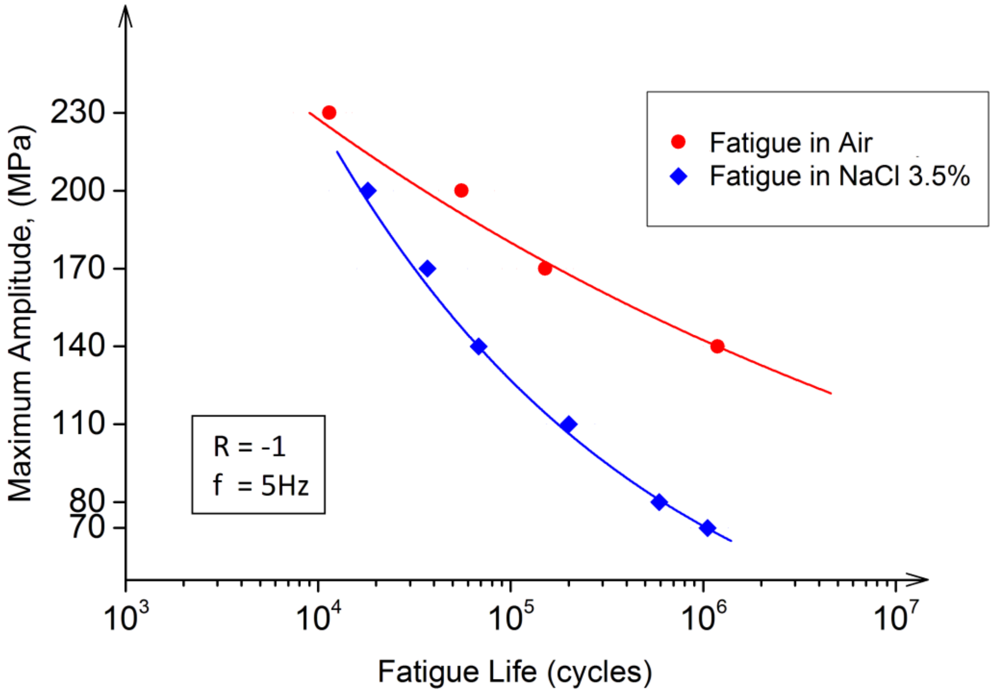

Figure 6.4 Fatigue S-N curves of AA6061-T6 tested in air and in NaCl solution

The fatigue performance of AA 6061-T6 was drastically downgraded when tested in NaCl solution with the allowable stress for fatigue life higher than one million cycles is less than *80MPa*. On the other hand, specimens subjected to fatigue loading in air can sustain more than one million cycles at much higher stress amplitude (approximately *140MPa*). The damage ratios of average fatigue life tested in NaCl solution to that tested in air ($N_{f\ NaCl}/N_{f\ air}$) at three different stress levels *200MPa, 170MPa and 140MPa* were calculated to be *3.06, 4.08* and *17.38* respectively. The increasing of fatigue damage ratio in association with diminishing stress amplitude indicates that the effect of corrosion fatigue is more significant at lower stress amplitude as there would be more time for corrosion reactions and hydrogen embrittlement processes to take place on materials. As a result, the crack initiation and crack propagation regions are minor at higher stress amplitude in comparison with final failure region caused by shear fracture.

6.4 Initiation and propagation behaviors of small fatigue crack

In order to elucidate the effects of corrosion environment on fatigue crack initiation and propagation, the fracture surfaces of failure samples were investigated using SEM. Figure 6.5 reveals the overview and details of fracture surface of a fatigue sample tested in air. Without the presence of corrosive environment, crack initiation was caused by extrusion and intrusion activities of materials along slip planes, which in turn form persistent slip bands and initiate fatigue crack as shown in Figure 6.5(b). Crack propagation mainly occurred by dislocations nucleated from the plastic zone induced by local stress-strain concentration ahead of crack tip. As aluminum alloys are relatively ductile, most of such dislocations would cause crack blunting while only a small portion will advance fatigue crack. Therefore, striations can be clearly observed all over the fracture surface with increasing crack length as shown in Figures 6.5(c), 6.5(d) and 6.5(e). Fine striations were found at short crack length while coarse striations can be clearly observed at extended crack length near the fast fracture region with large striation spacing. The fast fracture region is generally rougher than the fatigue crack growth region and shows formation of many dimples caused by the large amount of plastic deformation and micro-void coalescences (Figure 6.5f).

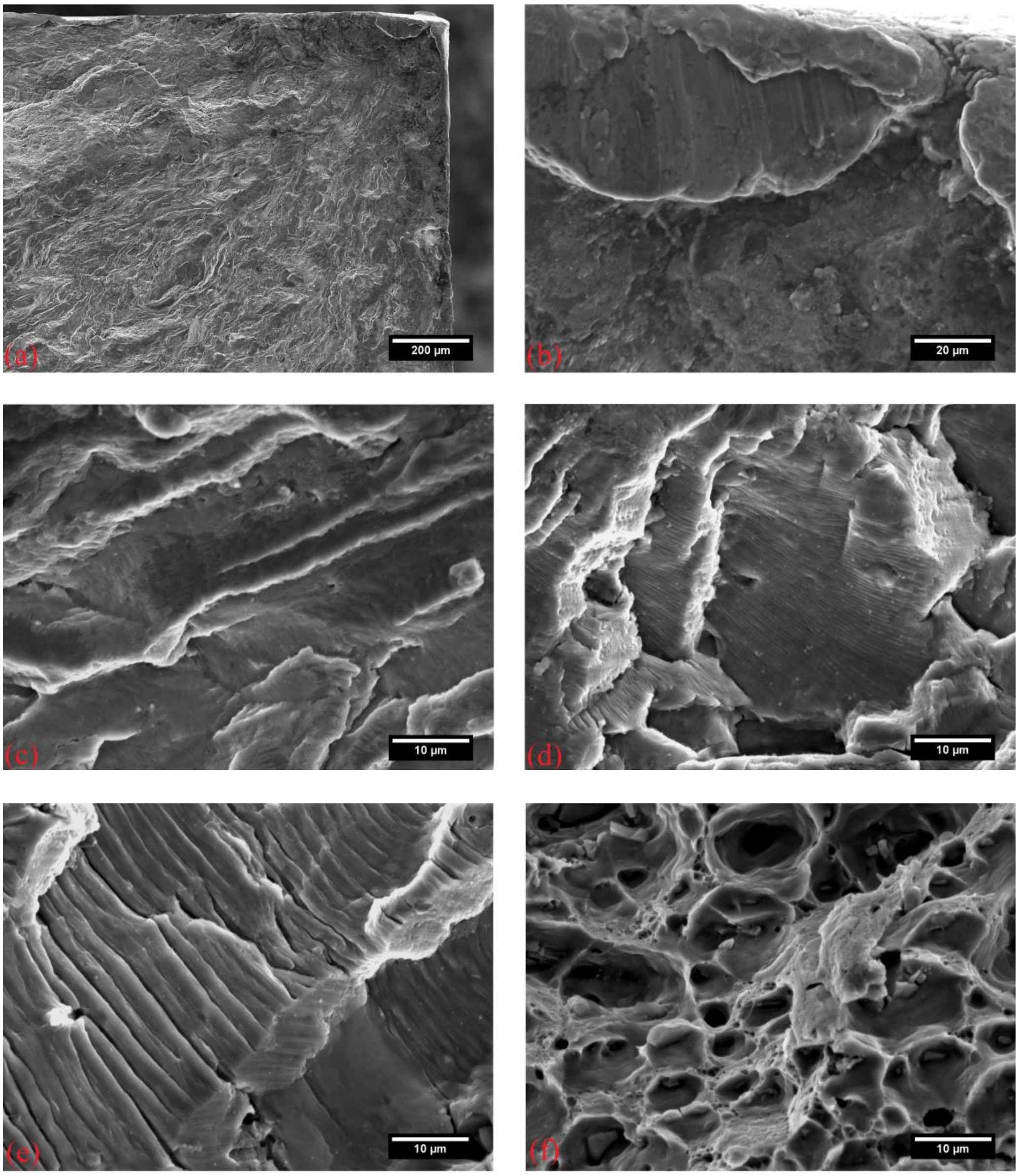

Figure 6.5 (a) Overview and (b,c,d,e,f) details of fracture surface of a fatigue sample tested in air with increasing crack length

When subjected to a corrosive environment, crack nucleation, as well as crack evolution, was affected. In order to investigate fatigue crack initiation characteristics of samples subjected to fatigue loading in a corrosive environment, some fatigue tests were terminated prior to failure and examined using optical microscope to identify critical cracks. Once a critical fatigue crack was identified, the surrounding area of this crack was shortly polished with colloidal silica 0.04-micron suspension for 2 minutes and then etched with Keller’s reagent in 30 seconds to reveal the microstructure for examination. Figure 6.6 shows SEM image and orientation map of a pit that initiates critical fatigue crack.

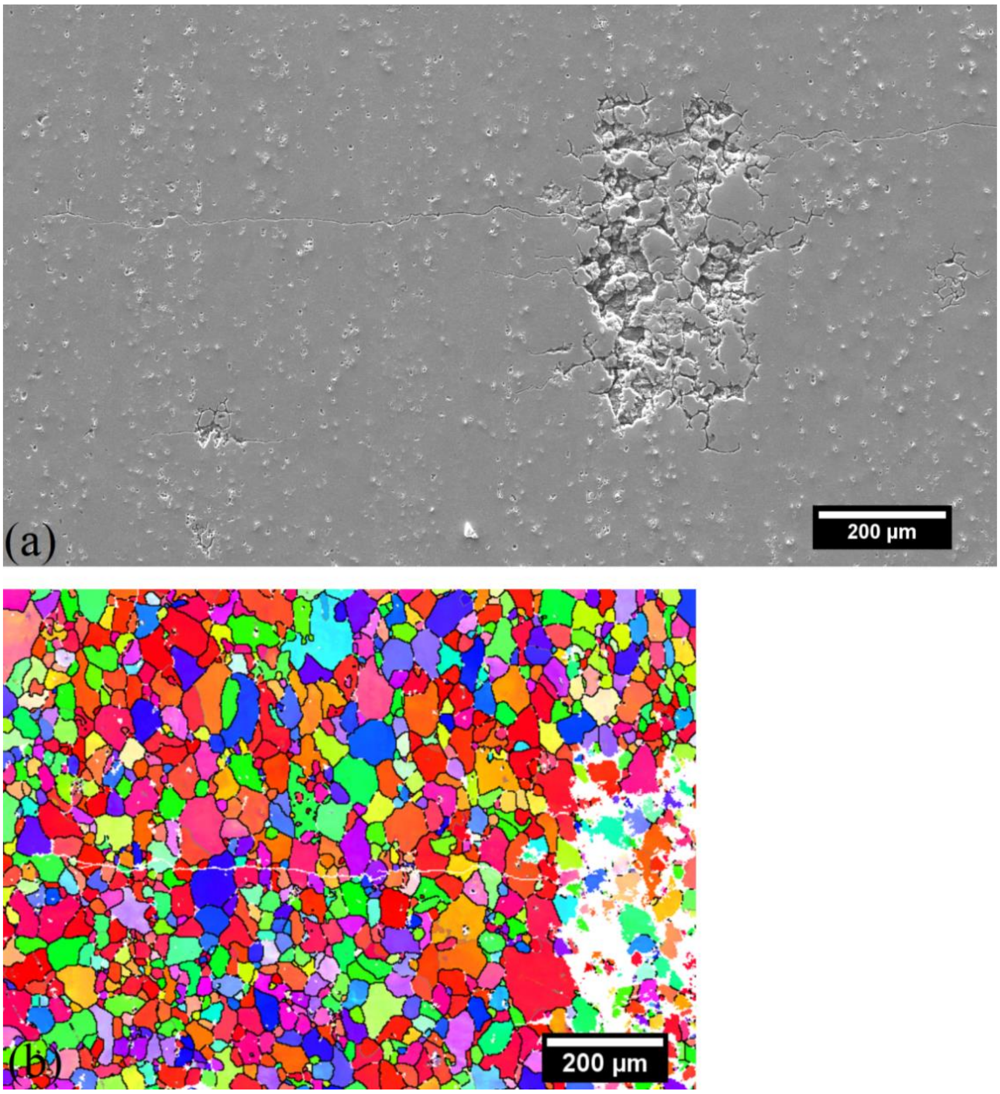

Figure 6.6 SEM image and orientation map of a pit that initiates critical fatigue crack

It can be seen that crack initiated from both sides of pit mouth which are highest stress concentration locations as demonstrated in section 4.5. Similar to crack initiation of a pre-corroded sample, grain boundaries surrounding crystallographic pits were attacked due to anodic reactions of corrosion processes, which create a local acidic environment with high chloride concentration. This local acidic environment creates a precipitate free zone, which facilitates intergranular corrosion at pit walls. Furthermore, fatigue loading can break down the protective aluminum hydroxide layer such that aggressive environment can easily penetrate into the metal as shown in Figure 6.7(a). High stress concentration at both sides of pit mouth in conjunction with attacked grain boundaries favored fatigue crack nucleation and substantially reduced fatigue life as crack initiation could account for up to 80 percent of the total corrosion fatigue life. It should be noted that intergranular corrosion only occurred around the perimeter of crystallographic pit within the zone that local pitting potential was modified by corrosion reactions as shown in Figure 6.7(b). Outside the corroded area, grain boundaries were not attacked and the occasional occurrence of intergranular fatigue crack growth in Figure 6.6(b) did not involve intergranular corrosion but associated with decohesion of grain boundaries due to the absorption of hydrogen and its compounds.

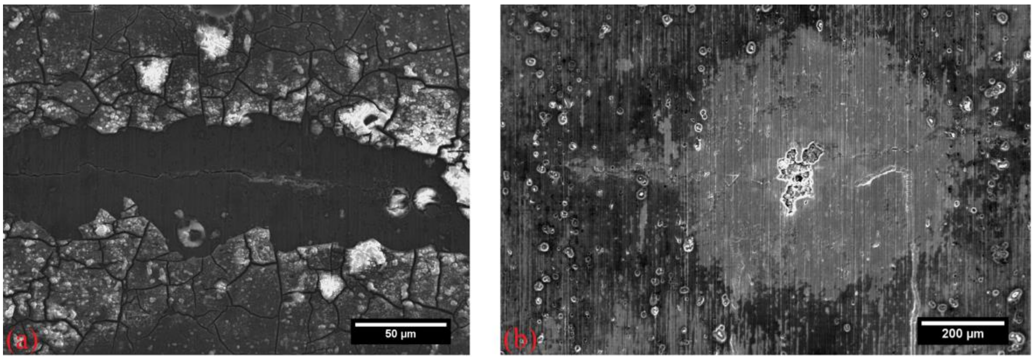

Figure 6.7 (a) Breakdown of oxide layer and (b) Overview of a corrosion fatigue crack prior to cleaning

The fracture surface of fatigue sample failed in NaCl 3.5% solution was shown in Figure 6.8. It can be seen that fatigue cracks nucleated from both sides of pit mouth forming multiple crack fronts. As these crack fronts further propagated, they merged into each other leaving a tearing ridge on the fracture surface. The fracture surface also revealed subsurface damage of corrosion with horizontal grain attack due to the morphology of grain structure, which is in the transverse-short transverse direction in this case. Two stages of short crack growth can be distinguished by detailed fractographic features as shown in Figure 6.8. Near crack origin, which is a crystallographic pit, fracture surface appears to be flat, and crack propagates transgranularly along crystallographic planes forming brittle cleavage patterns (Figure 6.8b). As crack grows to a critical length, extensive localized slip and fatigue striations are observed on fracture surface instead of cleavage facets (Figures 6.8c and 6.8d). It indicates that there is a change in crack growth mechanism of short fatigue crack when subjected to a corrosive environment.

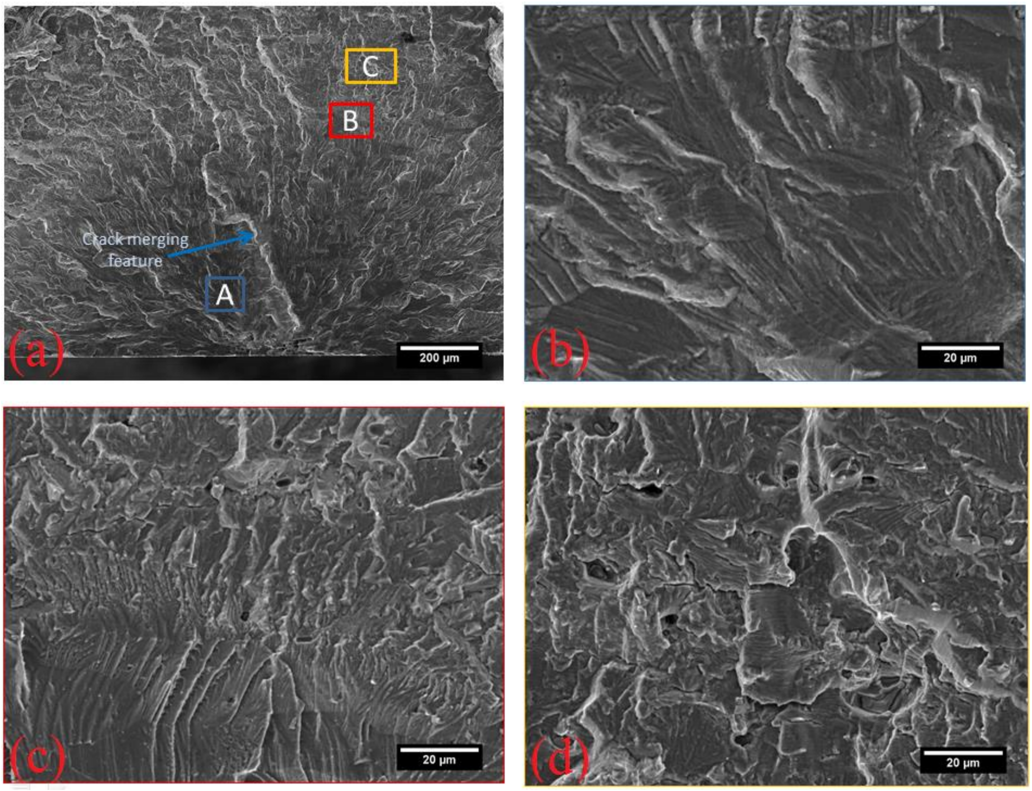

Figure 6.8 (a) Overview of fracture surface of a fatigue sample tested in NaCl solution and corresponding details of (b) area A; (c) area B and (d) area C

The higher crack growth rate and reduction of fatigue life of aluminum alloys in the corrosive environment can be attributed to the presence of hydrogen formed by cathodic corrosion reactions. The mechanism of pitting is based on the dissolution of metals in anode:

$$Al \rightarrow Al^{3+} + 3e^- \tag{6.5}$$

and several cathodic reactions, which could be the oxygen reduction:

$$O_2+2H_2O + 4e- \rightarrow 4OH^- \tag{6.6}$$

or hydrogen development in neutral or acidic environments:

$$2H^+ + 2e^- \rightarrow H_2 \tag{6.7}$$

$$2H_20 + 2e^- \rightarrow H_2+20H^- \tag{6.8}$$

The presence of hydrogen causes crack tip embrittlement and escalates crack growth rate. Moreover, the cohesive bonding at crack tips can also be weakened due to the high concentration of chloride ions in salt water. Fracture surface of corrosion fatigue samples exhibits brittle characteristics in comparison with ductile striations as in the case of fatigue samples tested in air. It is generally accepted that hydrogen absorption weakens interatomic bonds at crack tips and accelerate crack advancement. However, the speed of hydrogen diffusion and adsorption could be responsible for variation in crack growth mechanisms at different crack lengths. At short crack length where crack growth rate is small, there is sufficient time for corrosion reactions to produce hydrogen and diffuse it to crack front. Hydrogen absorbs at crack tips and weakens interatomic bonds such that decohesion occurred by tensile separation of atomic bonds on low index crystallographic planes. Capillary transportation of hydrogen is limited as it requires a crack tip with significant radius. However, the plastic zone size ahead of crack tip is relatively small at low stress intensity region meaning crack tip radius is tiny to favour capillary flow.

As crack grows further to a certain length corresponding to higher stress intensity, there would be not enough time for hydrogen diffusion at higher crack growth velocity. Therefore, crack tip is not embrittled yet, and most of dislocation activities caused by fatigue loading would produce crack tip blunting rather than crack advancing as the plastic zone size is enhanced at higher stress intensity. This crack tip blunting process facilitates capillary transportation of embrittling agents, hydrogen in this case, to crack front. Capillary transportation of hydrogen is dominant over surface diffusion at this stage of crack growth and thereby initiates AIDE process. This process involves absorption of embrittling species at crack tips and stimulating dislocation emission, which means most of dislocations induced by fatigue loading would advance fatigue crack on suitable slip planes. Therefore, extensive localized slip and fatigue striations were observed at growing crack length as shown in Figure 6.9.

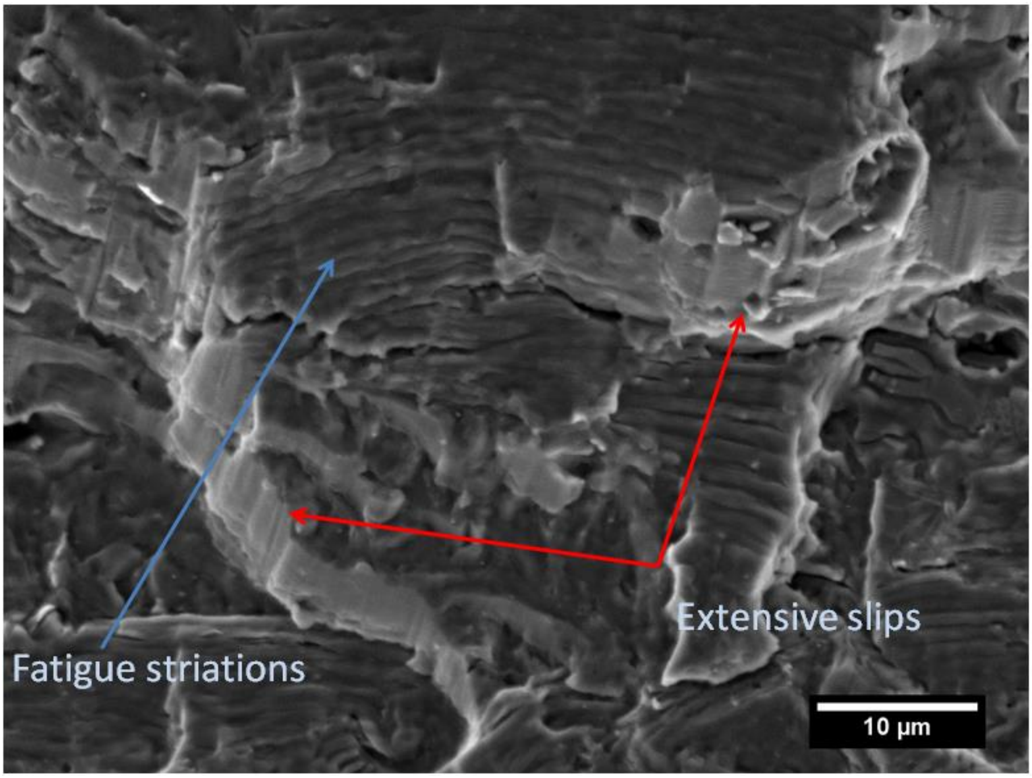

Figure 6.9 Extensive localized slip and fatigue striations at growing crack length

The crack growth processes described here were confirmed by the composite SEM image of a cross-section view of a fatigue crack in Figure 6.10(a). After cracks initiated from attacked grain boundaries at pit mouths, they merged into a single one and propagated transgranularly on the plane perpendicular to the loading direction. It indicates HEDE mechanism is dominant at short crack growth region. As fatigue crack further developed to such a length that crack growth velocity is too high to favour surface diffusion of hydrogen, AIDE took over crack growth process and facilitated extensive localized slips by shear movement, which can be observed at long crack growth region in Figure 6.10(a). The shear movement of crack tips at long crack growth region is enhanced by the formation of shear lip at extended crack length on the free surface, which is an implication that crack propagation is in mixed mode I+II+III (Opening+Sliding+Shearing) instead of the usually assumed pure mode I (Opening mode or tensile separation). Figure 6.11 shows a typical fracture surface of dog-bone sample and a schematic diagram of crack growth illustrating shear lip formation. As demonstrated by previous numerical studies, there is a reduction of approximately 40% in mode I stress intensity factor when shear lips develop on the crack surface in correspondence with an increase of about 40% of mode II (Sliding mode) and III (Tearing mode) stress intensity factors [9]. The rise of mode II and III stress intensity factors promoted shear displacements of crack tips forming extensive slips on the fracture surface. Extensive slips are more evident when crack grows further as the shear lip thickness, an indication of mode II and III stress intensity level, increases with escalating stress intensity factor. The orientation map of an area corresponding to long crack growth region is shown in Figure 6.10(b), it can be seen that intergranular crack growth occasionally occurred causing crack branching at selected areas. A possible explanation for occasional intergranular crack growth is that these grain orientations do not favour the occurrence of shear movement at crack front while their grains boundaries are more susceptible to dislocation emission and decohesion due to hydrogen segregation at grain boundaries. Furthermore, dislocation activities could affect the grain structure through the process of slip transfer such that their grain boundaries become weak links in the local stress field system. Crack advancement is intergranular or transgranular depending on which paths favour dislocation emission. Therefore, crack propagation in this region is in mixed mode with a higher fraction of transgranular. However, the appearance of intergranular decohesion is featureless when examined from fracture surface with the exception of occasional ridges or slips. Grain facets seem to be disguised by corrosion or oxidization processes, which were similarly observed in stress corrosion cracking.

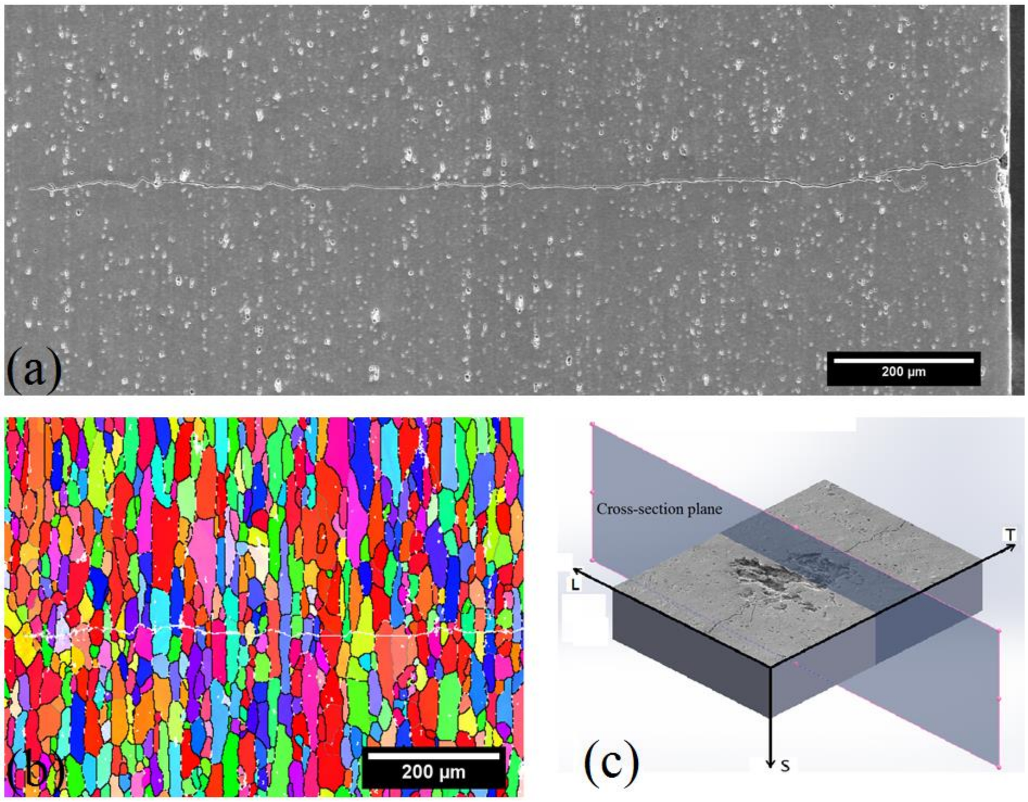

Figure 6.10 (a) SEM image of cross-section area of a fatigue crack; (b) corresponding IPF map at growing crack length and (c) Illustration of cross-section plane.

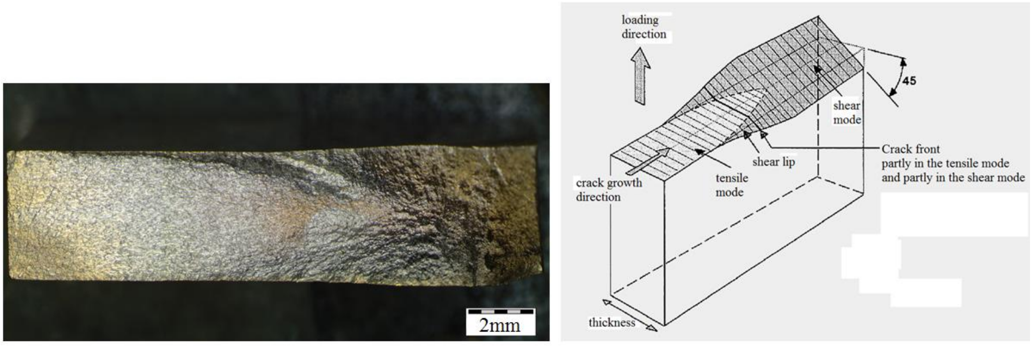

Figure 6.11 Optical image of fracture surface of dog-bone sample and illustration of shear lip formation

Figure 6.12 shows crystal orientation of a grain where slip occurred along [101] direction on (111) plane. It can be seen that crack advancement was strongly dependent on crystal orientation of grains located along crack path. Fatigue crack front was shown to preferably develop along <110> directions such that the closest packed planes {111}, which is the most preferable slip system for fcc crystal structures like aluminum, are more likely to intersect with crack front even if local stress state does not favour such directions. It was proved that at least five active slip systems are required to produce sufficient energy for shear dislocations [10]. Therefore, more active slip systems would be involved if closed packed planes intersect with crack front to facilitate shear movement.

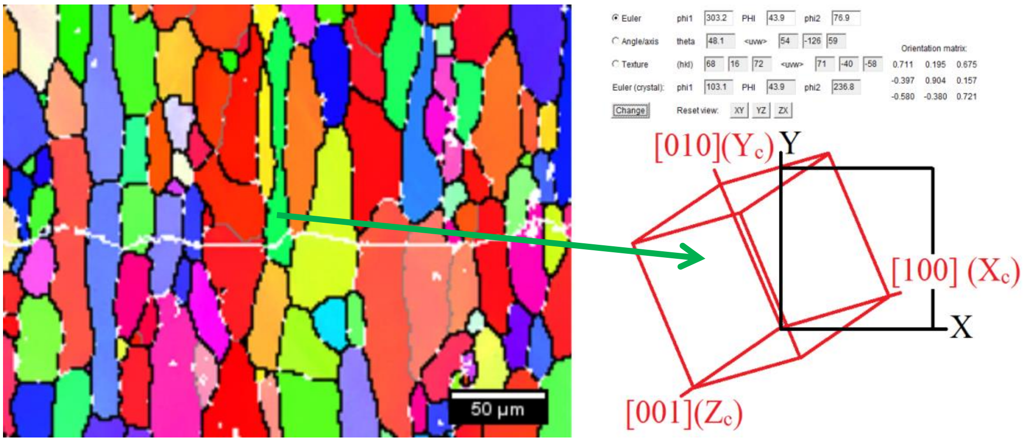

● Euler phi1 303.2 PHI 43.9 phi2 76.9
○ Angle/axis theta 48.1 <uvw> 54 -126 59
○ Texture (hkl) 68 16 72 <uvw> 71 -40 -58
Euler (crystal): phi1 103.1 PHI 43.9 phi2 236.8

Orientation matrix:
0.711 0.195 0.675
-0.397 0.904 0.157
-0.580 -0.380 0.721

Figure 6.12 Crystal orientation of a grain where slip occurred along [101] direction on (111) plane

6.5 Fatigue crack growth measurements

In order to quantify the effects of corrosion environment and characterize the effects associated with shear lip formation on crack growth behavior, fatigue crack growth rates were calculated by measuring crack length of MT samples. Figure 6.13 shows the plot of measured crack length versus the number of cycles of MT specimens tested in air and in NaCl 3.5%. It can be seen from the plot that the difference between the number of cycles to produce the same crack length increases with growing crack length. For crack lengths higher than 10mm, corrosive environment significantly decreases nearly 80%

the number of cycles needed to reach the same crack length when tested in air. As shown in Figure 6.14, fatigue crack growth rate of A6061-T6 when tested in NaCl solution is about half an order of magnitude higher compared to that tested in air.

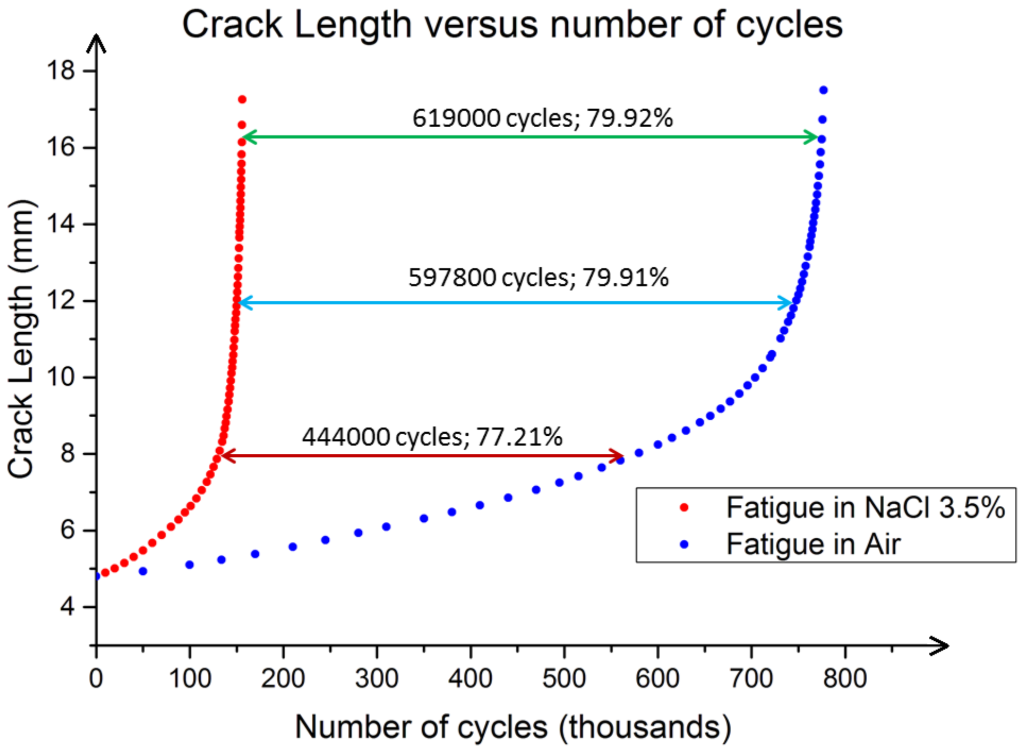

Figure 6.13 Measure crack length versus number of cycles of MT specimens tested in air and in NaCl 3.5%

Several crack growth transitions can be observed for samples tested in air as well as in NaCl solution. However, this study will focus on crack growth behaviors during stage II threshold region (transition T2 to T4) where crack growth is not a structure-sensitive phenomenon at material surface such that predictions based on stress intensity values can be justified. It can be seen that there is a change in the slope of crack growth curve in the stage II region, which is supposed to be linear on logarithmic scale according to the well-known Paris-Erdogan relationship:

$$\frac{da}{dN} = C\Delta K^n \tag{6.9}$$

The slope change during stage II region (transition T3) can be associated with the formation of shear lips similarly reported by other authors [9, 11]. The initiation of shear lips indicates a transition in stress state, which was observed for samples tested in air as well as in NaCl solution. As mentioned before, the formation of shear lip at growing crack length enhanced shear movements and is an implication that crack propagation is in mixed mode I+II+III. For samples tested in air, the rise of mode II and III stress intensity factor only reduces the slope of crack growth curve while the mechanism of crack growth is still dominated by fatigue striation formation.

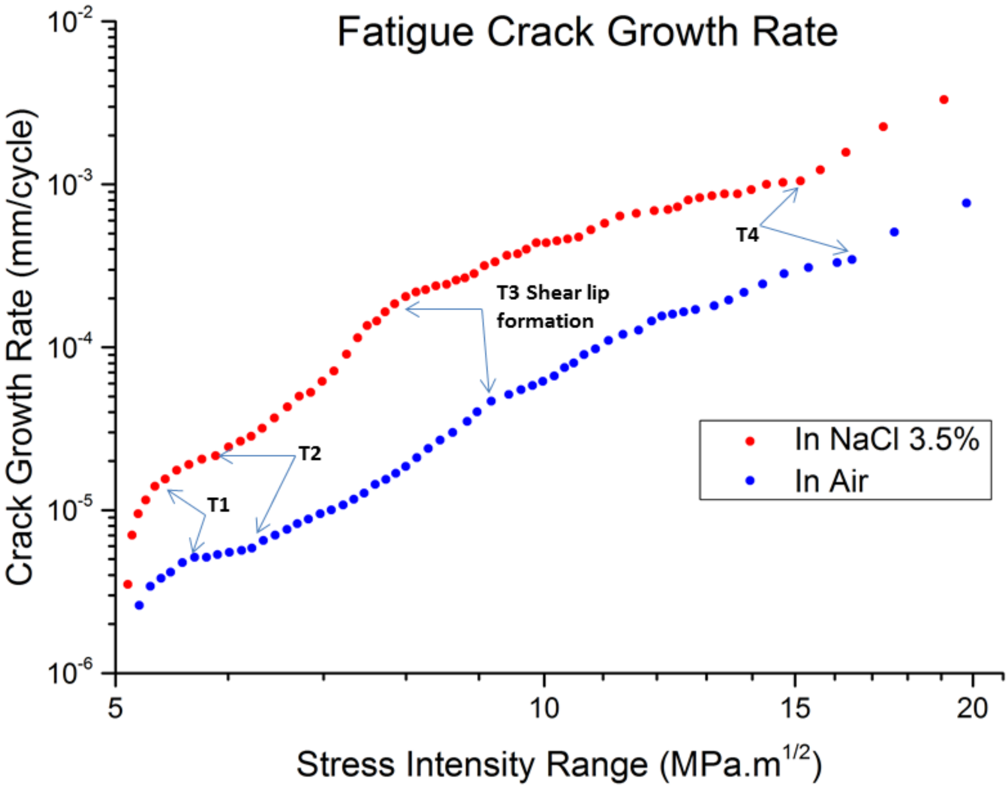

Figure 6.14 Fatigue crack growth rate of AA6061-T6 tested in air and in NaCl solution

As shown in Figure 6.15, the onsets of shear lip formation occurred at crack length $a = 10.6mm$ corresponding to $\Delta K = 9.18MPa\sqrt{m}$ for samples tested in air and $a = 9.16mm$ corresponding to $\Delta K = 7.99MPa\sqrt{m}$ for samples tested in NaCl solution. Noting here that shear lip thickness is thinner for samples tested in salt water as aggressive environment has impeding effects on dislocation movement at material surface. They are nicely in consistence with the points where transitions of crack growth occurred. In salt water, the fracture surface exhibits more brittle characteristics coupled with rough shear lips. As a corrosive environment promotes tensile decohesion rather than shear movement, higher crack growth rate is required in formation of shear lip in a corrosive environment.

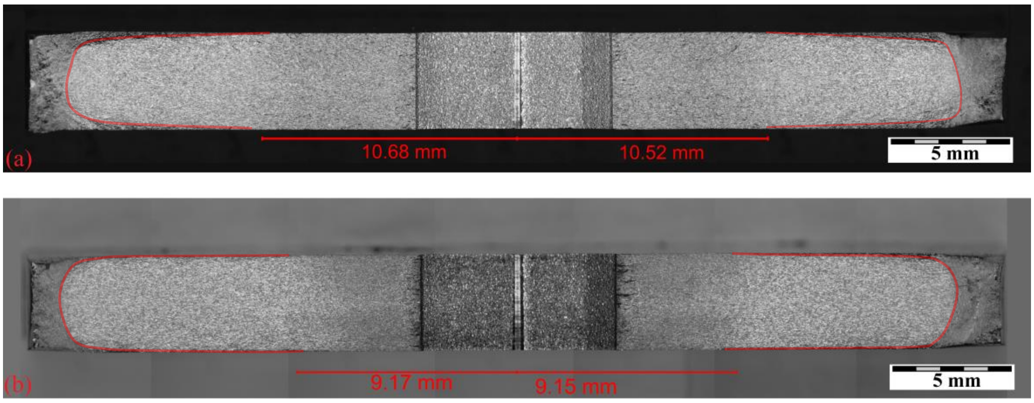

Figure 6.15 Fracture surface of MT samples tested (a) in air and (b) in NaCl solution showing onsets of shear lip formation (red lines indicate shear lip boundary)

The formation of shear lips is apparently caused by plastic deformation at the crack fronts near free surface of materials, which are less constrained than at mid-thickness. Due to the formation shear lips, crack path on the free surface may slightly deviate from the plane of symmetry even though crack plane does not change near mid-thickness. It is worth noting that the formation of shear lip is not the cause of changes in crack growth mechanisms but rather a phenomenon, together with a decrease in crack growth rate, activated by changes of stress state. It was reported that formation of shear lips could be impeded by making a shallow scratch of 0.1mm in depth along the crack path [12]. Specimens with shear lips and without shear lips exhibit the same crack growth behavior when they are identically fatigue loaded. Therefore, the onset of shear lips is just an indication of and is not responsible for changes in crack growth behavior. It appears that the change in crack growth behaviors associated with shear lip formation is a result of changes in stress state. As reported by previous researchers, the point where the slope of crack growth rate decreases corresponds to the onset of transition from plane strain to plane stress conditions at a specific stress intensity range and corresponding crack growth rate. It has been demonstrated that crack growth resistance is strongly dependent on the plastic zone size ahead of crack tip [13]. As plane stress condition arises, crack resistance increases as a result of increasing plastic zone size which in turn lessens the slope of crack growth rate curve.

6.6 Modelling crack growth behavior

The slope of crack growth rate curve is determined by the power law exponent n in equation (6.9). As there is a change in the slope of crack growth rate curve during stage II region, it is not possible to model crack growth behavior by using a single power law exponent when the transition of crack growth behavior occurred. In order to model crack growth behavior during stage II region, the concept of pivot point was used with two different power law exponents. This concept is based on the assumption that there is a linear relationship between lnC and the exponent n in equation (6.9). This relationship was identified either by mathematical calculation [14] or empirically by experimental results [15]:

$$lnC = -pn + q \tag{6.10}$$

By taking the logarithm of equation (1):

$$lnC = -\ln(\Delta K)n + ln\left(\frac{da}{dN}\right) \tag{6.11}$$

The constants p and q in equation (6.10) can be expressed dimensionally as:

$$\Delta K_p = e^p \tag{6.12}$$

and $$\frac{da}{dN_q} = e^q \tag{6.13}$$

It can be seen that e^p has the unit of stress intensity $MPa\sqrt{m}$ and e^q has the unit of crack growth rate mm/cycle. Combining equations (6.10), (6.12) and (6.13); it is then preferable to express equation (6.9) in the following form:

$$\frac{da}{dN} = \frac{da}{dN_q}\left(\frac{\Delta K}{\Delta K_p}\right)^n \tag{6.14}$$

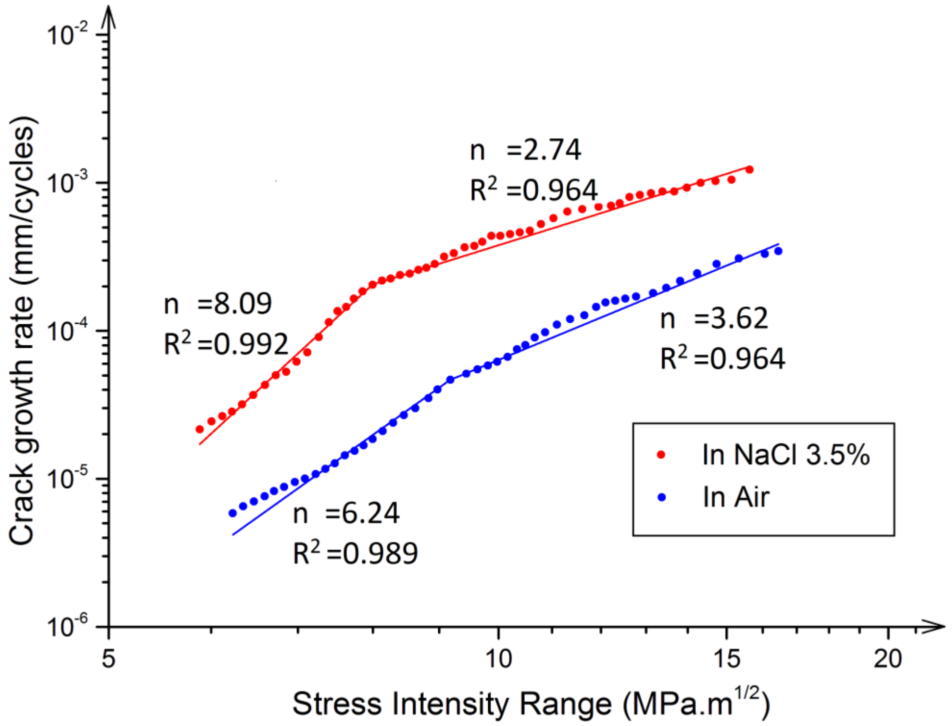

Figure 6.16 Fitting crack growth rate with different exponential laws

The point where transition of crack growth occurred corresponding to $\left[\Delta K_p, \frac{da}{dN_q}\right]$ was called "pivot point" by Tanaka [16]. By using equation (6.14), transition of fatigue crack growth behavior can be modelled by simply changing the exponential law n. In this study, the onsets of shear lip formations and crack growth transitions occurred at crack length $a = 10.6mm$ corresponding to $\left(\Delta K = 9.18, \frac{da}{dN} = 4.67 \times 10^{-5}\right)$ for samples tested in air and $a = 9.16mm$ corresponding to $\left(\Delta K = 7.99, \frac{da}{dN} = 2.05 \times 10^{-4}\right)$ for samples tested in NaCl solution. The slopes of crack growth rate curves before and after shear lip formation were determined by fitting crack growth data using linear least squares method. Thus, the fatigue crack growth rates in corrosive environment and in air during stage II can be modelled by the following equations:

$$\left(\frac{da}{dN}\right)_{air} = 4.67 \times 10^{-5} \left(\frac{\Delta K}{9.18}\right)^{6.24} \qquad \text{for } a \leq 10.6\ mm \qquad (6.15)$$

$$\left(\frac{da}{dN}\right)_{air} = 4.67 \times 10^{-5} \left(\frac{\Delta K}{9.18}\right)^{3.62} \qquad \text{for } a \geq 10.6\ mm \qquad (6.16)$$

$$\left(\frac{da}{dN}\right)_{NaCl} = 2.05 \times 10^{-4} \left(\frac{\Delta K}{7.99}\right)^{8.09} \qquad \text{for } a \leq 9.16\, mm \qquad (6.17)$$

$$\left(\frac{da}{dN}\right)_{NaCl} = 2.05 \times 10^{-4} \left(\frac{\Delta K}{7.99}\right)^{2.74} \qquad \text{for } a \geq 9.16\, mm \qquad (6.18)$$

The relatively high values of corresponding deviation R^2 in Figure 6.16 indicate satisfied goodness of fitting process. For samples tested in air, the change of exponential law is less significant as crack growth mechanism is still dominated by formation of fatigue striations after plane stress condition arises. In contrast, the slope change of crack growth curve when tested in salt water is more evident as hydrogen embrittlement and diffusion processes are involved in crack growth mechanism, which was before-mentioned.

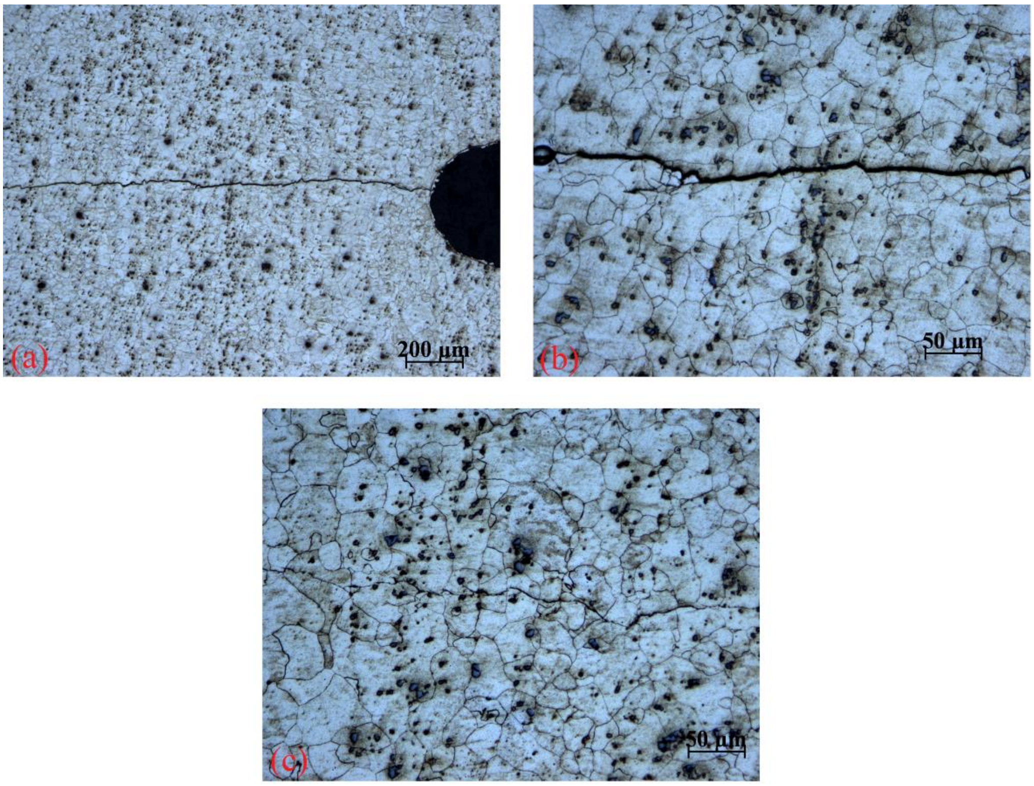

Figure 6.17 Optical images of cross section at mid-thickness of MT sample tested in NaCl solution (a) Overview; (b) detail at low ΔK (near notch tip) and (c) detail at high ΔK

Figure 6.17 shows optical images of cross sections at mid-thickness of a MT sample interrupted prior to failure. As MT samples emphasized the behavior of long fatigue crack, mixed mode of intergranular and transgranular was remarkable over the entire process of crack growth for samples tested in salt water. Near notch tip, crack is relatively straight indicating that tensile decohesion is still dominant at low stress intensity region. On the other hand, extensive slips are more evident at crack lengths corresponding to high stress intensity range due to the rise of plane stress condition. Extensive slips can also be observed for samples subjected to fatigue loading in air at growing crack length (Figure 6.18c). Nevertheless, crack developed transgranularly over the entire process when tested in ambient air as grain boundaries are not attacked by corrosion processes as can be seen in Figure 6.18.

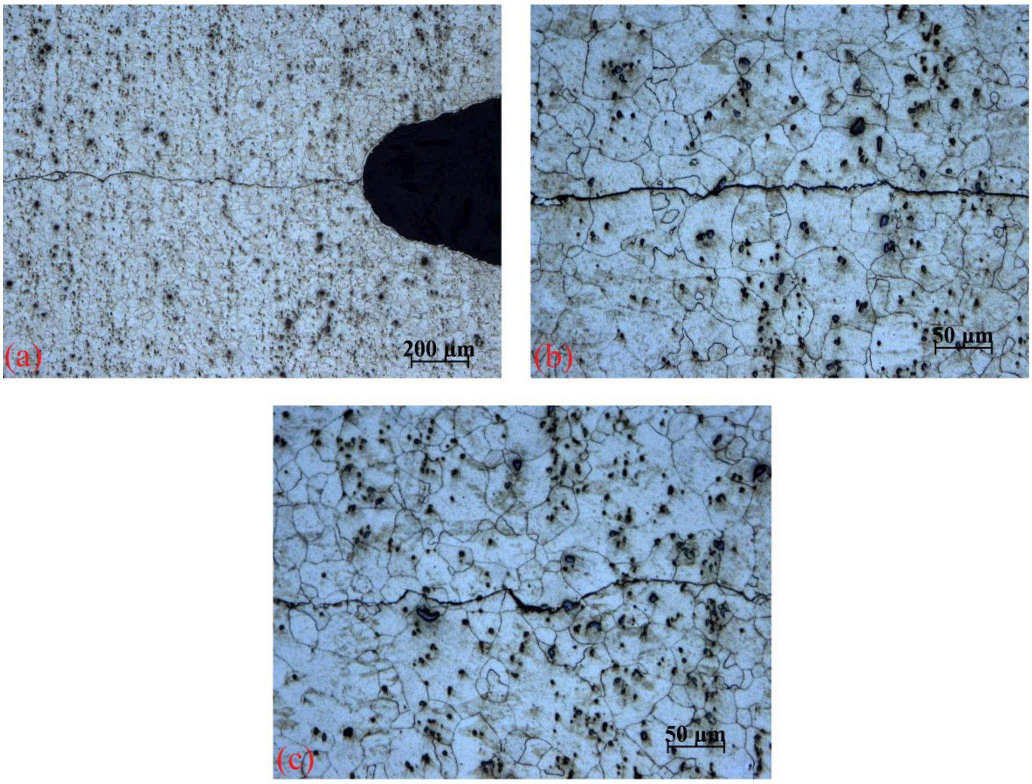

Figure 6.18 Optical images of cross section at mid-thickness of MT sample tested in air (a) Overview; (b) detail at low ΔK (near notch tip) and (c) detail at high ΔK

6.7 Conclusions

The fatigue performance of AA 6061-T6 was significantly downgraded when subjected to a corrosive environment NaCl 3.5% solution. Fatigue crack nucleation, as well as crack propagation, was affected by corrosive environment. High stress concentration at both sides of pit mouth in conjunction with attacked grain boundaries favoured fatigue crack nucleation while the presence of hydrogen formed by corrosion reactions caused crack tip embrittlement and intensified crack growth rate.

Two stages of short crack growth can be distinguished with detailed fractographic features. Near crack origin, which is a crystallographic pit, crack propagated transgranularly along crystallographic planes due to HEDE process. Further crack growth was dominated by AIDE process resulting in a mixed mode of intergranular and transgranular crack growth with a higher portion of transgranular.

When tested in corrosive environment, fatigue crack growth rate is escalated by about half an order of magnitude compared to that tested in air. The transition of crack growth during stage II region is associated with changes in stress state from plane strain to plane stress condition and the plastic zone size ahead of crack tip. The concept of pivot point was used to model transition of fatigue crack growth during stage II region. The slope change of crack growth curve, when tested in salt water, is more evident as hydrogen embrittlement and diffusion processes are involved in crack growth mechanism. In contrast, a lesser change of exponential law was observed for samples tested in air as crack growth mechanism is still dominated by the formation of fatigue striations after plane stress condition arises

References

1. *Newman, J., E.P. Phillips, and M. Swain, Fatigue-life prediction methodology using small-crack theory. International Journal of fatigue, 1999.* ***21****(2): p. 109-119.*

2. *Birnbaum, H.K. and P. Sofronis, Hydrogen-enhanced localized plasticity—a mechanism for hydrogen-related fracture. Materials Science and Engineering: A, 1994.* ***176****(1-2): p. 191-202.*
3. *Robertson, I., The effect of hydrogen on dislocation dynamics. Engineering Fracture Mechanics, 2001.* ***68****(6): p. 671-692.*
4. *Troiano, A.R., The role of hydrogen and other interstitials in the mechanical behavior of metals. trans. ASM, 1960.* ***52****(1): p. 54-80.*
5. *Oriani, R., Hydrogen embrittlement of steels. Annual review of materials science, 1978.* ***8****(1): p. 327-357.*
6. *Oriani, R., A mechanistic theory of hydrogen embrittlement of steels. Berichte der Bunsengesellschaft für physikalische Chemie, 1972.* ***76****(8): p. 848-857.*
7. *Lynch, S., Environmentally assisted cracking: overview of evidence for an adsorption-induced localised-slip process. Acta Metallurgica, 1988.* ***36****(10): p. 2639-2661.*
8. *Schijve, J., J. Schijve, and J. Schijve, Fatigue of structures and materials. 2001: Springer.*
9. *Zuidema, J., F. Veer, and C. Van Kranenburg, Shear lips on fatigue fracture surfaces of aluminum alloys. Fatigue & fracture of engineering materials & structures, 2005.* ***28****(1 ‐ 2): p. 159-167.*
10. *Friedel, J., Dislocations: International Series of Monographs on Solid State Physics. Vol. 3. 2013: Elsevier.*
11. *Amsterdam, E. and F. Grooteman, The influence of stress state on the exponent in the power law equation of fatigue crack growth. International Journal of Fatigue, 2016.* ***82****: p. 572-578.*
12. *ZUIDEMA, J., et al., ANOMALOUS FATIGUE CRACK GROWTH BEHAVIOUR IN AA 2024 AND AA 5083. Proceedings of Materials Structures and Micromechanics of Fracture (CD), Brno, 2001: p. 15.*
13. *Ritchie, R.O., Mechanisms of fatigue-crack propagation in ductile and brittle solids. International Journal of Fracture, 1999.* ***100****(1): p. 55-83.*

14. *Yokobori, T., I. Kawada, and H. Hata, Effects of Ferrite Grain Size on the Stage II Fatigue Crack Propagation in Plain Low-C Steel. Rep. Research Inst. Strength Fracture Mat. Tohoku Univ., 1973.* ***9****(2): p. 35-64.*
15. *Niccolls, E.H., A correlation for fatigue crack growth rate. Scripta Metallurgica, 1976.* ***10****(4): p. 295-298.*
16. *Tanaka, K. and S. Matsuoka, A tentative explanation for two parameters, C and m, in Paris equation of fatigue crack growth. International Journal of Fracture, 1977.* ***13****(5): p. 563-583.*

Chapter 7

Conclusions and recommendations

This research focuses on investigating corrosion fatigue behaviors of Aluminum alloys to provide a reliable corrosion fatigue control and further extend the use of aluminum alloys in offshore applications. The objectives of this work were firstly addressed by characterizing the morphological damage of pitting corrosion of aluminum alloys in 3-D and quantifying corrosion effects on pit induced stresses which responsible for crack initiation. Secondly, the effect of crystallographic texture on pitting susceptibility and fatigue performance were investigated. Characteristics of pitting corrosion and effects of prior corrosion on fatigue crack initiation were examined. Furthermore, fatigue crack initiation characteristics and crack growth mechanisms of an aluminum alloy when simultaneously subjected to a corrosive environment were addressed. This chapter draws together the noteworthy conclusions, and then the opportunities and strategies for future work are given.

7.1 Conclusions

7.1.1 Characterization of pitting morphology in 3-D

The 3-D morphological damage of pitting corrosion of AA7075-T6 was characterized using confocal microscopy and image processing. EDS analysis was carried out to identify different intermetallic particles and their role in corrosion performance of AA7075-T6. Confocal microscopy has been proven to be a great assistance in quantifying corrosion damage and characterizing pitting morphology in 3-D. Pitting morphology was classified using a 3-D shape descriptor defined by the ratio of average depth and maximum depth within a single pit. A methodology that simplified the general morphology of corrosion pit into idealized geometry was proposed. It was found that:

- $MgZn_2$ (η phase) is distributed over the entire aluminum matrix of AA7075-T6 with superior number density than other intermetallic particles. Its contribution to the overall pitting processes of AA7075 is much more significant than Mg_2Si particles even although Mg_2Si is the most anodic constituent found in AA7075.
- Corrosion severity increased with time in term of both affected area as well as pit depth. Pit width is generally larger than pit depth, which indicates that corrosion rate is higher at pit mouth than at the bottom. Pits were found to be predominantly semi-ellipsoidal and in the transitional region between conical and semi-ellipsoidal shape. Irregular and cylindrical pits were not found in this aluminum alloy.
- Stress-strain concentration factor significantly increased with corrosion duration. The highest stress-strain concentration factor reached a saturated point after 120h of immersion. Further increase of corrosion time to 240h does not significantly enhance highest stress-strain concentration. Within a single pit, highest stress-strain concentration occurred at both sides of pit mouth, which are 90^0 relative to the loading direction.
- Finite element analysis demonstrated that using semi-ellipsoid with equal surface area and maximum pit depth was a good approximation to predict

stress-strain distributions on corrosion surface and estimate stress-strain concentration factor caused by the presence of pits. The proposed method incorporates the combined effect of pit morphology and orientation as well as its interaction with other pits in adjacent areas. Therefore, it provides a realistic approximation in quantifying stress-strain concentration factor, which can be used to predict possible crack nucleation sites as well as the early stage of crack propagation behavior.

7.1.2 Microstructural characteristics of pitting corrosion

Microstructural characteristics of pitting corrosion were examined using SEM and OIM based analysis technique. Pitting corrosion of aluminum alloys was demonstrated to be strongly dependent on crystallographic orientation. The following conclusions can be drawn:

- There are two types of pitting occurring in AA6061-T6: hemispherical pitting and crystallographic pitting. Hemispherical pits formed by cathodic reactions around iron-containing particles have smooth profile, which is markedly distinguishable from crystallographic pits. The formation of crystallographic pits is associated with anodic reactions of aluminum alloys. Crystallographic pits were found to be more detrimental and preferably initiated from the inside of grains that have orientation close to $\langle 001 \rangle$.
- Surface morphology of crystallographic pits is influenced by the texture of grains on three different principle surfaces LT, LS and TS. On LT surface, crystallographic pits have equiaxed shape and are slightly elongated along rolling direction. On the other hand, pits on LS and TS surfaces are stretched out with respect to the grain texture. The morphology of crystallographic pits was demonstrated to be a key factor that affects the behavior of pit propagation as well as the anisotropic fatigue performance of aluminum alloys.
- Intergranular corrosion only occurred around the perimeter of crystallographic pits. The areas that do not crystallographically pit are invulnerable to intergranular corrosion. As corrosion time increase, the sharp facets of crystallographic pits become rounded and pitting process does not

significantly attack the materials although tunneling may occur below the pitting surface.

7.1.3 Effect of prior corrosion on crack initiation and fatigue performance

- When subjected to prior corrosion, fatigue endurance along rolling direction of AA6061-T6 is higher than along transverse direction due to the morphology of crystallographic pits and grain texture. The evolution of crystallographic pits is the main cause of fatigue life reduction. The anisotropy fatigue behavior of this aluminum alloy, when subjected to prior corrosion, can be attributed to the variations of pit morphology on three principle surfaces LT, LS, and TS. Crystallographic pits on LT surface are stretched out along rolling direction because of grain texture. Therefore, pits on LT surface of longitudinal samples have less stress concentration in comparison with transverse samples since they are orientated along loading direction.
- OIM analysis revealed that critical fatigue crack nucleated from grain boundaries that were damaged by corrosion processes around a crystallographic pit. Fatigue crack nucleation was further assisted by surrounding grains that have multiple active slip systems associating with high Schmid factor value. Once fatigue crack developed to a stable state, it propagated transgranularly on the plane perpendicular to the loading direction. Microstructures of corroded surface no longer affect crack propagation, since the resistance to crack evolution is dependent on materials properties as a bulk metal at this stage.

7.1.4 Crack growth mechanism when simultaneously subjected to corrosion and fatigue

- The fatigue performance of AA 6061-T6 was significantly downgraded when subjected to a corrosive environment NaCl 3.5% solution. Fatigue crack initiation, as well as crack propagation, was affected by corrosive environment. High stress concentration at both sides of pit mouth in conjunction with attacked grain boundaries favoured fatigue crack nucleation while the presence of hydrogen formed by corrosion reactions caused crack tip embrittlement and intensified crack growth rate.

- Fractography analysis showed that there is a change in crack growth mechanism of short fatigue crack when tested in NaCl solution. Near crack origin, which is a crystallographic pit, crack propagated transgranularly along crystallographic planes due to Hydrogen-enhanced decohesion process. Further crack growth was dominated by Adsorption Induced Dislocation Emission process resulting in a mixed mode of intergranular and transgranular crack growth with a higher portion of transgranular.
- When tested in corrosive environment, fatigue crack growth rate is escalated by about half an order of magnitude compared to that tested in air. The transition of crack growth during stage II region is associated with changes in stress state from plane strain to plane stress condition and the plastic zone size ahead of the crack tip. The concept of pivot point was used to model transition of fatigue crack growth during stage II region. The slope change of crack growth curve, when tested in salt water, is more evident as hydrogen embrittlement and diffusion processes are involved in crack growth mechanism. In contrast, a lesser change of exponential law was observed for samples tested in air as crack growth mechanism is still dominated by the formation of fatigue striations after plane stress condition arises.

In summary, the preferred orientation of grains having high susceptibility to pitting was identified that could offer an important contribution to corrosion resistance aspect. Corrosion inhibitors might be developed to restrict the corrosion processes of crystallographic pits on $\langle 001 \rangle$ facets that could, in turn, improve fatigue performance of structures operating in an offshore environment. Furthermore, advanced manufacturing techniques could be involved in producing materials with texture having superior corrosion resistance.

The existence of crystallographic pits was mainly mentioned in research works investigating corrosion behavior of single crystal or pure aluminum. There were scarcely a few studies touching on the crystallographic pitting behaviors of Aluminum alloys. From the corrosion fatigue aspect, most of research work merely focused on the degradation of fatigue performance. The existence of crystallographic pits was usually overlooked or not distinguished from hemispherical pits. To the best knowledge of the author, there has been no research showing that crystallographic pitting of aluminium alloys is strongly dependent on grain texture and grain orientation, which subsequently induce anisotropic fatigue performance. In general, the effects of microstructures and grain orientation on pitting susceptibility and fatigue performance of aluminium alloys have not been sufficiently investigated. A few studies have been carried out to investigate the dependence of corrosion fatigue behavior of Nickel superalloys or stainless Steel on microstructures and crystal orientation using EBSD technique. However, it is difficult to compare the results in this study with those works due to the dissimilarity in microstructure and the complexity of material-environment interactions. Therefore, further research is of the essence to provide more insights and comparisons in corrosion fatigue mechanism of aluminum alloys.

The cause of fatigue crack initiation in a corrosive environment was generally attributed to high stress concentration around corrosion pits. The role of damaged grain boundaries, which surround crystallographic pits, in fatigue crack initiation has not been widely recognized. Intergranular crack growth is commonly observed in stress corrosion cracking of Aluminum alloys while crack growth in corrosion fatigue is typically transgranular. In this study, crack propagation was observed to be in a mixed mode of intergranular and transgranular. Among different forms of hydrogen-induced degradation, intergranular degradation is the most hazardous as it can induce subcritical cracking at applied stress below the threshold level. In order to extend the use of aluminum alloys in an offshore environment, it is of the essence to lessen the severity of intergranular embrittlement in aluminum alloys.

7.2 Recommendations

Based upon the obtained results of this thesis, the following aspects are recommended for further investigations to promote the use of aluminum alloys in offshore applications

7.2.1 Characterizing pitting corrosion using X-ray computed tomography

In this study, confocal microscopy has been proven as a useful method in characterizing the 3-D morphological damage of pitting corrosion. However, a limitation of confocal microscopy is that it cannot capture subsurface damages of corrosion pits, which could result in an underestimation of corrosion severity. Further research on pitting characterization is encouraged to make use of X-ray computed tomography to provide more insights into the 3-D morphological characteristics of corrosion pits.

7.2.2 Conducting variable amplitude corrosion fatigue test

Structures operating in offshore conditions are normally designed to guarantee a fatigue life of 20 years or 10^8 cycles. Under certain circumstances, fatigue load can be simplified by constant amplitude cycles. However, failures of essential components still occur due to the variability of fatigue loads, which naturally exist in offshore conditions. Depending on the function and operating environment, the situations for corrosion fatigue of a component in actual operation can be appreciably different, especially with respect to the load-time history, material-environment interactions and prolonged years of exposure. These differences cannot be eliminated in practical problems. As load interactions during variable amplitude loading may have crack growth acceleration or retardation effect. This crack acceleration or retardation will result in a decrease or increase of fatigue life. Therefore, it is essential to predict corrosion fatigue life of a component subjected to variable loading amplitude and frequency. Complex fatigue loading spectrum is often simplified by loading blocks with varying amplitudes and sequences or by simple loading patterns containing periodic single overloads or underloads.

In most of previous studies, corrosion fatigue tests were usually conducted under constant amplitude conditions with closely controlled environment. Therefore, further investigation of this research is recommended to examine the effect of spectrum loading on corrosion fatigue behavior of aluminum alloys.

7.2.3 Scale up investigations

In this research work, only two types of aluminum alloys were investigated. However, different alloying elements exhibit various electrochemical behaviors, which in turn have distinctive effects on corrosion and fatigue performance. It suggests a great necessity to investigate the role of alloying elements and its influence on corrosion fatigue mechanism of aluminum alloys. Further research should be carried out to provide more insights and comparisons into the differences in corrosion fatigue mechanism of various classes of aluminum alloy.

7.2.4 Improving finite element model

In recent years, Extended Finite Element Method (XFEM) has been extensively used to model crack initiation and crack growth behavior as it is a mesh-independent fracture modeling technique. Finite element mesh can be generated independently from crack geometry while crack propagation does not require remeshing. The finite element model in this study still can be improved by taking into consideration the influence of fatigue loading. Furthermore, a subroutine can be written to define crack initiation and propagation criteria in XFEM to provide a more realistic model for characterizing the interaction between fatigue crack and corrosion pits.

7.2.5 Reducing intergranular fracture in aluminum alloys by “grain boundary engineer”

When fatigue loaded in NaCl solution, it was demonstrated that crack developed in a mixed mode of intergranular and transgranular. Although all forms of hydrogen-induced degradation mechanisms are of concern, intergranular degradation is the most hazardous as it can cause time-dependent subcritical cracking at applied stress below the threshold level. By using thermomechanical processing methods, the practicability of employing ‘‘grain-boundary engineering” techniques has been demonstrated to lessen intergranular embrittlement of metallic materials such as high-strength steels and nickel super alloy, etc.

SEM in conjunction with OIM technique has become a standard method to characterize grain boundary microstructure of polycrystalline materials. In order to extend the use of aluminum alloys in an offshore environment, it is of the essence to eliminate the severity of intergranular embrittlement in aluminum alloys. The experimental method used in this thesis can be applied to provide guidelines for designing an optimal microstructure of aluminum alloys with a high portion of special grain boundaries (such as annealing twins) that are inherently more endurable to intergranular cracking.